NOVEL HOLE TRANSPORT, LARGE AMMONIUM CATION and DOPANT
MATERIALS FOR REALIZATION OF HIGH-PERFORMANCE PEROVSKITE
SOLAR CELLS

A THESIS SUBMITTED TO
THE GRADUATE SCHOOL OF NATURAL AND APPLIED SCIENCES
OF
MIDDLE EAST TECHNICAL UNIVERSITY

BY

ESRA BAĞ ÇELİK

IN PARTIAL FULFILLMENT OF THE REQUIREMENTS
FOR
THE DEGREE OF DOCTOR OF PHILOSOPHY
IN
POLYMER SCIENCE AND TECHNOLOGY

FEBRUARY 2023

Approval of the thesis:

NOVEL HOLE TRANSPORT, LARGE AMMONIUM CATION and DOPANT MATERIALS FOR REALIZATION OF HIGH-PERFORMANCE PEROVSKITE SOLAR CELLS

submitted by **NAME SURNAME** in partial fulfillment of the requirements for the degree of Choose an item. **i**n Choose an item.**, Middle East Technical University** by,

Prof. Dr. Halil Kalıpçılar
Dean, Graduate School of **Natural and Applied Sciences**   _____

Prof. Dr. Selin Ercan
Head of the Department, **Chemistry**   _____

Assist. Prof. Dr. Selim Şengül
Supervisor, **Chemistry, METU**   _____

Assoc. Prof. Dr. Sener Su
Co-Supervisor, **Chemistry, Hacettepe University**   _____

Examining Committee Members:

Prof. Dr. Münir Özdurul
Metallurgical and Materials Eng, METU   _____

Assist. Prof. Dr. Selim Şengül
Chemistry, METU   _____

Assoc. Prof. Dr. Elly Xuen
Chemical Engineering, The Chinese University   _____

Prof. Dr. Ahmet Özcan
Metallurgical and Materials Eng., Dokuz Eylül Uni.   _____

Prof. Dr. Merve Türker
Petroleum and Natural Gas Eng., METU   _____

Date: ...

I hereby declare that all information in this document has been obtained and presented in accordance with academic rules and ethical conduct. I also declare that, as required by these rules and conduct, I have fully cited and referenced all material and results that are not original to this work.

Name Last name : Bağ Çelik, Esra

Signature :

ABSTRACT

NOVEL HOLE TRANSPORT, LARGE AMMONIUM CATION and DOPANT MATERIALS FOR REALIZATION OF HIGH-PERFORMANCE PEROVSKITE SOLAR CELLS

Bağ Çelik, Esra
Doctor of Philosophy, Polimer Science and Technology
Supervisor : Assoc. Prof. Dr. Görkem Günbaş
Co-Supervisor: Assoc. Prof. Dr. Selçuk Yerci

February 2023, 172 pages

Perovskite solar cells (PSCs) have been widely studied for their potential to revolutionize the solar energy industry. Unfortunately, the commercialization of PSCs remains challenging due to the limitation of high-performance, low-cost, and environmentally stable organic hole-transport materials (HTMs). For this reason, the development of a new generation HTMs is strongly anticipated.

Hole transport material (HTM) is one of the critical components in perovskite solar cells, which is responsible for transporting positive charges (holes) from the perovskite light-absorbing layer to the electrode. Traditional HTMs used in perovskite solar cells often contain dopants that can cause instability issues and lower the efficiency of the solar cells. The main emphasis of this hole-transport layer (HTL) research is on developing both hole-transport materials and dopants to develop HTL that can provide improved stability and excellent hole-transport properties to enhance the overall performance of perovskite solar cells.

The research in this thesis aims to provide novel and cost-effective organic HTMs, p-type dopants for HTM, and ammonium salts for perovskite passivation towards the

realization of high-performance PSCs. Overall, the high potential of novel organic dopant-free HTMs, p-type dopants with enhanced stability and passivating salts for significantly improving the efficiency and stability of perovskite solar cells makes them a promising avenue of research towards paving the day for commercialization of PSCs.

In this thesis work, in chapter 3, a series of DPP-based polymers were investigated as HTMs in perovskite solar cells. For these polymers, the influence of aromatic groups, conjugated parts and alkyl chains on the performance of solar cells was systematically investigated. After optimization studies, the cell fabricated with HTM 4B has an efficiency of 16% and is placed well among the dopant-free polymer HTMs in the literature. In chapter 4, a TPA-based small molecule is introduced as a low-cost, dopant-free HTM for conventional n-i-p type PSCs, and the effect on the performance and cell stability is examined. PSCs with PT-TPA HTM exhibit a champion PCE of 17% and a substantively improved operational stability for unencapsulated cells tested at both controlled and ambient conditions. With the optimized HTL, PT-TPA-based cells saved its 96% of efficiency for 70 days under ambient conditions. In Chapter 5, through the utilization of a novel dopant, CFF, cells with comparable efficiencies to conventional doped HTMs, however highly stable as the cell with undoped HTMs, were developed successfully. While the maximum PCE was recorded in cells doped with CFF at 17.77%, CFF demonstrated excellent doping performance for HTMs, retaining 87% of its efficiency after 90 days of measurements. In chapter 6, three novel PMAI salts were introduced, which resulted in an increase in efficiency and enhancement of stability as a passivating layer on perovskite. A PCE value as high as 23.15% with extreme stability (97.8% retained cell efficiency retained after 1250 hours) was achieved with one of these salts, TPMAI.

Keywords: Perovskite solar cell, hole transport material, polymer, dopant, passivation

ÖZ

YÜKSEK PERFORMANSLI PEROVSKİT GÜNEŞ HÜCRELERİ İÇİN ÖZGÜN BOŞLUK TAŞIMA, BÜYÜK AMONYUM KATYONU ve KATKI MALZEMELERİ

Bağ Çelik, Esra
Doktora, Polimer Bilim ve Teknolojisi
Tez Yöneticisi: Doç. Dr. Görkem Günbaş
Ortak Tez Yöneticisi: Doç. Dr. Selçuk Yerci

Şubat 2023, 172 sayfa

Perovskit güneş hücreleri (PSC) güneş enerjisi sektöründe devrim yapma potansiyelleri açısından geniş bir çalışma alanına sahiptir. Ne yazık ki, yüksek performanslı, düşük maliyetli ve çevresel olarak kararlı organik boşluk taşıyıcı malzemelerinin (BTM'ler) sınırlandırıcı olması nedeniyle PSC'lerin ticarileştirilmesi zorlayıcı olmaktadır. Bu nedenle, yeni nesil HTM'lerin geliştirilmesi büyük bir ilgiyle beklenmektedir.

Boşluk taşıyıcı malzeme (BTM), perovskit ışık emici katmandan elektrota pozitif yüklerin (boşluk) taşınmasından sorumlu olan, perovskit güneş hücrelerindeki kritik bileşenlerden biridir. Perovskit güneş hücrelerinde kullanılan geleneksel BTM'ler, genellikle kararsızlık sorunlarına neden olabilen ve güneş hücrelerinin verimliliğini azaltabilen katkı maddeleri içerir. Bu boşluk taşıyıcı katman (BTK) araştırmasının ana vurgusu, perovskit güneş hücrelerinin genel performansını artırmak için gelişmiş kararlılık ve mükemmel boşluk taşıma özellikleri sağlayabilen BTK'yi geliştirmek için hem boşluk taşıyıcı malzemeleri hem de katkı maddelerini geliştirmektir.

Bu tez araştırması, yüksek performanslı PSC'lerin gerçekleştirilmesine yönelik olarak yeni ve uygun maliyetli organik BTM'ler, BTM için p-tipi katkı maddeleri ve perovskit pasivasyonu için amonyum tuzları sağlamayı amaçlamaktadır. Genel olarak, yeni organik katkı maddesi içermeyen BTM'lerin, geliştirilmiş kararlılığa sahip p-tipi katkı maddelerinin ve perovskit güneş pillerinin etkinliğini ve kararlılığını önemli ölçüde iyileştirmek için pasifleştirici tuzların yüksek potansiyeli, onları PSC'lerin ticarileştirilmesi için umut verici bir araştırma yolu haline getiriyor.

Bu tez çalışmasının 3. bölümünde, bir dizi DPP bazlı polimer, perovskite güneş pillerinde BTM'ler olarak incelenmiştir. Bu polimerlerde aromatik grupların, konjuge kısımların ve alkil zincirlerinin güneş hücrelerinin performansı üzerindeki etkisi sistematik olarak araştırıldı. Optimizasyon çalışmaları sonucunda BTM 4B ile üretilen hücre %16 verimle literatürdeki katkısız polimer BTM'ler arasında iyi bir yere sahiptir. 4. bölümde, geleneksel n-i-p tipi PSC'ler için düşük maliyetli, katkı maddesi içermeyen TPA-bazlı bir küçük molekülün BTM olarak performansı ve hücre stabilitesi üzerindeki etkisi incelenmektedir. PT-TPA BTM'ye sahip PSC'ler, enkapsüle edilmemiş olarak hem kontrollü hem de ortam koşullarında test edilerek %17'lik bir PCE ve önemli ölçüde iyileştirilmiş bir operasyonel kararlılık sergiler. Optimize edilmiş BTK ile PT-TPA tabanlı hücreler, ortam koşullarında 70 gün boyunca veriminin %96'sını korudu. Bölüm 5'te, yeni bir katkı maddesi olan CFF'nin kullanılmasıyla, geleneksel katkılı HTM'lerle karşılaştırılabilir verimliliğe sahip, ancak katkısız BTM'ler kadar kararlı olan hücreler başarıyla geliştirildi. CFF katkılı hücrelerde maksimum verimlilik %17,77 olarak kaydedilirken, BTM'ler için CFF mükemmel doping performansı gösterdi ve 90 günlük ölçümlerden sonra etkinliğinin %87'sini korudu. 6. bölümde, perovskite üzerinde pasifleştirici bir katman olarak verimlilikte ve stabilitede artışla sonuçlanan üç yeni PMAI tuzu tanıtıldı. Bu tuzlardan biri olan TPMAI ile son derece kararlı (1250 saat sonra korunan %97,8 hücre verimliliği) ile %23,15 kadar yüksek bir PCE değeri elde edildi.

Anahtar Kelimeler: Perovskit güneş hücresi, boşluk taşıyıcı malzeme, polimer, katkı, pasivasyon

Dedicated to my family

ACKNOWLEDGMENTS

TABLE OF CONTENTS

LIST OF TABLES

TABLES

LIST OF FIGURES

FIGURES

xx

xxiii

LIST OF ABBREVIATIONS

ABBREVIATIONS

ACN	Acetonitrile
AM	Air mass 1.5 global
CB	Chlorobenzene
CBM	Conduction band minimum
CFF	3,5-Bistrifluoromethyl-Phenylammonium iodide
CV	Cyclic voltammetry
DMF	Dimethylformamide
DMSO	Dimethyl sulfoxide
DPP	Dıketopyrrolopyrrole
DSSC	Dye-sensitized solar cells
EQE	External quantum efficiency
ETL	Electron transport layer
ETM	Electron transport material
FA	Formamidinium
FAI	Formamidinium iodide
FAMA	Formamidinium methylammonium
FF	Fill factor
FPMAI	4-(furan-2-) yl)phenyl)methanaminium iodide

FTO	Fluorine-doped tin oxide
GPC	Gel permeation chromatography
HOMO	Highest occupied molecular orbital
HTL	Hole transport layer
HTM	Hole transport material
IPA	Isopropyl alcohol
IPCE	Incident Photon-to-Electron Conversion Efficiency
ITO	Indium doped Tin Oxide
JSC	Short-circuit current density
JV	Current density-voltage
LED	Light-emitting diode
LUMO	Lowest unoccupied molecular orbital
MA	Methylammonium
MAPI	Methylammonium lead iodide
MPPT	Maximum power point tracking
PCE	Power conversion efficiency
PL	Photoluminescence
PMAI	Phenylmethanaminium iodide
PSC	Perovskite solar cell
PT-TPA	.4'.4''.4'''-(pyrazine-2.3.5.6-tetrayl)tetrakis(N.N-bis(4-methoxyphenyl)aniline

PV	Photovoltaic
RH	Relative humidity
SEM	Scanning electron microscopy
SPMAI	4-(selenophene-2-yl)phenyl)methanaminium iodide
Spiro-OMeTAD	2,2',7,7'-Tetrakis-(N,N-di-4-methoxyphenylamino)-9,9'-spirobifluorene
SPO	Standing power output
TBP	4-tert-butylpyridine
TCO	Transparent conductive ox
TPMAI	4-(thiophene-2-yl)phenyl)methanaminium iodide
TRPL	Time-resolved photoluminescence
UPS	Ultraviolet photoelectron spectroscopy
UV	Ultraviolet
VBM	Valence band maximum
VOC	Open-circuit voltage
XRD	X-ray Diffraction
2D	2-dimensional

CHAPTER 1

INTRODUCTION

1.1 World Energy Consumption and Renewable Energy

Global energy consumption has increased over the past decades due to rising electricity utilization which resulted in significantly increased pollution as the majority of this energy was supplied by fossil fuels like coal, oil, and gas. It is essential to realise that although fossil fuels still provide a significant quantity of electricity, very efficient and reasonably low-cost green energy sources are required to be discovered as alternatives to non-renewable resources. The transition to renewable energy sources is being driven by a combination of factors, including the need to reduce greenhouse gas emissions, improve energy security, and reduce dependence on fossil fuels. In recent years, the cost of renewable energy technologies has also fallen significantly, making them more competitive with fossil fuels. Renewable energy refers to energy sources that are persistent or regenerates naturally but have a limiting utilization with current technologies. They are almost unlimited in duration but have a limited amount of energy per unit of time. Solar energy, wind power, geothermal energy, and hydroelectric power are all examples of renewable energy sources[1].

1.2 Solar Energy and Photovoltaics

Solar energy is a sort of renewable energy produced by harnessing the energy of the sun and its utilization is rapidly increasing in the field of renewable energy. Solar energy can be harnessed through a variety of technologies, including concentrated solar thermal and photovoltaics.

Photovoltaics (PV) is a technology that converts sunlight into electricity. PV cells are made of semiconductor materials, such as silicon, that absorb sunlight and convert it into electrical energy. The conversion of solar energy to electricity in a PV cell is a process that involves the photoelectric effect. When sunlight strikes the surface of a PV cell, it causes electrons in the semiconductor material to move, creating an electrical current.

Photovoltaic technology has been steadily improving over the past few decades, and the cost of solar energy has fallen dramatically. As a result, solar energy is becoming an increasingly popular renewable energy source in many parts of the world.

Solar cells can be classified into three generations based on the materials used to make them and the technologies employed in their production[2,3]. Here is a brief summary of the various generations of solar cells:

1. First generation (1G) solar cells: These are the earliest and most common type of solar cells, and are made of silicon[3]. 1G solar cells are highly efficient and have been the dominant technology in the solar industry for many years. 1G solar cells are durable and have a long lifespan, but they are also relatively expensive to produce and are not as flexible or lightweight as some of the newer solar cell technologies. Despite these limitations, 1G solar cells continue to be an important part of the solar energy landscape and are likely to remain so for the foreseeable future.

2. Second generation (2G) solar cells: These solar cells, also known as thin-film solar cells, are made of thin layers of semiconductor material deposited on a substrate[4,5]. 2G solar cells are typically made of materials such as amorphous silicon, cadmium telluride, and copper indium gallium selenide. 2G solar cells are less efficient than 1G cells, but they are cheaper to produce and have the potential to be more flexible and lightweight. 2G solar cells have been used in a variety of applications, including small electronic devices, portable power generators, and building-integrated photovoltaics. Despite their

potential advantages, 2G solar cells have not yet achieved widespread adoption and are still a relatively small part of the solar energy market.

3. Third generation (3G) solar cells: These solar cells, also known as advanced photovoltaics, use a variety of materials and technologies to improve efficiency and reduce cost[6–8]. Examples of 3G solar cells include perovskite solar cells, quantum dot solar cells, and dye-sensitized solar cells. One of the most important of them is perovskite solar cells that achieve high levels of efficiency and have the potential to be a low-cost alternative to traditional silicon-based solar cells. 3G solar cells are still in the research and development stage and are not yet widely available on the market. There are many studies about developing 3G solar cells and improving their efficiency and stability. 3G solar cells are anticipated to play an essential role in the future of solar energy.

1.3   Perovskite Solar Cells

Perovskite solar cell is a type of photovoltaic cell that can be used to convert sunlight into electricity. These solar cells are based on a class of materials called perovskites, with a unique crystal structure that allows them to convert sunlight into electricity efficiently. Perovskite solar cells (PSCs) are a rapidly developing technology that have the potential to revolutionize the field of renewable energy in recent years due to their high efficiency, low cost, and ease of manufacture. In fact, the efficiency of perovskite solar cells has increased significantly over the past decade, with some prototypes achieving efficiencies of over 25%[9].

One of the critical breakthroughs in the development of perovskite solar cells came in 2009 when Miyasaka *et al.* first introduced perovskite as the 'dye' in dye-sensitized solar cells (DSSCs) and obtained a PCE of 3.8% by using a mesoporous TiO_2 layer and a perovskite material based on methylammonium lead iodide $(MAPbI_3)$[8]. Hence there is a liquid corrosive electrolyte as the charge transport layer in DSSCs, the stability of that perovskite solar cell was relatively low, which brings

a limited lifetime. However, this discovery led to a surge of interest in perovskite solar cells, and over the next decade, researchers worldwide worked to improve their efficiency and stability. In 2012, Park *et al.* used a solid-state organic molecule, 2,2',7,7'-Tetrakis-(N,N-di-4-methoxyphenylamino)-9,9'-spirobifluorene (Spiro-OMeTAD), instead of the liquid electrolyte to inhibit the degradation of the perovskite absorber layer[10]. 9.7% efficiency was achieved with the integration of mesoporous TiO_2, and later on, 12% efficiency was achieved with a porous Al_2O_3 scaffold by Snaith *et al.* [11]. A 15% efficient planar structure perovskite solar cell was created in 2013. While the perovskite layer was fabricated with a solution method in former publications, Snaith *et al.* fabricated the perovskite layer via the co-evaporation method in that study. The structures for all the devices mentioned before are named as the 'n-i-p' structures (normal structure), in which the solar cell is illuminated from the electron transport layer to the perovskite layer. The first 'p-i-n' structure (inverted structure) perovskite solar cell was reported with 10% efficiency in the same year. PSCs, first produced by Miyasaka and his group in 2009, have been developed from 3.8% to 25.6%[12] through those years with several improvements and have become competitive with their strong competitors in the photovoltaic field in a short time (Figure 1-1).
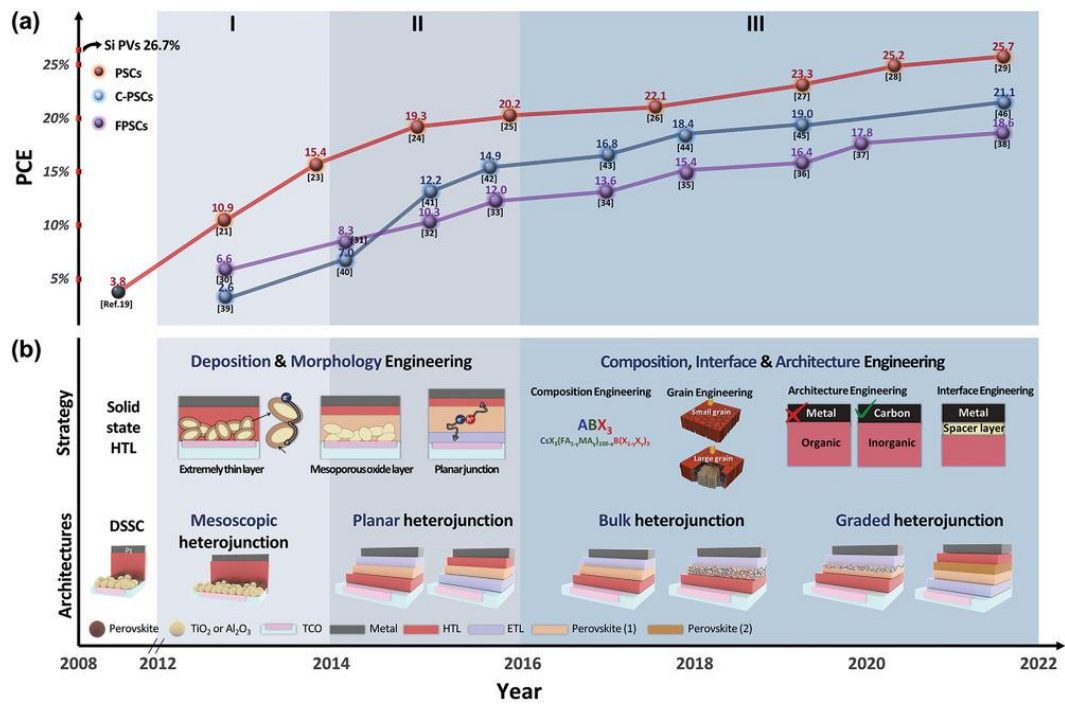
Figure 1-1. Timeline of perovskite solar cells' efficiency development[13]

The simple fabrication methods open the possibility of integrating perovskite processing into industrial roll-to-roll manufacturing, allowing low-cost mass production. The chemical tuning of the material's band gap makes it particularly interesting for application in tandem solar cells. In addition, other applications such as light emitting devices[14,15], photodetectors[16] and indoor applications[17] have been successfully demonstrated in recent years.

Perovskite solar cells have several advantages over the other solar cell technologies like their high efficiency and low cost. Some of the main advantages of PSCs include;

1. High efficiency: Perovskite solar cells have demonstrated very high levels of efficiency in converting sunlight into electricity. In 2023, the highest reported efficiency for a perovskite solar cell was just over 25%. While this is still

5

lower than the highest reported efficiency for a silicon solar cell, perovskite solar cells have the potential to achieve even higher efficiencies in the future.

2. Low-cost: Perovskite solar cells can be produced using low-cost, solution-based techniques, which makes them potentially cheaper to manufacture than silicon solar cells.

3. Thin and lightweight: Perovskite solar cells can be made using very thin films, which makes them lightweight and flexible. This makes them well-suited for use in portable devices, as well as for integration into building materials and other structures.

4. High absorption coefficient: Perovskite materials have a high absorption coefficient, which means that they can absorb a large amount of sunlight over a wide range of wavelengths. This makes them well-suited for use in solar cells.

5. High charge carrier mobility: Perovskites also have a high charge carrier mobility, which means that electrons and holes can move quickly and easily through the material. This is due to the unique crystal structure of perovskites, which allows for the efficient transport of charge carriers through the material.

6. Long diffusion length: Perovskites have a long diffusion length, which means that charge carriers can travel long distances within the material before recombining. This is important for efficiently collecting charge carriers and generating electrical power in solar cells.

The unique properties of perovskites make them highly attractive for use in solar cells and other optoelectronic devices, and ongoing research is focused on developing new and improved perovskite materials for a wide range of applications. There are several challenges that need to be addressed in order to make perovskite solar cells a viable alternative to traditional silicon-based solar cells. Nevertheless, perovskite solar cells show considerable promise with their features such as ease of application, low cost of production and excellent light absorber, as well as their maximum efficiency ratio that competes with other solar cells.

1.4   Perovskite Material

The word "perovskite" is a mineral chemical substance found in the Ural Mountains of Russia by Gustav Rose in 1839 and was named after a Russian mineralogist L. A. Perovski (1792-1856)[18]. It has a distinctive crystal structure, known as the perovskite structure, which is characterized by a cubic arrangement of metal atoms surrounded by oxygen atoms. Perovskite materials have attracted significant attention in the field of solar energy due to their high photovoltaic efficiency and low cost of production[19].

Perovskite materials are a class of compounds that have a specific crystal structure and chemical composition and are composed of an organic and metal cation and a halide anion. Figure 1-2 demonstrates the general formula for perovskite, ABX_3, where A can be an organic (the most common methyl ammonium (MA^+) or formamidinium (FA^+)) or inorganic cation (Cs^+), B is a metal cation (Pb^{2+} or Sn^{2+}), and X is a halide anion or a mixture of halogens (I^-, Br^-, or Cl^-). In the perovskite structure, the A cation is located at the corners of the unit cell, the X anion is located at the center of each face of the unit cell, and the B cation is located at the center of the unit cell. The A cations and X anions form a simple cubic lattice, and the B cation is coordinated to twelve X anions, forming a slightly distorted octahedron.

Perovskite solar cells (PSCs) are a hybrid system, a combination of organic and inorganic components, and organic-inorganic lead halide hybrid perovskite is now the most common perovskite material in photovoltaics. The perovskite crystal structure can accommodate a wide variety of cations and anions, leading to the formation of many different perovskite compounds. Generally, the most commonly used perovskite structure is methylammonium lead iodide, MAPI.
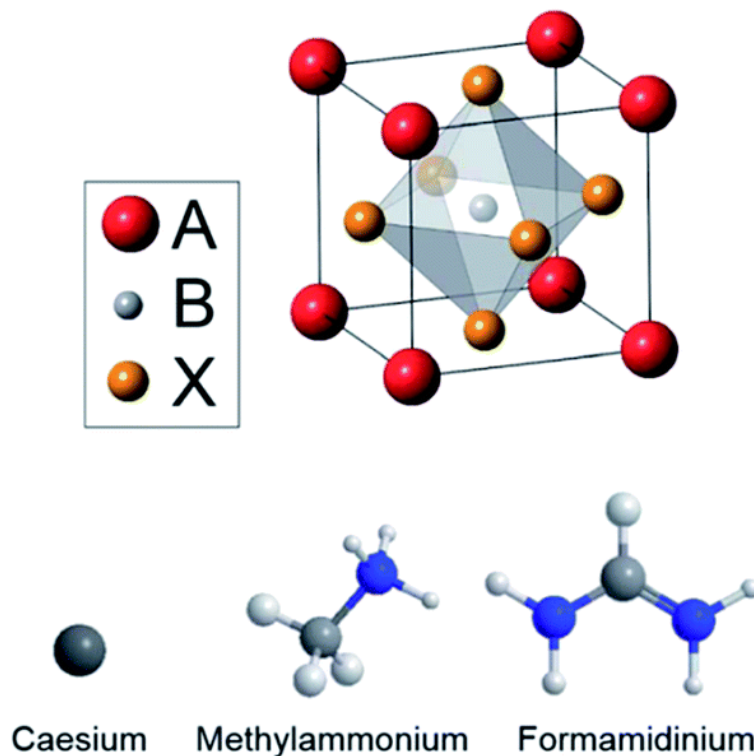
Figure 1-2. ABX$_3$ perovskite unit cell. A(grey)=CH$_3$NH$_3$, B(blue)=Pb or Sn, O (violet)=I, Br or Cl[20].

1.5   Perovskite Solar Cell Structure and Working Principle

Perovskite solar cells have a layered structure similar to traditional solar cells, with some key differences in the materials used. In solar cells, perovskite materials are used as the active layer, which is responsible for converting sunlight into electricity. When sunlight hits the perovskite layer, it excites the electrons in the material, causing them to jump to a higher energy level. These excited electrons are then collected by electrodes and transported to the electrical circuit, where they can be used to generate electricity.

A perovskite solar cell is a combination of three layers. The layers of a perovskite solar cell can be explained basically as follows;

1. Substrate: This is the base layer on which the other layers of the solar cell are deposited. The substrate is generally made of glass.

2. Electrode: The electrode is a layer of conducting material that is deposited on the substrate. It serves as the connection point for the electrical current that is generated by the solar cell.

3. Perovskite layer: This is the active layer of the solar cell that absorbs sunlight and generates an electrical current.

4. Electron transport layer (ETL): The ETL is a layer of material that is responsible for transporting negative charge carriers (electrons) from the perovskite active layer to the electrodes. A material's LUMO (least unoccupied molecular orbital) level must be compatible with the perovskite absorber layer to be employed as an electron transport material (ETM).

5. Hole transport layer (HTL): The HTL is a layer of material that is responsible for transporting positive charge carriers (holes) from the perovskite active layer to the electrodes. Hole transport material (HTM) must have a slightly higher occupied molecular orbital (HOMO) than the perovskite absorber layer.

6. Counter electrode: The counter electrode is the second electrode of the solar cell, and it is typically made of a material such as gold or silver.

The working principle of a perovskite solar cell is similar to that of other photovoltaic cells where sunlight is converted into electric power. The working mechanism of a perovskite solar cell can be explained in the following steps:

1. Absorption of sunlight: When sunlight falls on the perovskite solar cell, the photons are absorbed by the perovskite layer.

2. Excitation of electrons: The absorbed photons cause the electrons in the perovskite layer to get excited and move from the valence band to the conduction band. This creates electron-hole pairs in the perovskite layer.

3. Separation of electrons and holes: The excited electrons are free to move, and they move towards the electron transport layer. The holes move towards the hole transport layer (HTL).

4. Collection of electrons: As the electrons move towards the electron transport layer, they are collected by the electrodes. This generates an electric current that can be used as a source of power.

PSCs also have some common radiation recombination mechanisms, like silicon solar cells. It is important to prevent the recombination of the electrons and holes to maintain the efficiency of the solar cell. The HTL is designed to transport the holes quickly to prevent recombination with the electrons in the perovskite layer. Limiting these charge recombination processes may improve the device efficiency in perovskite solar cells. Figure 1-3 depicts the whole charge transport/recombination process: Through the transparent electrode, photons excite the perovskite layer, resulting in the photogeneration of electron-hole pairs. Electrons and holes are separated (1) and delivered into the conduction band of the ETL (2) and the HOMO level of the HTL (3), respectively, forward travelling to the electrodes. Due to recombination processes that can occur between the ETL, the perovskite layer, and the HTL, there are unwanted photovoltage losses (5, 6 and 7). Nonradiative recombination (4) also can occur.
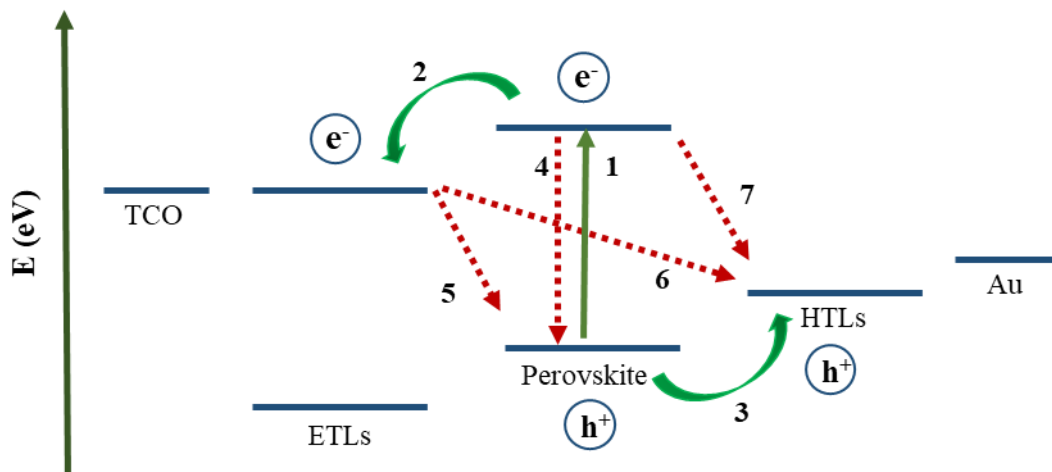
Figure 1-3. Processes in PSCs involving charge transport and recombination: 1. charge generation, 2 and 3. charge transport of the electrons and holes to the ETL and HTL, respectively, 4, 5, 6, and 7. recombination processes.

Overall, the structure of a perovskite solar cell is designed to optimize the absorption of sunlight and the generation of electricity while also ensuring good charge transport and stability.

1.6   Device Configurations of Perovskite Solar Cells

Perovskite solar cells have been fabricated using two distinct device designs, n–i–p and p–i–n. The cell structure changes according to the direction of the light in PSCs. The key difference between the two structures is the position of the perovskite layer between the charge transport layers.

Normal structure (n-i-p) is adopted from dye-sensitized solar cell structure. If the light comes from the electron transport layer (ETL) and reaches the perovskite active layer, it is called the normal structure. The general structure of a normal perovskite solar cell consists of a TCO layer as the bottom electrode, an ETL, a perovskite absorber layer, a HTL, and a top electrode. If it comes from the hole transport layer (HTL) and reaches the perovskite active area, it is called the inverted structure (p-i-n). In contrast, the general structure of an inverted perovskite solar cell consists of a transparent conductive oxide (TCO) layer as the bottom electrode, a hole transport layer (HTL), a perovskite absorber layer, an electron transport layer (ETL), and a top electrode. (Figure 1-4).
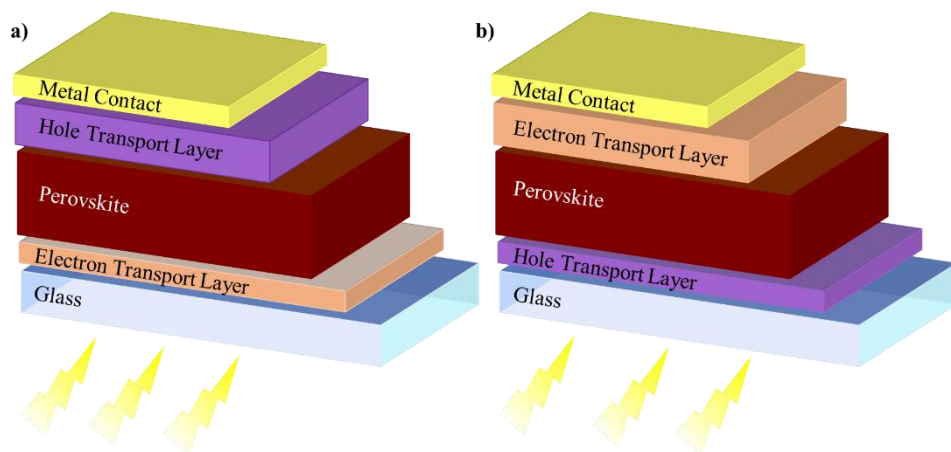
Figure 1-4. Perovskite solar cell architecture, a) normal structure (n-i-p), b) inverted structure (p-i-n)

1.7 Fabrication Techniques of Perovskite Solar Cells

The fabrication process of PSCs involves several steps, including the preparation of the perovskite material, deposition of the charge transport layers, and encapsulation. The performance and stability of PSCs are strongly influenced by the fabrication technique used. Perovskite solar cells can be fabricated using a variety of techniques, including solution processing and vapour deposition.

a) Solution-based Methods:

Solution-based methods are the most commonly used techniques for fabricating PSCs due to their simplicity and low cost. The most commonly used solution-based technique is spin-coating, which involves depositing a solution of perovskite precursors onto a substrate and spinning it at high speed to form a thin, uniform film. The substrate is then annealed to form the perovskite layer.

Another solution-based technique is inkjet printing, which involves depositing small droplets of perovskite precursors onto a substrate using an inkjet printer. This technique offers precise control over the deposition of the perovskite material and

can be used to create complex patterns. Other techniques that have been used generally to fabricate large-area perovskite solar cells include blade coating, spray coating, and doctor blading. Each of these techniques has its own advantages and disadvantages, and the best technique for a given application will depend on the specific requirements and constraints of the system.

Solution-based techniques offer several advantages, including low cost, scalability, and ease of processing. However, they also suffer from poor reproducibility and can result in non-uniform films, leading to reduced performance and stability of PSCs.

    b) Vacuum-based Methods:

Vacuum-based methods, such as thermal evaporation and sputtering, are less commonly used for fabricating PSCs due to their complexity and cost. However, they offer several advantages over solution-based techniques, including better film uniformity, precise control over film thickness, and the ability to deposit multiple layers.

Thermal evaporation involves heating the charge transport materials in a vacuum chamber, causing them to evaporate and condense onto the substrate. Sputtering involves bombarding the charge transport materials with high-energy ions, causing them to eject and deposit onto the substrate.

Vacuum-based methods offer better control over film thickness and uniformity, resulting in improved performance and stability of PSCs. However, they are more complex and expensive than solution-based techniques.

1.8   Charge Transport Layers

The photovoltaic processes include the subsequent steps: i) absorption of light, ii) electron/hole separation, and iii) charge transport and collection. One of the key challenges in PSCs is to achieve efficient charge transport through the device. For

high efficiency in PSC devices, fast charge carrier transport with a low charge recombination rate is frequently required.

In a perovskite solar cell, the charge transport layers are responsible for transporting charge carriers (electrons and holes) from the active layer to the electrodes, where they can be collected as electrical current. There are two main types of charge transport layers in a perovskite solar cell: the hole transport layer (HTL) and the electron transport layer (ETL). A variety of materials have been used as HTL and ETL in PSCs, including organic and inorganic materials.

The hole transport layer (HTL) is a layer of material that is responsible for transporting positive charge carriers (holes) from the perovskite active layer to the electrodes. The HTL plays a critical role in the overall performance of the solar cell, as it helps to improve the efficiency of the device by facilitating the flow of charge carriers. For HTLs, materials such as Spiro-OMeTAD[21], PTAA[22], PEDOT:PSS[23], and P3HT[24] have been widely used.

The electron transport layer (ETL) is a layer of material that is responsible for transporting negative charge carriers (electrons) from the perovskite active layer to the electrodes. The ETL helps to ensure that the electrons are efficiently collected at the electrodes, which is important for the overall performance of the solar cell. For ETLs, materials such as SnO_2[25], TiO_2[26], and ZnO[27] have been commonly used.

There are several factors that can affect the performance of the charge transport layers in a perovskite solar cell. These include the material used for the layers, the thickness of the layers, and the quality of the interface between the layers and the other layers of the solar cell. Especially in recent years, the diversification and development of transport layers have played a significant role in achieving high-performance perovskite solar cells. Normal solar cells are of interest because of the structure where perovskite studies start and their high-efficiency structure.

1.8.1 Electron Transport Layer

The electron transport layer (ETL) is an essential component of perovskite solar cells, responsible for efficiently transporting electrons from the perovskite layer to the cathode electrode. The ETL serves several functions in perovskite solar cells. First, it acts as an electron-selective contact, blocking the transport of holes from the perovskite layer to the cathode electrode. This helps to maintain a high open-circuit voltage and prevent recombination of electron-hole pairs. Second, the ETL provides a pathway for electrons to flow from the perovskite layer to the cathode electrode, where they can be collected and used to power devices or stored in a battery.

The titanium dioxide (TiO_2) layer has been the most widely used electron transport layer (ETL) in normal structure perovskite cells and has helped to achieve high efficiencies in solar cells. However, alternative electron transport layers have been developed that can be used instead of TiO_2 because it is not very stable under UV light, its electron transport properties are not good enough, and in addition, very high temperatures are required for its production which inclined the literature for using new ETMs[28]. The tin oxide (SnO_2) has started to be used rather frequently instead of TiO_2 because of its advantages such as better optical and electrical properties according to the TiO_2, better energy band compatibility with the perovskite layer, and being able to be produced at low temperatures. Firstly, in 2015, 17% efficiency value was obtained from the planar perovskite solar cell produced using SnO_2 nanocrystals[29] and 21% cell efficiency was reached within two years[30]. For these reasons, the SnO_2 layer was used as the electron transport layer in this thesis work.

1.8.2 Hole Transport Layer

The HTL plays a critical role in maintaining the high efficiency of perovskite solar cells. The hole transport from the perovskite layer to the back-contact metal electrode takes place by HTL. The HTL plays a critical role in the overall performance of the

solar cell, as it helps to improve the efficiency of the device by facilitating the flow of charge carriers.

There are several factors that can affect the performance of the HTL in a perovskite solar cell. These include the material used for the HTL, the thickness of the layer, and the quality of the interface between the HTL and the other layers of the solar cell.

Multiple properties of HTM have been revealed in PSCs, along with the following: a) It functions as a barrier between the perovskite layer and the metal electrode, which improves device stability and effectively prevents electron transmission from the perovskite layer to the anode. b) Since HTM has high hole mobility properties, it improves the hole transport in PSCs. c) HTL plays a vital role in terms of the long-term stability of solar cells. In the normal structure (n-i-p), the HTL covers the perovskite layer and protects the perovskite from external stimuli, like water. Therefore, the hydrophobic hole transport layer is essential to keep the perovskite from absorbing moisture from the air. HTM works as moisture or metal ion diffusion barrier, mitigating PSC degradation. The literature indicates that HTM covers perovskite more effectively than TCO/perovskite/metal[31].

The performance of hole transport layers (HTLs) in perovskite solar cells (PSCs) is influenced by various factors. The followings are the primary prerequisites for an HTM to transport hole efficiently in PSCs:

a) Energy Level Alignment: The energy level alignment between the HTL and the perovskite layer is critical for efficient hole transport in PSCs. The energy level of the HTL should be well-matched with the valence band of the perovskite layer to ensure efficient hole extraction (no more than 0.3 eV). If the energy levels are not aligned properly, the holes can be trapped in the perovskite layer, resulting in a decrease in the power conversion efficiency (PCE) of the device.

a) Hole Mobility: The mobility of holes through the HTL is another essential factor that affects the performance of PSCs. The HTL should have high hole

16

mobility to facilitate efficient hole transport to the anode. The mobility of holes depends on the structure and composition of the HTL. For instance, inorganic materials such as CuSCN[32] and NiO_x[33] have demonstrated high hole mobility, while organic materials such as Spiro-OMeTAD have relatively lower mobility. The addition of dopants may improve the low mobility of HTM.

b) Conductivity: The conductivity of the HTL is also an important factor that affects the performance of PSCs. The HTL should have a high conductivity to facilitate efficient charge transport to the anode. High conductivity can be achieved by optimizing the doping concentration and structure of the HTL.

c) Thickness: The thickness of the HTL can also affect the performance of PSCs. The HTL should be thin enough to allow efficient charge extraction but thick enough to prevent shunting or shorting between the anode and cathode. An optimal thickness can be determined experimentally by varying the thickness of the HTL and measuring the performance of the device.

d) Stability: The stability of the HTL is also an important factor that affects the performance of PSCs. The thermal, photochemical, and environmental stability of HTM is crucial. The HTL should be stable under ambient conditions to ensure long-term device stability.

e) Solubility: The HTM needs to be soluble in a solvent that can be used to prepare a uniform and defect-free thin film on the surface of the perovskite layer. The solvent should have a high boiling point to enable slow evaporation and sufficient time for the HTM molecules to rearrange and form a dense, continuous film. The solvent should also be compatible with the perovskite layer and not cause any damage or degradation.

f) Film forming: The HTM should have high charge mobility and conductivity to facilitate efficient charge transport and extraction from the perovskite layer to the electrode. This is important for achieving high device efficiency and stability.

Some common materials that are used for the HTL in perovskite solar cells include spiro-OMeTAD, which is a conductive organic material, and inorganic materials such as titanium dioxide (TiO_2) and zinc oxide (ZnO). Figure 1-5 is a schematic of a "efficiency tree" that illustrates the HTMs applied to PSCs with the highest levels of efficiency (>21%)[34].
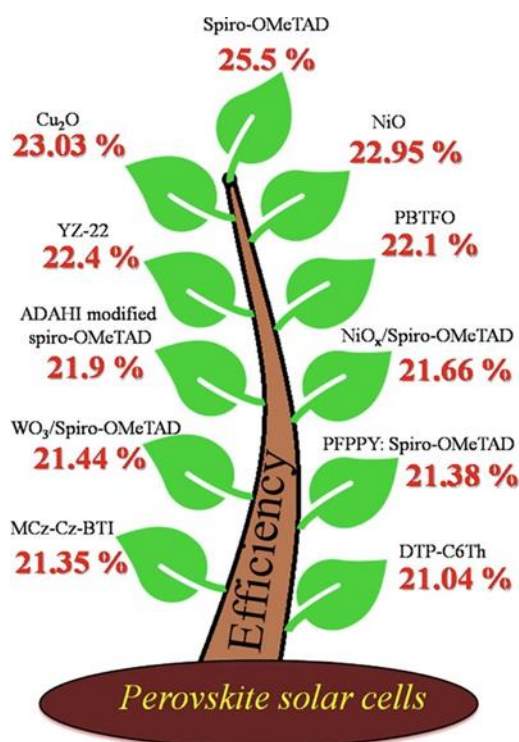
Figure 1-5. Schematic of the hole transport layers with the highest efficiency[34]

A distinct problem with hybrid organic/inorganic PSCs is that the perovskite cannot tolerate aggressive processing throughout subsequent layer deposition. For instance, various inorganic materials, including copper iodide, nickel oxide, and copper oxide, have been investigated as alternatives to PSC for HTLs[35]. While these materials may provide better durability, they frequently need incompatible or high processing temperatures, making oxide-based HTLs only attractive for devices with p-i-n architecture (which requires substrate/HTL/perovskite/ETL), not treated on top of the fragile perovskite film[36–39]. For this reason, the vast bulk of perovskite solar cell

research, particularly record-breaking efficiency, has been based on organic-based HTL PSC designs.
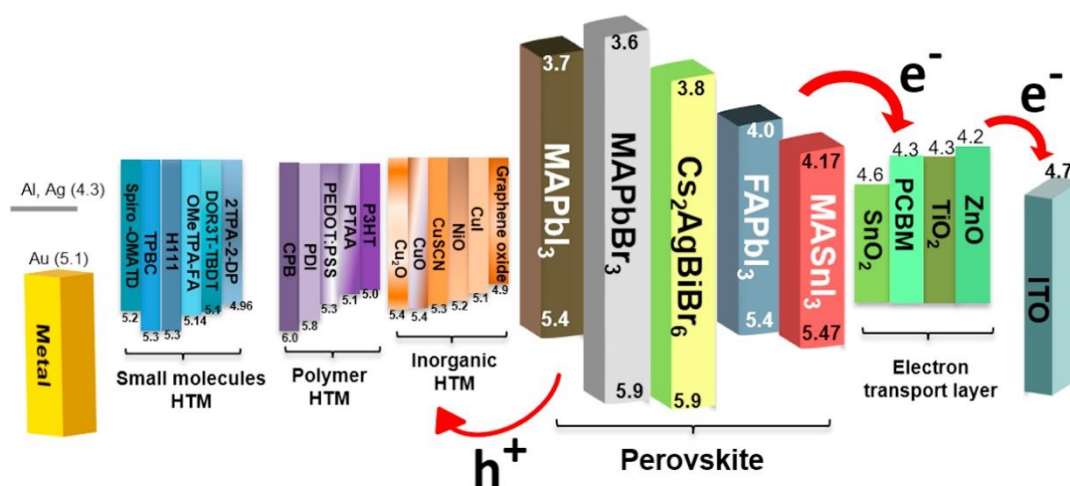
Figure 1-6. Energy levels of various common HTMs together with iodide and bromide based halide-perovskites[40].

Organic polymers, such as poly[bis(4-phenyl)(2,4,6-trimethylphenyl)amine (PTAA), poly(3,4-ethylenedioxythiophene) polystyrene sulfonate (PEDOT:PSS), and poly(3-hexylthiophene) (P3HT), have been reported to be efficient HTLs due to their comparatively high intrinsic conductivities and mobilities[41]. With the exception of PEDOT:PSS, which has been proven to be hydrophilic, organic polymers are solution-processable, exhibit good thermal stability, and are hydrophobic[39–45].

Small molecule-based HTLs also are highly adaptable in terms of property tuning (e.g., energy tuning, hydrophobicity, film morphology, etc.) and exhibit excellent batch-to-batch consistency in not only synthesis and purification but also device manufacturing because organic small molecule (OSM) HTLs are often amorphous[46–52].

1.8.2.1 Spiro-OMeTAD and Doping of HTM

Spiro-OMeTAD was discovered and authorized by Merck almost twenty years ago[53,54]. Kim *et al.* first utilized Spiro-MeOTAD as the HTL in the mesoporous structured MAPbI$_3$ PSCs with an efficiency of around 10%. Since then, spiro-OMeTAD remains the most studied HTM for n-i-p perovskite solar cells due to its potential to produce devices with higher performance.

The LUMO and HOMO of spiro-OMeTAD align favorably with the conduction band minimum (CBM) and valence band maximum (VBM) of perovskite, respectively, in PSCs. Dopants and additives to organic HTMs and derivatives of the HTMs thus have the potential to enhance the performance of PSCs significantly. However, pristine spiro-MeOTAD has limited conductivity and hole mobility. Noh *et al.* have doped spiro-OMeTAD with bis(trifluoromethylsulfonyl) amine lithium salt (Li-TFSI), 4-tert-butylpyridine (TBP), and tris(2-(1H-pyrazol-1-yl)-4-tert-butylpyridine)cobalt(III) tri[bis(trifluoromethane)sulfonimide] (FK209) to minimize the charge transport resistance in 2013[55] (Figure 1-7). The combined use of LiTFSI and TBP in Spiro-OMeTAD enhanced its conductivity by two orders of magnitude, from 2.5×10^{-7} Scm^{-1} to 2.5×10^{-5} Scm^{-1}, and the incorporation of FK209 enhanced conductivity further, resulting in a drop in series resistance from 94.7Ω to $65.8\ \Omega$[56,57]. In addition, these additives or dopants decreased the fermi level and carrier recombination of Spiro-OMeTAD.

LiTFSI
Lithium
bis(trifluoromethane)sulfonimide

FK 209 Co(III) TFSI salt
tris(2-(1*H*-pyrazol-1-yl)-4-*tert*-butylpyridine)cobalt(III)
tri[bis(trifluoromethane)sulfonimide]

***t*BP**
4-*tert*-Butylpyridine
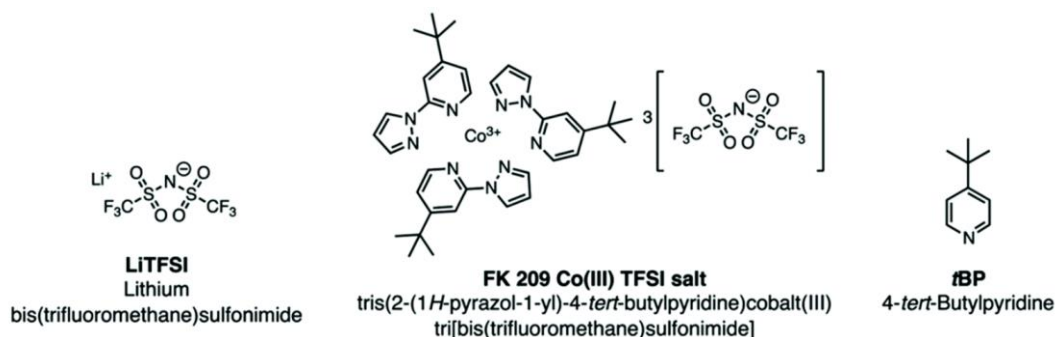
Figure 1-7. Chemical structures of conventional spiro-OMeTAD dopants.

Doping is a method for enhancing the conductivity of semiconductors, in which an impurity is added to the semiconductor to elevate the concentration of majority charge carriers and raise conductivity[58]. The doping mechanism of Spiro-OMeTAD involves the introduction of impurities into the material that alter its energy levels and electrical conductivity. The doping process involves adding the dopant molecule to a solution of Spiro-OMeTAD in a solvent such as chlorobenzene. The solution is then spin-coated onto the perovskite layer, forming a thin layer of doped Spiro-OMeTAD as the hole transport layer (HTL). The dopant molecules can improve the conductivity of the Spiro-OMeTAD layer, resulting in improved device performance. Spiro-OMeTAD is p-doped by oxidation to spiro-OMeTAD$^+$[59]. This also deepens its HOMO, which may improve the energy alignment at the interface between Spiro-OMeTAD and perovskite[60]. Despite the fact that Spiro-OMeTAD oxidation was observed even in the absence of p-dopants, the rate was too low to appreciably alter conductivity[61]. Even though the electrical characteristics of doped Spiro-OMeTAD provide for high-efficiency devices in a research context, its stability poses a significant obstacle.

1.9   Challenges of Perovskite Solar Cells

Despite those advantages, there are a couple of challenges that need to be overcome. One of the major challenges is the stability problem. Perovskite solar cells tend to degrade over time, particularly when exposed to moisture or heat. This limits their lifetime and makes them less reliable than silicon solar cells. Complexity of the fabrication processes is another one. The process of fabricating perovskite solar cells is relatively complex and requires specialized equipment and expertise. This makes it more difficult to scale up production compared to silicon solar cells. Additionally, there can be significant losses at the interface between the perovskite layer and the charge transport layers, which can reduce the overall efficiency of the cell. Lastly, perovskite solar cells are not yet widely available commercially, and it will likely take some time before they are mass-produced and widely adopted.

1.9.1 Hysteresis

Hysteresis is a phenomenon that can occur in perovskite solar cells, in which the current-voltage (J-V) curve of the device exhibits a loop or hysteresis when the voltage is swept back and forth under constant illumination. This can be a problem for perovskite solar cells, as it can lead to reduced efficiency and stability.

Although the origin of hysteresis in PSCs is still not fully understood, it is related to the complex interplay between charge transport, recombination, and ion migration within the device. One proposed mechanism is that hysteresis is caused by the accumulation of mobile ions, such as lead iodide (PbI_2) and/or methylammonium lead iodide ($MAPbI_3$), in the perovskite layer. These ions can move under the influence of the applied electric field and affect the band alignment at the interfaces, resulting in changes in the current flow and device performance. Another proposed mechanism is that hysteresis is caused by slow charge accumulation and release processes in the perovskite layer, which can result in different transient current responses during the voltage sweep. This can lead to a delay in the response of the device to changes in the applied voltage, resulting in hysteresis.

Significant hysteresis can occur in the current-voltage curves of perovskite solar cells measured at specific scan settings. As demonstrated in Figure 1-8, the photocurrent of the reverse scan is always higher than the photocurrent of the forward scan. Due to this occurrence, reporting the device performance is more challenging: The device performance cannot be accurately represented by any scan direction.
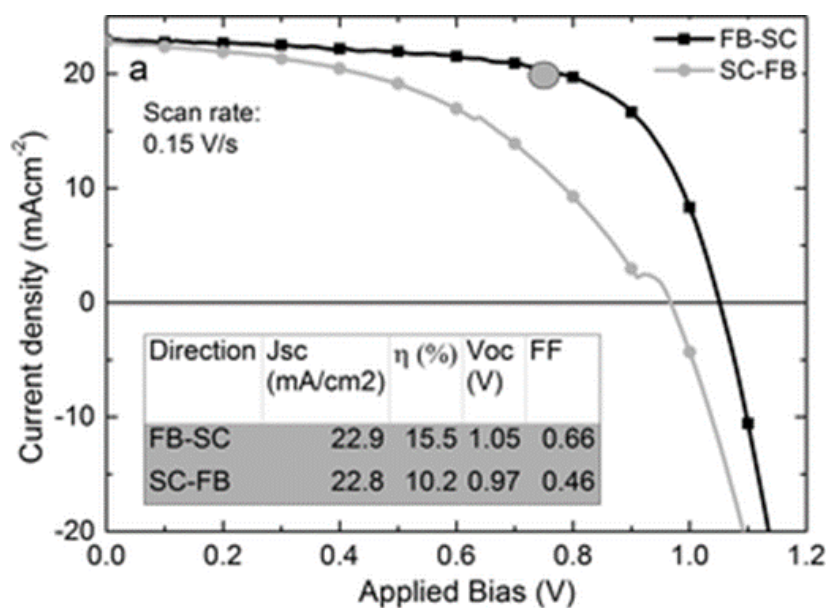
Figure 1-8. Hysteresis in PSCs: forward and reverse scan of a device with different J-V curves[62].

There are several factors that can contribute to hysteresis in perovskite solar cells. The main reasons of hysteresis can be ascribed as; the ion migration in the perovskite film[63], the ferroelectricity of the perovskite compound[64] and the ion diffusion across the hole transport layer and perovskite films[65]. Even though there are many studies about the hysteresis problems in perovskite solar cells, relatively little work has been done to establish a synergistic knowledge of the interaction between the structure-property relationship of perovskite and the origin of hysteresis.

1.9.2　Stability

Although PSCs are quite good at converting photon energy into electrical energy, there are still challenges to overcome before this technology can be commercialized. Stability is an important consideration for perovskite solar cells, as the performance of these devices can degrade over time due to various factors such as exposure to light and heat, and the presence of defects or impurities in the perovskite material.

The stability of the perovskite devices is the main limitation in that way. Perovskite is structurally unstable when exposed to oxygen, heat (thermal instability), humidity (moisture and air), and light for an extended period (Figure 1-9).
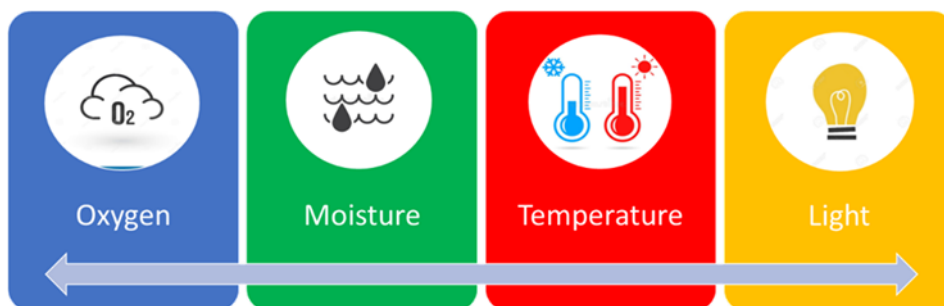
Figure 1-9. Components affect the stability of perovskite

There are several ways in which researchers are trying to improve the stability of perovskite solar cells. One approach is to optimize the layers of the perovskite solar cells to reduce the number of defects and improve its stability. Another approach is to use protective coatings or encapsulation techniques to shield the perovskite material from the environment and prevent degradation.

Development of more stable PSCs is a conspicuous area of research as well as achieving high efficiency solar cells. In recent years, there are quite a lot work on ways to improve the long-term stability of PSCs.

1.9.3 Defects and Charge Traps

One of the main challenges that limit the performance and stability of PSCs is the presence of defects and charge traps in the perovskite layer. Defects in the perovskite material can negatively impact the performance of the solar cell by reducing the efficiency and stability of the cell.

Defects in the perovskite layer can arise from various sources, such as crystal defects, grain boundaries, surface defects, and impurities. These defects can act as trapping centers for charge carriers, leading to a reduction in the carrier mobility and lifetime[66]. The presence of defects can also increase the density of trap states, resulting in a reduction of the open-circuit voltage (V_{oc}) and fill factor (FF). Charge traps can be created in PSCs due to the presence of interface states between the perovskite layer and the charge transport layers. Charge traps, which are regions within the material where charge carriers become trapped and cannot contribute to the current, can reduce the performance of the cell[67,68]. Uncoordinated ions such as Pb^{2+} and the accompanying dangling bonds at grain boundaries and surfaces are assumed as the significant causes of charge traps[69,70].

Passivation is a technique used to reduce the effects of defects and charge traps in perovskite solar cells[71]. This can be achieved by using passivating layers or by introducing passivating agents into the perovskite material. The passivating layers or agents help to reduce the number of defects and charge traps in the material, which in turn improves the performance of the solar cell.

Additive engineering has been applied to control crystal growth and grain size, passivate defects, improve charge transport, and develop a moisture barrier with the purpose of enhancing PCE and stability.

Additive engineering is a technique used to enhance the stability and efficiency of perovskite solar cells. It involves the addition of various materials to the perovskite layer to enhance its properties. Some examples of additive engineering techniques used in perovskite solar cells include:

- Doping: Doping is explained as introducing impurities into the perovskite layer to change its electrical properties. For example, by introducing a small amount of iodine or bromine into the perovskite layer, the bandgap of the material can be adjusted to improve its light-absorption efficiency.

- Interfacial engineering: Interfacial engineering involves the modification of the interlayer between the perovskite layer and the electrodes.

- Surface modification: Surface modification of the perovskite layer can also improve its performance and stability. For example, by adding small amounts of hydrophobic molecules to the perovskite surface, the material becomes more stable against moisture and humidity.

As a result, additive engineering is a powerful tool for improving the performance and stability of perovskite solar cells, and it is an active area of research in the field.

1.10 Aim of the Thesis

The aim of this thesis is to investigate new materials and methods for improving the performance of perovskite solar cells by developing HTLs with improved properties. The thesis would also aim to investigate the relationship between the properties of the HTLs and the performance of the solar cells and identify the optimal conditions for using these novel HTLs in perovskite solar cells. The research methodology would include the design and synthesis of novel HTL materials and their characterization using various techniques. The performance of perovskite solar cells incorporating these HTLs would be evaluated and compared to reference cells with commonly used HTLs. The results and findings of the research are presented and discussed in the thesis, highlighting the properties of the novel HTLs and their impact on the performance of perovskite solar cells. The thesis is concluded with a discussion of the implications of the research and suggestions for future work.

The introduction of the thesis would provide a background of the current state of perovskite solar cell technology, highlighting the importance of the HTLs and the current limitations of the existing materials. In chapter 2, fabrication methods and characterization techniques were explained. Chapter 3 focuses on DPP-based polymers as a hole transport layer. Chapter 4 includes a small organic molecule as hole transport material in the perovskite solar cell system. In Chapter 5, a new p-type dopant for the Spiro-OMeTAD hole transport layer is presented. In Chapter 6 the passivation of the perovskite active layer via ammonium salts in perovskite solar cells is introduced. Chapter 7 summarizes the whole study in this thesis and discusses future work.

In summary, the aim of this thesis is to investigate new materials and methods for improving the performance of perovskite solar cells by developing HTLs with improved properties and to identify the optimal conditions for using these novel HTLs in perovskite solar cells.

CHAPTER 2

EXPERIMENTAL METHODS

2.1   Device Performance Parameters

The performance of perovskite solar cells is often evaluated using several key parameters. Some of the most essential device performance parameters of perovskite solar cells include:

- Power conversion efficiency (PCE): This is the most commonly used parameter to evaluate the performance of solar cells. It is defined as the ratio of the electrical power output to the incident light power. PCE is calculated from the below equation:

$$\eta = (V_{MP} \times J_{MP}) \div (V_{oc} \times J_{sc})$$
$$\eta = (V_{oc} \times J_{sc} \times FF) \div (P_{in})$$

- Fill factor (FF): This parameter describes how well the current-voltage (I-V) characteristics of the solar cell match the ideal characteristics. A fill factor of 1 indicates a perfect match, while a fill factor of less than 1 indicates that the I-V characteristics deviate from the ideal. FF is calculated from the below equation:

$$FF = (V_{MP} \times J_{MP}) \div (V_{oc} \times J_{sc})$$

- Open circuit voltage (V_{oc}): This parameter is the voltage at which the solar cell generates no current. The higher the open-circuit voltage, the more energy can be harvested from the solar cell.
- Short circuit current (J_{sc}): This parameter is the current generated by the solar cell when a short circuit is applied across the electrodes. The higher the short-circuit current, the more energy that can be harvested from the solar cell.

29

Another important parameter is incident photon-to-current efficiency (IPCE). ICPE is a measure of the efficiency of a solar cell in converting incident light into electrical current. In perovskite solar cells, IPCE is a valuable metric that gives insight into the device's performance under different light conditions. It is defined as the ratio of the photocurrent density to the incident photon flux density and is typically measured as a function of the wavelength of the incident light.

The IPCE spectrum allows researchers to identify the range of wavelengths for which the solar cell is most efficient and can help to identify the underlying mechanisms responsible for light absorption and charge generation in the device.

The IPCE of perovskite solar cells can reach above 80% in a wide range of wavelengths, which allows the cells to efficiently convert a wide range of light into electrical energy. However, the IPCE also depends on the device configuration and the quality of the perovskite layer, and it's affected by factors such as recombination, trap states, and interface defects.

2.2   Device Fabrication Procedure

This thesis's device construction is based on the typical materials used in n-i-p perovskite solar cells, as described in Chapter 1: $ITO/SnO_2/Perovskite/HTL/Au$. However, in Chapters 4 and 5, an electron-blocking MoO_3 layer with a thickness from 0 to 20 nm is introduced after the HTL deposition and evaporated before metal contact. Schematics of different device structures were given in Figure 2-1.
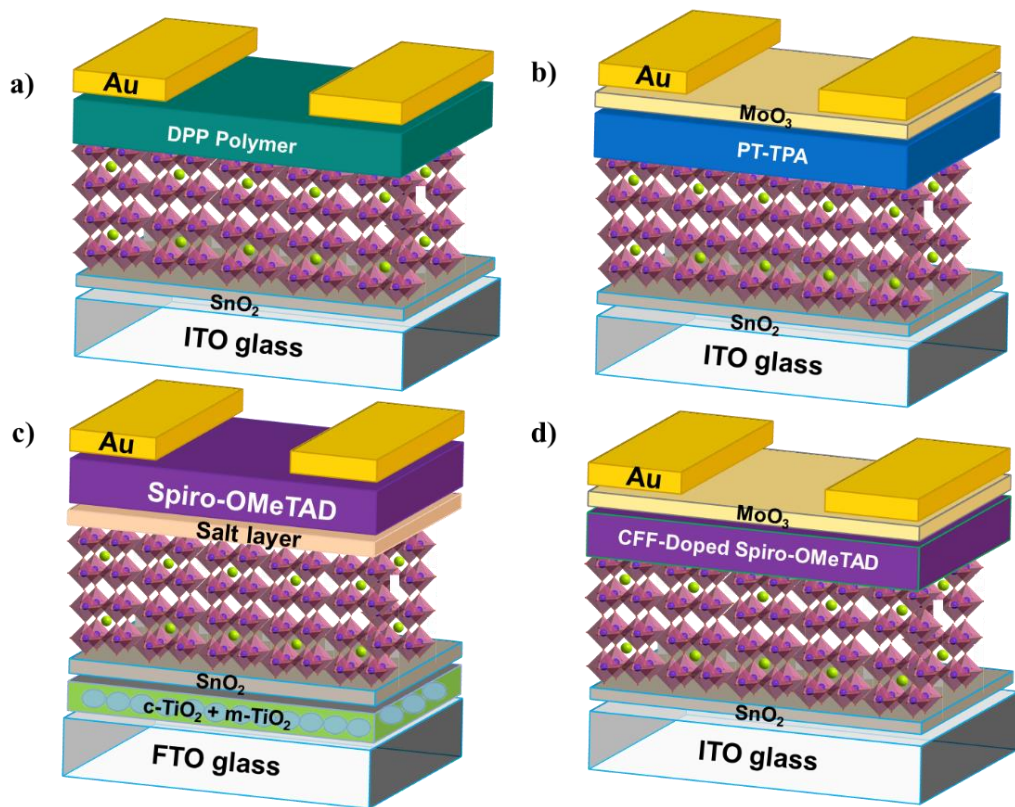
Figure 2-1. Schematics of device structures of a) DPP Polymers HTLs, b) PT-TPA HTL, c) Salt passivated PSC and d) CFF-doped PSC

The perovskite solar cell fabrication for Chapter 3, 4 and 5 is as follows;

Indium tin oxide (ITO) coated glass substrates were washed with Hellmanex (2%), deionized water, acetone and isopropanol (IPA) for 10 minutes, respectively. Then UV-ozone was applied for 10 minutes to remove organic residues on the surface. Then, the tin oxide (SnO_2) solution was spin-coated at 4000 rpm for 30 seconds and annealed at 150℃ for 30 minutes. The perovskite absorbing layer and hole transport layer are deposited within a glove box containing a nitrogen (N_2) atmosphere under vacuum conditions. For the perovskite layer, 1.3 M of lead iodide (PbI_2) dissolved in DMF:DMSO = 9.5:0.5; on the other hand, 60 mg:6mg:6 mg of formamidinium Iodide (FAI), methylammonium bromide (MABr) and methylammonium chloride (MACl), respectively, was dissolved in 1 ml of IPA. The precursor solution was

31

coated for 45 seconds at 3000 rpm and annealed at 125°C for 5 minutes. Then, for reference cells, 54.2 mg of Spiro-OMeTAD was dissolved in 750 µL of chlorobenzene and supplemented with 21.6 µL of TBP and 13.12 µl of Li-TFSI. The solution was coated by spinning at 3000 rpm for 30 seconds. The novel hole transport materials were dissolved with the appropriate concentration and coated on the perovskite layer instead of Spiro-OMeTAD. Then, 80 nm gold (Au) was coated by the evaporation method (Figure 2-2).
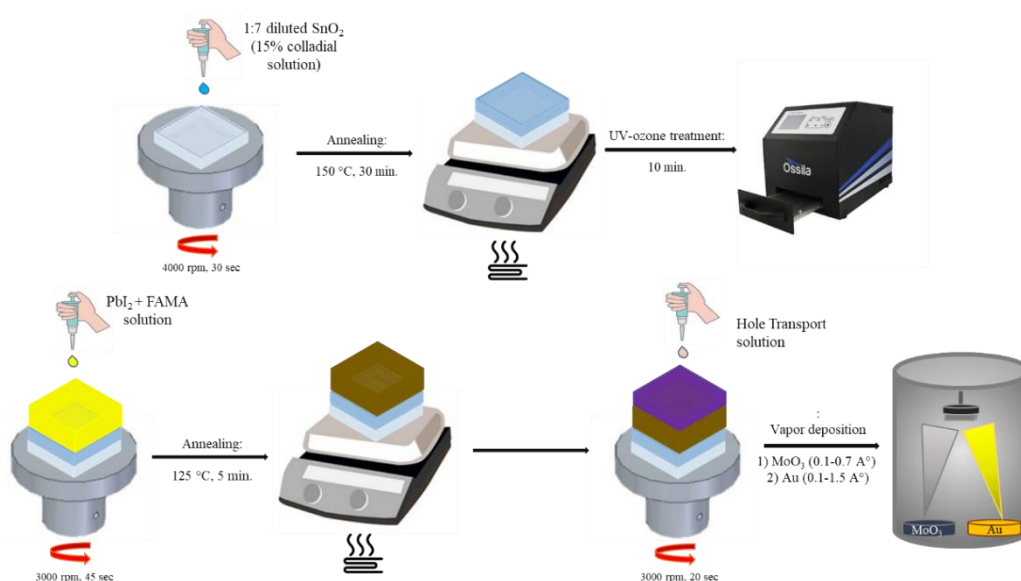
Figure 2-2. Schematic of fabrication of perovskite solar cell

The following is the perovskite solar cell fabrication procedure for Chapter 6:

Fluorine-doped tin oxide (FTO) substrates were washed with Hellmanex (2%), deionized water, acetone and isopropanol (IPA) for 10 minutes, respectively. Then UV-ozone was applied for 15 minutes to remove organic residues on the surface. Then, titanium diisopropoxide bis-(acetylacetonate) solution diluted in IPA at a 1:15 volume ratio to form a compact TiO_2 film was coated by spray pyrolysis method and annealed at 450°C for 30 minutes. Mesoporous TiO_2 (mp- TiO_2) solution was

prepared by dissolving 1 g TiO$_2$ paste in ethanol at a volume ratio of 1:10 and was coated on the compact TiO$_2$ layer by rotating at 4500 rpm for 20 seconds. For the annealing process, samples were first annealed at 125°C for 30 minutes, then the temperature was gradually increased to 500°C and annealed at this temperature for another 20 minutes. Then, the SnO$_2$ layer was produced by spinning the 0.1 M SnCl$_4$ solution at 3000 rpm for 20 seconds and annealing at 150°C for 10 minutes and then at 190°C for 1 hour. Before coating the perovskite solution, the pre-coated film was treated with UV-ozone for 30 minutes. The perovskite absorbing layer and hole transport layer are deposited within a glove box containing a nitrogen (N$_2$) atmosphere under vacuum conditions. The perovskite precursor solution was prepared by dissolving the lead iodide (PbI$_2$) (1.19 M), formamidinium iodide (FAI) (1.04 M), methylammonium bromide (MABr) (0.15 M), cesium iodide (CsI) (0.10 M) and lead bromide (PbBr$_2$) (0.15 M) in N,N-dimethylformamide:dimethyl sulfoxide (DMF:DMSO) (4:1 volume ratio). The prepared solution was first coated at 1000 rpm for 10 seconds and then at 5000 rpm for 30 seconds, and 100 μL of chlorobenzene was dropped onto the film surface 15 seconds before the end of the coating process. The film was annealed at 100 °C for 1 hour. Then 10 mg of TPMAI, SPMAI and FPMAI salts were dissolved in 1 mL of IPA. The salt solutions were coated by the spin-coating method at 4000 rpm for 30 seconds. Spiro OMeTAD: Co FK209: Li-TFSI: TBP was mixed at molar ratios of 1:0.03:0.5:3.3 and coated by spinning at 4000 rpm for 20 seconds. Finally, a 70 nm thick gold layer was deposited as the counter electrode with the evaporation method.

2.3 Characterization Techniques

There are several techniques that we used during the thesis studies to characterize perovskite solar cells, including:

1. **Current-Voltage (I-V) Measurements:** JV measurements, or current-voltage measurements, are a common way to characterize the performance of perovskite solar cells. In a JV measurement, a solar cell is placed in a

circuit, and the current and voltage are measured as the cell is illuminated with light. The resulting curve, known as the JV curve, can provide important information about the solar cell's performance, including its efficiency and fill factor. The J-V measurements were conducted using a Keithley 2400 source meter and a Pico G2V LED solar simulator with an AM 1.5G illumination intensity and a scan rate of 100 mV/s. The active regions of metal contacts were determined to be 3 mm^2.

2. **External Quantum Efficiency (EQE):** A solar cell's EQE (external quantum efficiency) measures the efficiency with which the cell converts incident photons into electrical current. It is typically measured under standardized test conditions and is expressed as a percentage. These measurements are used to determine the efficiency of the cell at converting light into electricity and can provide information about the performance of different layers within the cell. The EQE was measured using a PV characterization system (Bentham Instruments, PVE300) equipped with a light source and monochromator to calculate integrated J$_{sc}$ values.

3. **X-ray Diffraction (XRD):** This technique is used to determine the crystal structure of the perovskite material, which can provide information about its optoelectronic properties. XRD patterns were obtained (Rigaku Ultima-IV X-Ray diffractometer) with Cu Kα radiation at 30 kV and 40 mA operation conditions and a grazing angle of 0.5 ° at a scan rate of 2 °/min.

4. **Scanning Electron Microscopy (SEM):** This technique is used to study the surface morphology of the cell and its various layers, which can provide insights into the processing conditions used to fabricate the cell. SEM using the model QUANTA 400F Field Emission is used to observe and record the top view of the perovskite films with/without HTMs, as well as the cross-sectional image of the devices.

5. **Contact Angle:** To assess the surface wettability of the produced films, i.e. the hydrophobicity of the HTMs, the contact angles were recorded using the

Attension Theta Lite instrument. In the studies, a drop of water was placed on the film surfaces, and the resulting images were captured instantaneously.

6. **Ultraviolet-visible (UV-Vis) Spectroscopy**: UV-vis spectroscopy is a technique that can be used to study the optical properties of perovskite materials, including their absorption and emission of light. Ultraviolet-visible (UV-Vis) absorption spectra were recorded on a Agilent Technologies 8453 UV-Vis Spectrophotometer.

7. **Photoluminescence (PL):** PL spectra were recorded on a fluorescence spectrophotometer we designed for our research group. There are two Ocean Insight Tungsten Halogen light sources, two Ocean Insight flame visible/near-infrared spectrometers, UV-visible bifurcated fibers, which are high OH fibers that transmit the light (300-1100 nm) efficiently, UV-visible 33 patch cords, and two collimating lenses in the PL setup. The films were excited with an excitation wavelength of 430-435 nm with a UV-LED lamp. The reflection probe detected the radiation of the excited sample.

8. **Conductivity:** Two-probe electrical conductivity measurements were performed to determine the electrical conductivity of HTM films with a device structure of glass/HTMs/Au (Figure 2-3). The conductivity (σ) was then calculated using the following equation (Eqn 1):

$$\sigma = \frac{W}{RLD} \qquad\qquad Eqn.\,1$$
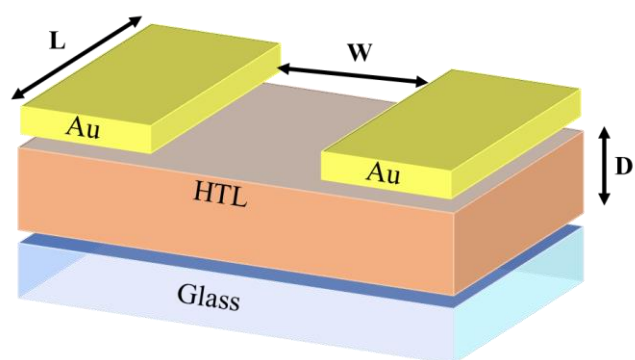
Figure 2-3. Schematic illustration of the fabricated device for conductivity measurements

2.4   Synthesis Procedures

The general procedure in Figure 2-4 was used for all DPP polymer synthesis. Aliekber Karabağ, Figen Varlıoğlu Yaylalı and Mustafa Yaşa synthesized all of the materials used in this thesis.
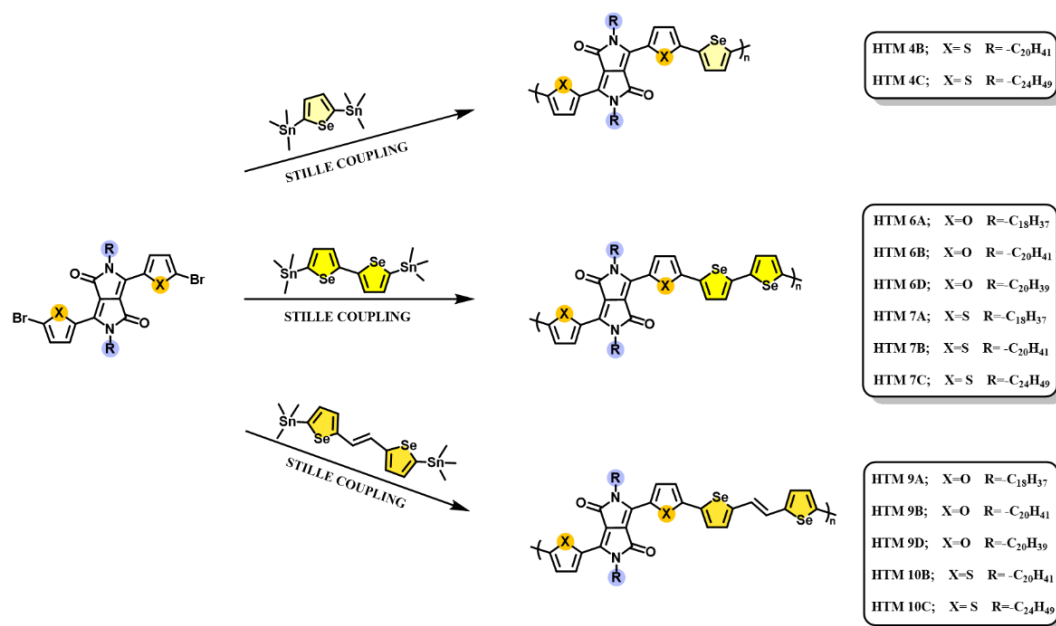
Figure 2-4. Schematics of DPP Polymer synthesis
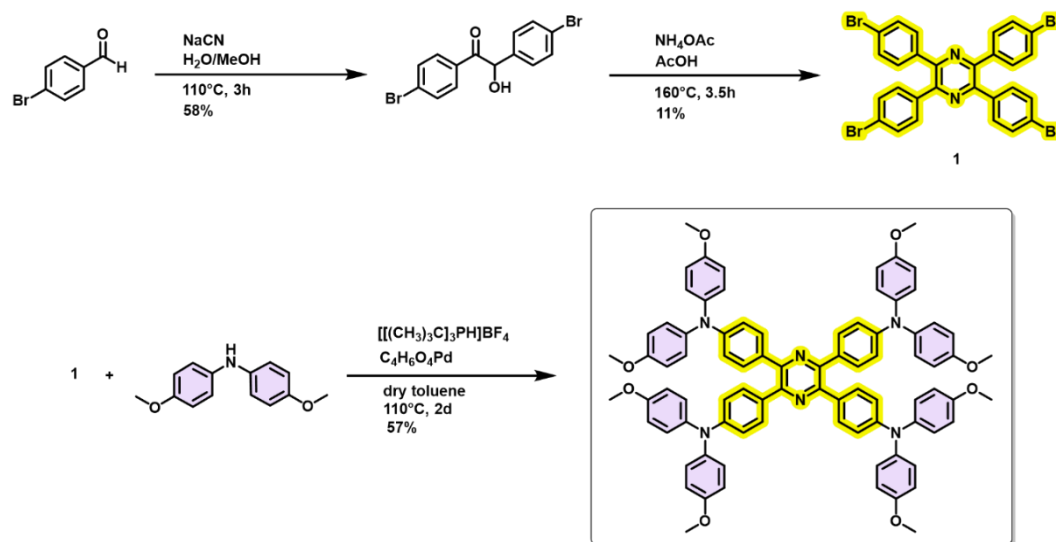
Figure 2-5. Schematics of PT-TPA synthesis
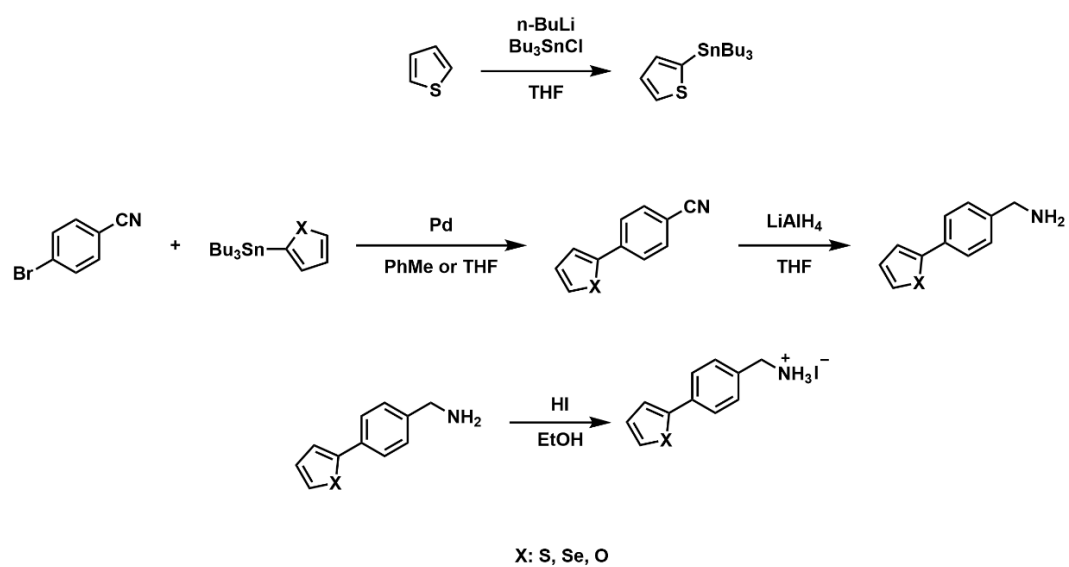
Figure 2-6. Schematics of PMAI salts synthesis

CHAPTER 3

DIKETO PYRROLOPYRROLE (DPP) – BASED POLYMERS
as HTMs in PSCs

One of the primary components of perovskite solar cells is hole transport materials (HTMs). As noted in Chapter 1, in order for HTM to be suitable for PSCs, it must possess the following characteristics: a) a HOMO level suitable for the perovskite material, b) high hole mobility, c) good film-forming capabilities, and d) photochemical stability. In contrast to small molecules and inorganic HTMs, polymer HTMs exhibit excellent stability and solution processability[72–77].

Conductive polymers are one of the most effective HTMs used in PSCs. Contrary to other small molecules, charge transport in polymers occurs via two distinct pathways: intramolecular and intermolecular charge transport. Generally, conducting polymers generate significantly longer conjugated systems, facilitating rapid charge transport. Furthermore, intramolecular charge transport is considerably faster than intermolecular charge transport, highly dependent on the distance between molecules. Consequently, these polymers often provide high charge carrier mobility. Moreover, the relatively flexible conducting polymers may be coated in thinner layers than small molecules, which enables charge transport in HTM.

In relation to organic small molecule and inorganic HTMs, conjugated polymer HTMs exhibit better stability and solution operability. They are typically easier to process than inorganic materials, and they can be deposited using a variety of solution processing techniques, which are generally low-cost and scalable methods. Additionally, polymer-based solar cells became increasingly popular due to their simple synthesis and purification processes, as well as their enhanced processability. Polymer HTLs can also be engineered to have specific properties, such as specific energy levels solubility and conductivity, which can be useful for optimizing the performance of the solar cells.

Researchers investigated polymer-based HTMs as HTLs for PSCs because of their high hole mobility and superior film-forming capabilities.

DPP (diketopyrrolopyrrole) polymers, are a class of conjugated polymers that are characterized by the presence of diketopyrrolopyrrole (DPP) units in their backbone. DPP polymers are known for their good electrical conductivity, which makes them attractive for use in a variety of electronic and optoelectronic applications.

The first report of dopant-free polymeric HTM employed in a perovskite solar cell in 2013 was a DPP-based polymer, PCBTDPP[78]. Cai *et al.* successfully fabricated solid-state hybrid solar cells with p-type polymer PCBTDPP as the hole carrying material. This polymer comprises carbazole, thiophene, and 2,5-dihydropyrrolo[3,4]pyrrole-1,4-dione (DPP) units with alkyl chains that enhance its solution processability. Although efficiencies were not on par with the leading materials at the time, the study was substantial from the perspective of demonstrating the ability of polymeric HTMs to work in PSC cells which has been and greatly improved over the years.

Diketopyrrolopyrrole (DPP)-based polymers have drawn a great deal of attention for photovoltaics during past years due to their excellent optoelectronic properties, such as high hole mobility, good thermal and photostability, high hydrophobicity.

Strong - interactions, a relatively high electron affinity, and strength of the optoelectronic characteristics are all critical qualities of the DPP core unit, and they have been the primary drivers in their utilization in solar cell applications. In addition to being a strong electron-withdrawing group thus enabling realization of donor-acceptor type polymer for energy level allignment, the diketopyrrole group strengthens the crystallization tendency in diketopyrrole-based polymers due to its polar structure. Diketopyrrole-based (DPP) polymers are also gained attention due to their simple synthesis mechanism and absorption in the near-infrared region. With all these properties, DPP polymers are great candidates as transport layers in perovskite solar cells.

DPP Polymers have four main components (Figure 3-1), which are; i) the DPP unit, ii) alkyl chains, iii) aromatic substituent and lastly, iii) π-conjugated segment. DPP polymers' optical and electronic properties can be adjusted by changing aromatic substituents or π-conjugated segments. The alkyl chains on the DPP unit help to improve the solubility of polymer for solution processing and are essential in terms of the crystallization of the polymer during thin film deposition.
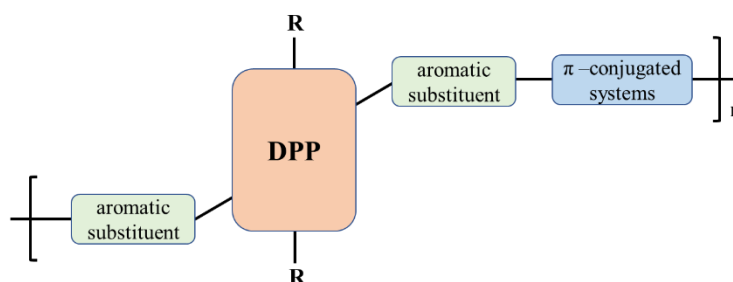
Figure 3-1. The basic structure of DPP polymers includes the four principal parts: the DPP unit, the alkyl chains, the aromatic substituent, and the π-conjugated segment.

The amide groups of an unsubstituted DPP unit form intermolecular hydrogen bonds, which results in very poor solubility in organic solvents. To impart solubility on the DPP polymers and facilitate the fabrication of solar cells by solution processing, it is mandatory to introduce (alkyl) side chains on these positions. In practice, linear side chains are often not enough to solubilize DPP polymers, but alkyl chains, with branching on the 2-position, have proven to be an effective way of providing sufficient solubility.

The aromatic substituents are introduced during the formation of the DPP unit and strongly influence the optical and electrical properties. The optical band gap can be more finely tuned by variation of the electron donating properties of the π-conjugated segment. By introduction of stronger electron donating π-conjugated segments, the optical band gap can be reduced. Photovoltaic parameters of DPP-based polymer as HTMs in perovskite solar cells in the literature are presented in Table 3-1.

Table 3-1. Photovoltaic parameters of DPP-based polymer HTMs in the literature

Device Configuration	Polymer Name	Polymer Structure	Voc (V)	Jsc (mA/cm^2)	FF (%)	PCE (%)	Ref
FTO/TiO$_2$/MAPbI$_3$/HTM/Ag	PDPP3T		0.98	20.5	61	12.3	[79]
FTO/TiO$_2$/MAPbI$_3$/HTM/Au	PDVT-10		0.99	20.9	65	13.4	[80]
FTO/TiO$_2$/CsMAFAPb(BrI)$_3$/HTM/Au	DPP-P4		1.01	19.7	72	14.2	[81]
FTO/SnO$_2$/Cs$_{0.05}$(MA$_{0.17}$FA$_{0.83}$)$_{0.95}$Pb(I$_{0.83}$Br$_{0.17}$)$_3$/HTM/Au	PBDTP-DTDPP		1.08	19.4	69	14.7	[82]
FTO/TiO$_2$/CsPbI$_2$Br/HTM/Au	DPP-DTT		1.29	15.0	78	15.1	[83]
FTO/TiO2/PCBM/MA$_{1-y}$FA$_y$PbI$_{3-x}$Cl$_x$/HTM/Ag	PDPPT-TT		1.04	22.6	69	16.2	[84]
FTO/TiO$_2$/RbCsMAFAPb(BrI)$_3$/HTM/Au	DPP-P4		1.05	20.6	75	16.3	[81]
FTO/TiO2/PCBM/MA$_{1-y}$FA$_y$PbI$_{3-x}$Cl$_x$/HTM/Ag	PDPPT-TT (solv. vap. anneal.)		1.07	22.8	72	17.8	[84]
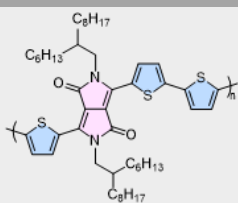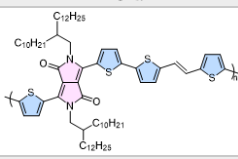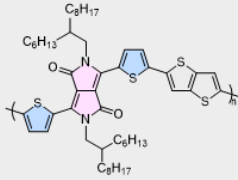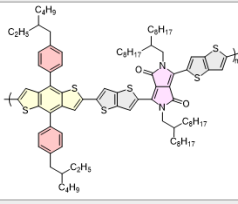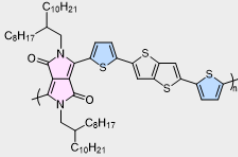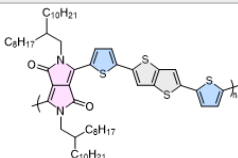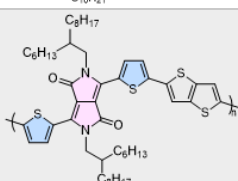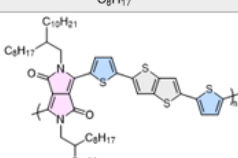
ITO/SnO₂/(MA₀.₈FA₀.₂)Pb(I₀.₉₃Cl₀.₀₇)₃/HTM/Ag	P25NH		0.99	22.2	82	18.1	[85]
ITO/SnO₂/(MA₀.₈FA₀.₂)Pb(I₀.₉₃Cl₀.₀₇)₃/HTM/Ag	P5NH		1.04	21.0	83	18.1	[86]
ITO/C60-SAM/SnO₂/PC₆₀BM/FAMA/HTM/ Ta-WOₓ/Au	pDPP5T-2		1.15	21.5	76	18.9	[87]
ITO/SnO₂/FA₀.₈₅MA₀.₁₅PbI₃/HTM/MoO₃/Ag	2DP-TDB		1.16	24.1	76.9	21.5	[88]
ITO/SnO₂/FA₀.₈₅MA₀.₁₅PbI₃/HTM/MoO₃/Ag	2DP-O		1.18	24.9	81.6	24.1	[89]
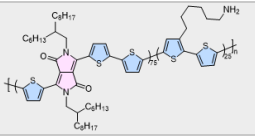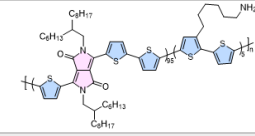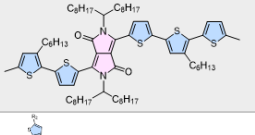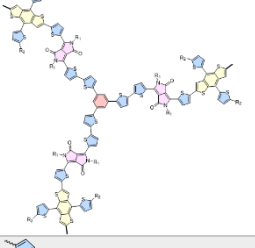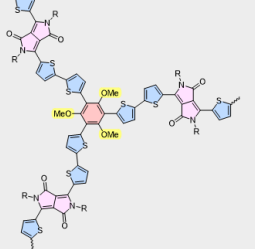
Thiophene-substituted DPP polymers are used for photovoltaic applications of their appropriate optoelectronic properties. Absorption of DPP polymers can be shifted to the near-infrared region with the thiophene substitution. Also, they exhibit high hole mobility above 1 cm² V⁻¹ s⁻¹.

Recent studies indicate that the polymer containing sulphur and selenium can be applied as the hole transport layer in perovskite solar cells. Its photoluminescence and light-induced absorption properties make it a better material for charge transport. According to the thiophene group, the selenophene group in DPP polymers indicates a correspondingly lower band gap. Sulfur substitution with selenium reduces interring bond lengths with a greater contribution from quinoidal resonance structures in the ground state, making polyselenophene backbones rigid and difficult to twist[90,91]. The improved photostability of selenophene-substituted polymer films

was attributed to the deeper LUMO and p-type behaviour. Furthermore, the incorporation of selenophene into the polymer backbone decreased solubility but increased the crystallinity of films, typically resulting in improved charge transport in devices due to strong intermolecular selenophene-selenophene – interactions[92]. With the combination of the low band gap, good film morphology, and great stability, selenophene-incorporated DPP polymers are a promising donor material candidate for photovoltaic applications.

3.1   Results and Discussions

Here we demonstrate our results for utilization of various DPP-based polymer as hole transport materials into the perovskite solar cells to realize a structure-activity realationship. Polymers were used as hole transport layer instead of Spiro-OMeTAD in normal (n-i-p) structured perovskite solar cells. The efficiencies of cells in which the synthesized polymers are used as HTL are fairly similar to the DPP-based polymers in the literature, and a great improvement in cell stability has been demonstrated.

In this context, a group of DPP-based polymers were synthesized and named as HTM 4B, HTM 4C, HTM 6A, HTM 6B, HTM 6D, HTM 7A, HTM 7B, HTM 7C, HTM 9A, HTM 9B, HTM 9D, HTM 10B, and HTM 10C. The structures and naming of DPP-based polymers with different aromatic substituents (furan, thiophene, and selenophene), different π-conjugated units and different alkyl groups are listed in the
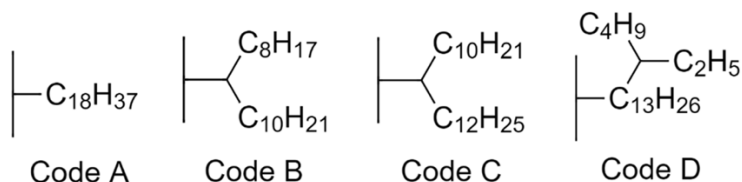
Figure 3-2 in an orderly fashion.

44
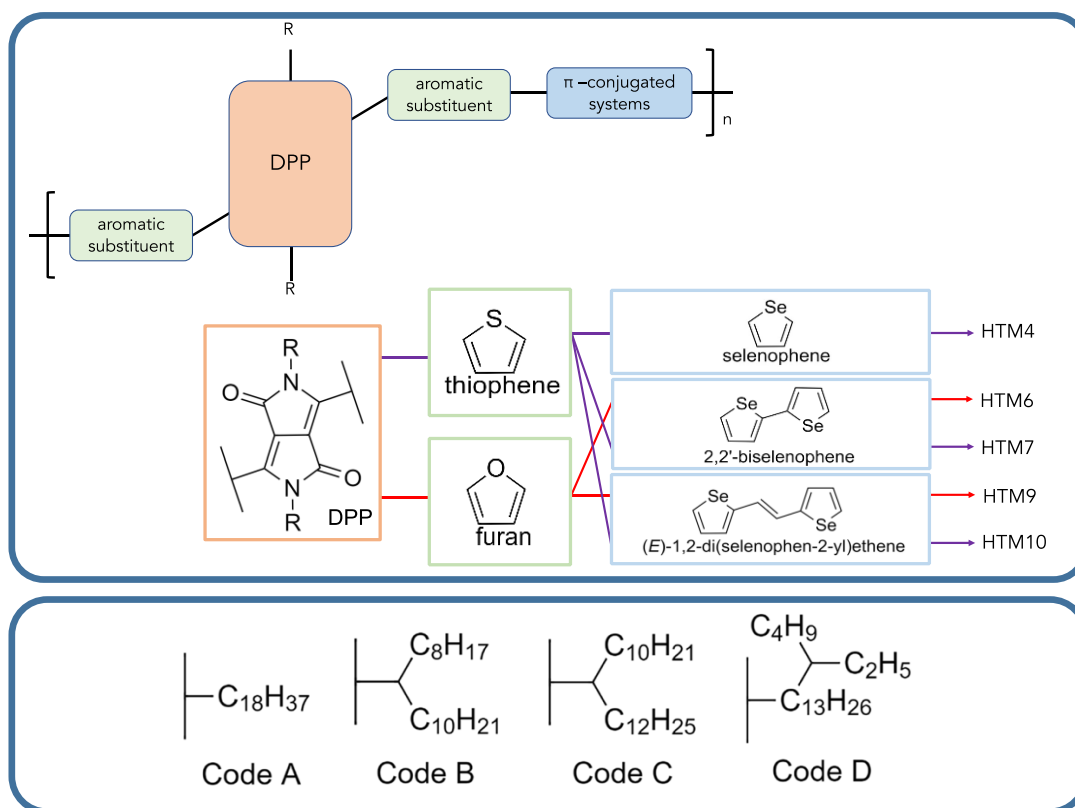
Figure 3-2. Polymer nomenclature scheme

HTMX layout was created based on the aromatic substituent (furan or thiophene) on DPP unit and the donor unit (selenophene, 2-2'-biselenophene, (E)-1,2-di(selenophene-2-il)ethane and thieno(3,4-b)thiophene). According to the alkyl chain differences, it is divided into addition four groups labelled by letters a, b, c, and d.

Table 3-2 demonstrates the chemical structures, molecular weights, and band gap values of all synthesized polymers and photovoltaic studies. GPC results could not be obtained due to the solubility problems of HTM 6D, HTM 9A, HTM 9B, HTM 9D, and HTM 10B polymers.

The optical absorption of the DPP-based polymer hole transport materials as thin films was measured by ultraviolet-visible (UV–vis) spectroscopy. The optical band gap values of the polymers were obtained from the UV absorbance spectrum, and

are given in Table 3-2. Figure 3-3 displays images of polymer films coated on glass. Polymers with solubility problems can be easily identified from film quality.

Table 3-2. Chemical structures, molecular weights and band gaps of synthesized DPP-based polymers

HTM	Chemical Structure	GPC Result	E_g (eV)
4B		Mw: 41.4 kDa Mn: 16.0 kDa PDI: 2.59	1.28
4C		Mw: 48.5 kDa Mn: 30.1 kDa PDI: 1.61	1.23
"6A		Mw: 5.2 kDa Mn: 4.0 kDa PDI: 1.3	1.36
6B		Mw: 28.5 kDa Mn: 8.60 kDa PDI: 3.3	1.40
6D		-	1.47
7A		Mw: 8.05 kDa Mn: 6.03 kDa PDI: 1.33	1.45
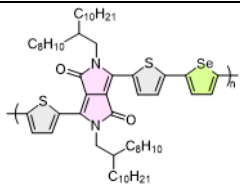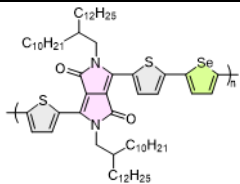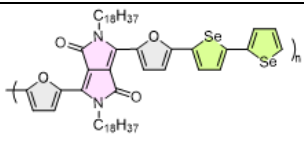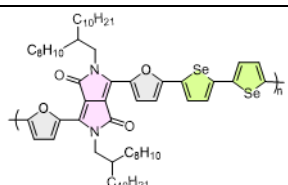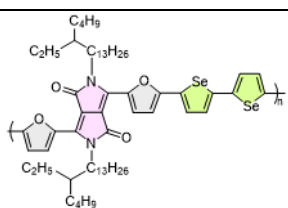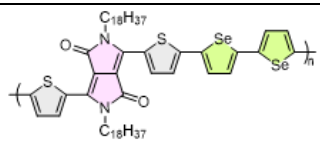
7B		Mw: 36.2 kDa Mn: 23.0 kDa PDI: 1.57	1.39
7C		Mw: 362 kDa Mn: 156 kDa PDI: 2.32	1.40
9A		-	1.42
9B		-	1.41
9D		-	1.37
10B		-	1.37
10C		Mw: 316 kDa Mn: 151 kDa PDI: 2.09	
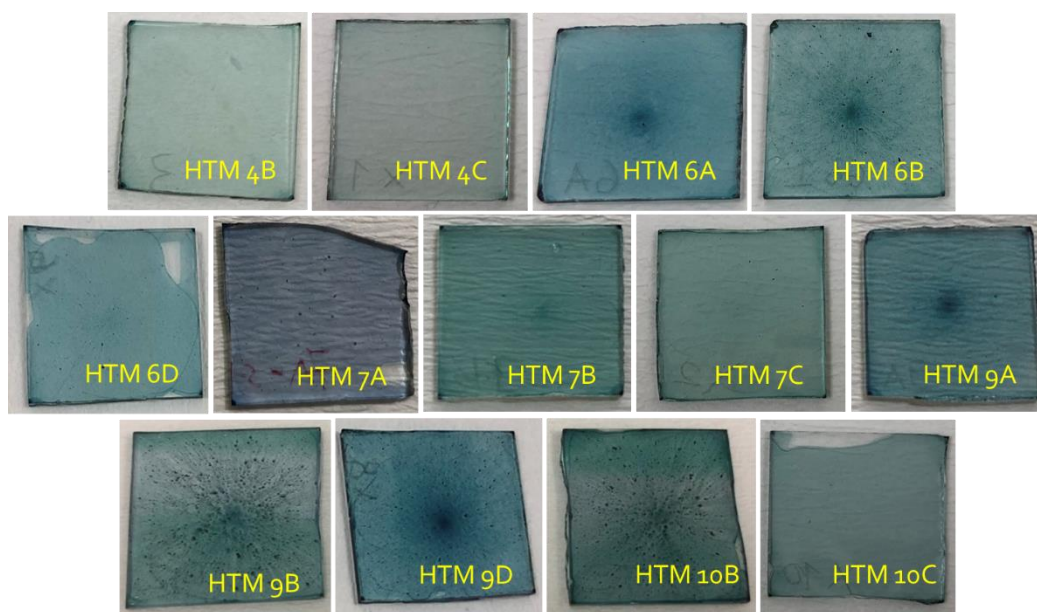
Figure 3-3 Thin film state of DPP-based polymers on glass

3.1.1 Optimization Studies of HTM 4B

Hole transport layer optimization of DPP-based polymers studies were performed with HTM 4B polymer and promising results were achieved. HTM 4B polymer dissolves well in chlorobenzene and was coated on perovskite by spin coating method. It was observed that the film was homogeneously coated on the surface (Figure 3-4).
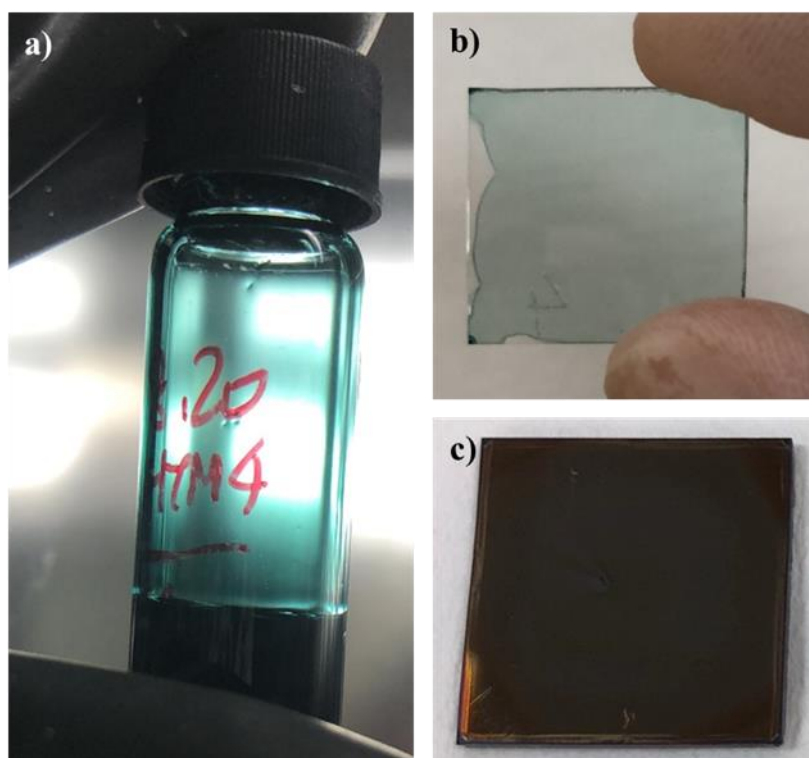
Figure 3-4. At 10 mg/mL concentration a) HTM 4B solution, b) HTM 4B thin film coated on glass, c) HTM 4B layer coated on perovskite

Compared to reference HTM Spiro-OMeTAD, DPP-based polymer HTMs are more cost-effective materials. While Spiro-OMeTAD is coated with a concentration of 72.3 mg/mL, DPP-based polymers perform remarkably well with a concentration of only 10 mg/mL or less without using dopants. As seen in Figure 3-5, almost similar efficiency values were achieved with the polymer film coated with a thickness of almost one-third of the reference cell. The thin and homogeneous film produced by HTM 4B draws attention.
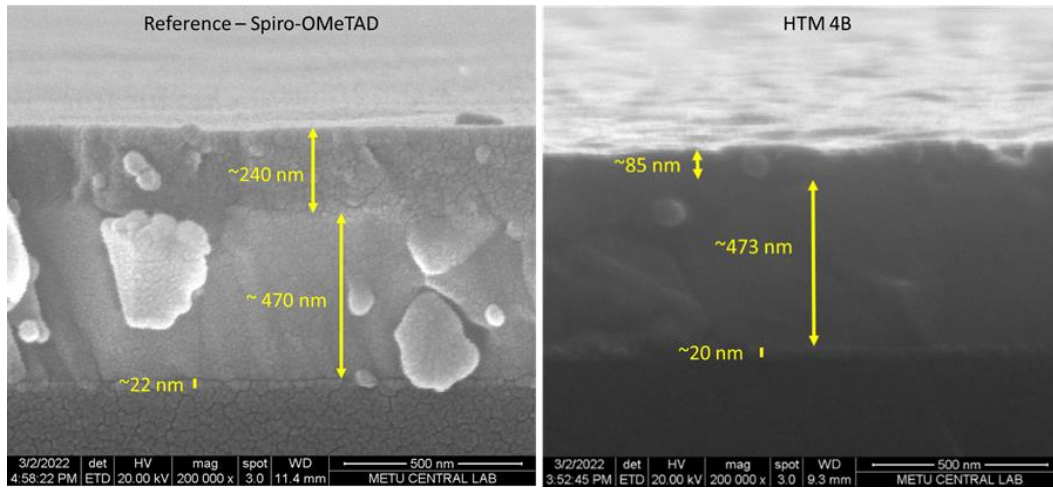
Figure 3-5. Cross-section SEM images of reference and HTM 4B perovskite solar cells with a device structure of ITO/SnO$_2$/Perovskite/HTL

3.1.1.1 Concentration Optimization

Firstly, 5 mg, 10 mg, 15 mg, and 20 mg of polymers were dissolved in 1 mL of chlorobenzene, and cell performances were measured (Table 3-3). The highest efficiency was obtained as 13.57 % at 10 mg/mL concentration. The short circuit current density (J_{sc}) value of the cell was measured as 18.60 mA/cm^2, the open circuit voltage (V_{oc}) was 1.02 V, and the fill factor (FF%) value was 71.50. Looking at the mean values, the values of 10.61%, 12.86%, 12.52%, and 12.34% were measured for 5 mg/mL, 10 mg/mL, 15 mg/mL and 20 mg/mL, respectively. As a result of the average values, 10 mg/mL concentration was chosen as the best one.

Table 3-3. Photovoltaic parameters of cells including HTM 4B hole transport layer
prepared at different concentrations

HTM		V_{oc} (V)	J_{sc} (mA/cm^2)	FF (%)	PCE (%)
5 mg/mL	Average	0.91 ± 0.03	18.69 ± 0.42	62.67 ± 6.20	10.61 ± 0.91
	Highest	0.97	18.31	67.53	11.99
10 mg/mL	Average	0.99 ± 0.04	18.21 ± 0.51	71.01 ± 1.48	12.86 ± 0.79
	Highest	1.02	18.60	71.5	13.57
15 mg/mL	Average	1.00 ± 0.02	17.47 ± 0.63	71.33 ± 1.92	12.52 ± 0.83
	Highest	1.02	18.25	72.72	13.53
20 mg/mL	Average	1.01 ± 0.03	17.30 ± 0.45	70.81 ± 2.35	12.34 ± 0.61
	Highest	1.00	17.94	74.23	13.32

The JV plot of the cells produced at different concentrations with the best efficiencies
is shown in Figure 3-6.
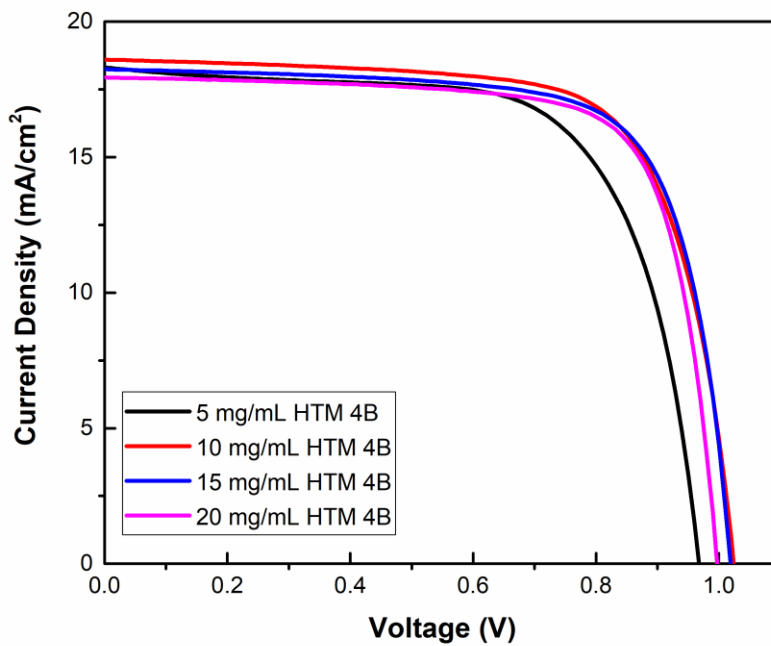
Figure 3-6. JV plot of best cells including HTM 4B hole transport layer prepared at different concentrations

Box charts of all cells are given in Figure 3-7. As seen from the box charts graphs, although the best average J_{sc} value was obtained with 5 mg/mL, V_{oc} and FF values were measured relatively low according to the other concentration devices. Although the films coated with 5 mg/mL solution are suitable in terms of thickness, their V_{oc} and FF values are low due to lack of uniform surface coating. For this reason, studies were continued with 10 mg/mL HTM 4B concentration, considering the average and highest results.
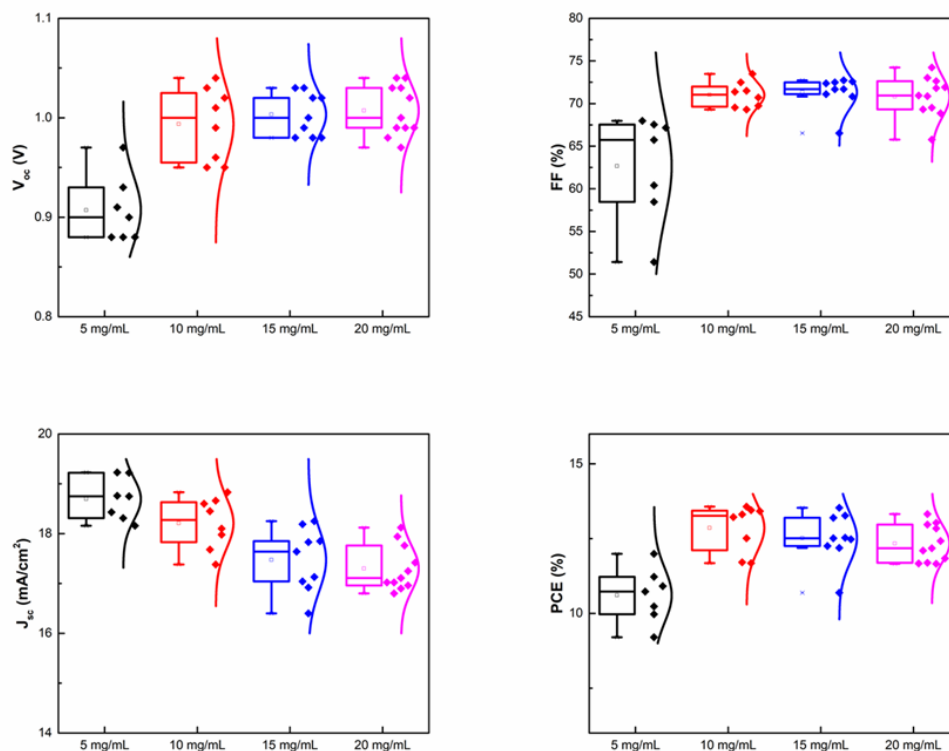
Figure 3-7. Box charts of HTM 4B hole transport layer prepared at different concentrations (Voc, Jsc, FF% and PCE%)

3.1.1.2 Spin-speed Optimization

The subsequent study aimed to decide the correct spin speed, and HTM 4B polymer film was coated at different spin speeds between 1000 rpm and 4000 rpm. The concentration of all solutions for film fabrication was fixed 10 mg/mL based on previous set results. Homogeneous film quality was observed at all rotation speeds, and efficiency values close to each other were observed. The doped Spiro-OMeTAD material was used as the hole transport layer in the reference cell.

While the perovskite cell coated with 2000 rpm worked on average at 14.22%, the highest efficiency for that spin speed was seen at 15.76%. The short circuit current density (J_{sc}) value of the cell was measured as 20.34 mA/cm^2, the open circuit voltage (V_{oc}) was 1.02 V, and the fill factor (FF%) value was 75.96. Efficiency values

obtained with the undoped HTM 4B polymer were comparable to the reference cell
(Table 3-4).

Table 3-4. Photovoltaic parameters of cells containing HTM 4B hole transport
layer prepared at different spin speeds

HTM		V_{oc} (V)	J_{sc} (mA/cm^2)	FF (%)	PCE (%)
Reference	Average	1.13 ± 0.01	20.10 ± 0.66	78.19 ± 1.63	17.70 ± 0.71
	Highest	1.13	21.18	79.67	19.07
1000 rpm	Average	0.98 ± 0.01	19.87 ± 0.79	72.76 ± 1.74	14.18 ± 0.67
	Highest	0.99	20.33	75.29	15.15
2000 rpm	Average	0.99 ± 0.01	19.96 ± 0.74	71.68 ± 3.49	14.22 ± 0.93
	Highest	1.02	20.34	75.96	15.76
3000 rpm	Average	0.98 ± 0.01	20.09 ± 0.85	71.64 ± 3.18	14.05 ± 0.67
	Highest	0.98	21.05	72.52	14.96
4000 rpm	Average	1.00 ± 0.02	19.97 ± 0.71	72.95 ± 1.53	14.51 ± 0.74
	Highest	1.01	20.84	74.5	15.68

The JV graph of the cells with the best efficiency, produced at different rotation
speeds, is shown in Figure 3-8.
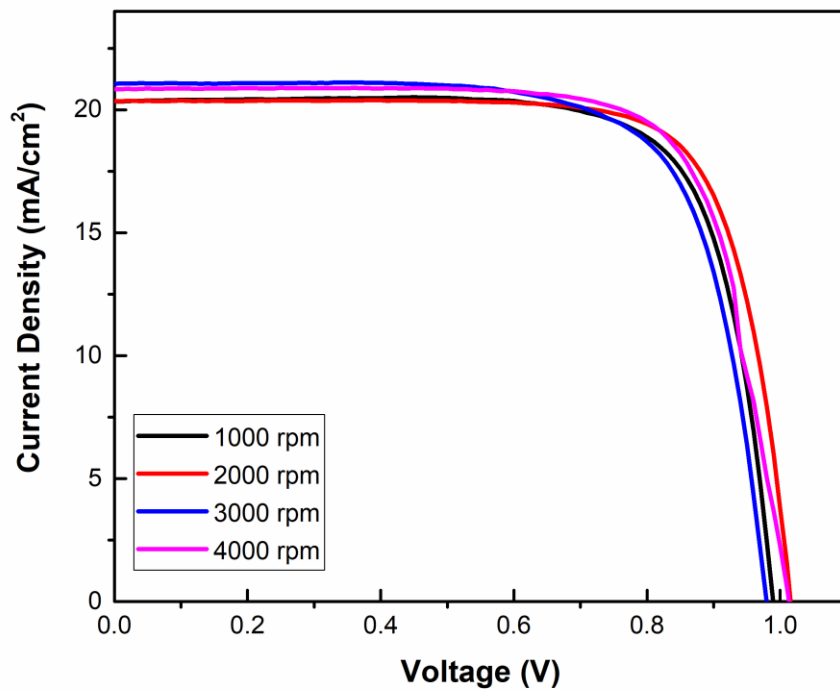
Figure 3-8. JV plot of perovskite solar cells prepared with HTM 4B hole transport material coated at different spin speeds

Box charts of all cells measured are given in Figure 3-9. As demonstrated in the box charts, successful and comparable results were obtained on average at all spin speeds; nonetheless, the study continued with the optimal speed of 2000 rpm.
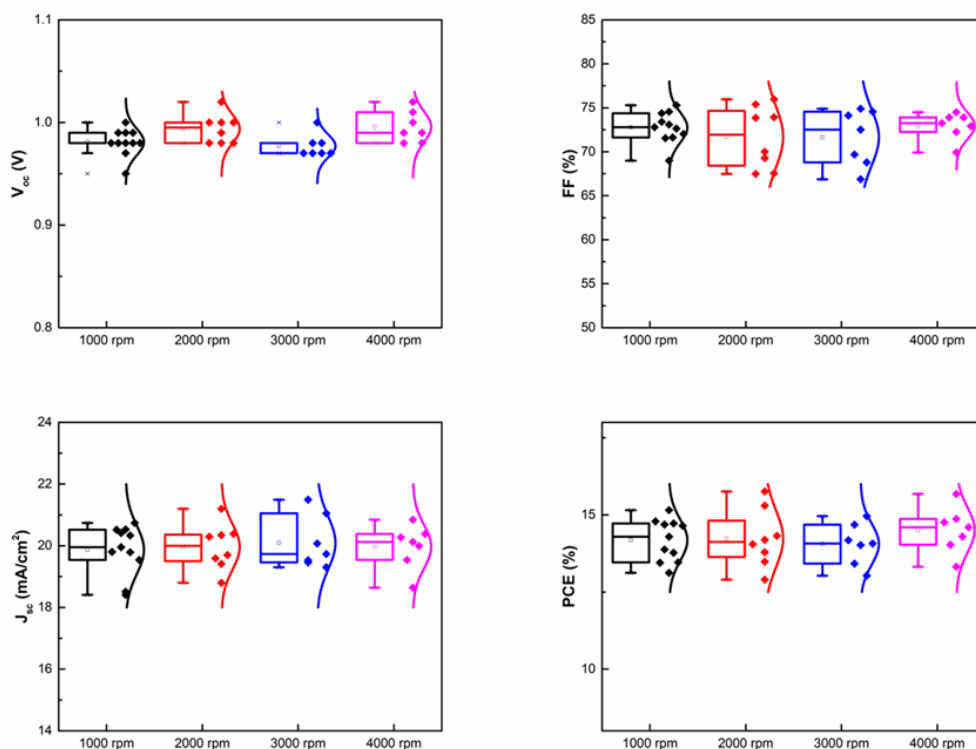
Figure 3-9. Box charts of cells containing HTM 4B hole transport material
fabricated at different spin speeds (Voc, Jsc, FF% and PCE%)

3.1.1.3 Addition of electron blocking layer

HTM 4B devices exhibited lower FF values than reference cells, which resulted in
lower final efficiency values compared to the reference. HTM 10C is one of the DPP-
based polymers with a very similar chemical structure to HTM 4B that was
synthesized in our labs. The integrated J_{sc} values of solar cells were calculated to be
20.31 mA/cm^2 and 17.60 mA/cm^2 for reference and HTM 10C, respectively. The
external quantum efficiency (EQE) graph of HTM 10C was analyzed in order to
determine the cause of this observation.

Cells containing Spiro-OMeTAD and HTM 10C as hole transport layers were compared in the external quantum efficiency (EQE) graph in Figure 3-10. When the external quantum efficiency (EQE) graph of HTM 10C is examined, it is seen that there is a current loss on the side of the hole transport layer. We believe this loss is observed due to the low band gap of these polymers which in turn results in low lying LUMO levels thus ineffective electron blocking. Since a similar effect is predicted for HTM 4B, MoO_3, a well-known electron blocking layer, was coated between the hole transport layer and the metal electrode to prevent this current loss. The MoO_3 layer was coated with a thickness of 10 nm by thermal evaporation.
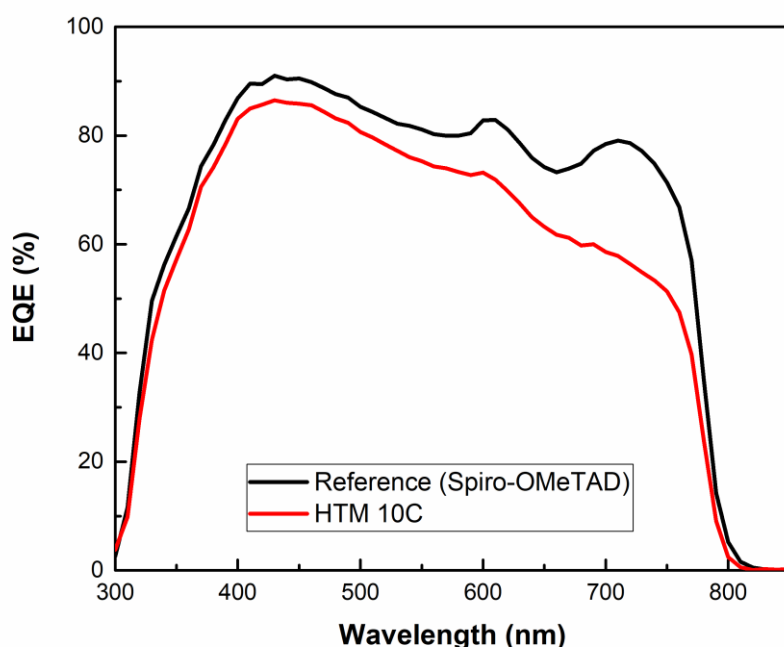
Figure 3-10. External quantum efficiency (EQE) graph of the reference and HTM 10C cells

The highest efficiency in the reference cell is measured as 15.16%, with a J_{sc} of 19.64 mA/cm^2, V_{oc} of 1.09 V, and FF of 70.81%. In cells coated with the MoO_3 layer on HTM 4B polymer, the highest efficiency is 11.47%, with a J_{sc} of 20.49 mA/cm^2, V_{oc}

of 1.02 V and FF of 54.87%. The average and highest efficiency values of cells are given in Table 3-5.

Table 3-5. Photovoltaic parameters of cells containing HTM 4B and HTM 4B+MoO$_3$ layer

HTM		V_{oc} (V)	J_{sc} (mA/cm^2)	FF (%)	PCE (%)
Reference -HTM 4B	Average	1.08 ± 0.01	18.64 ± 0.73	69.74 ± 1.06	13.98 ± 0.68
	Highest	1.09	19.64	70.81	15.16
HTM 4B + MoO$_3$	Average	1.00 ± 0.01	20.06 ± 0.51	52.67 ± 3.15	10.59 ± 0.61
	Highest	1.02	20.49	54.87	11.47

While introducing the MoO$_3$ layer, we expected that it will lead to an increase in the FF values by blocking electrons. Nevertheless, contrary to our predictions, even though the average short-circuit current increased in the cells with the MoO$_3$ layer, the open-circuit voltage and fill factor values decreased dramatically. The JV plot of the cells with the highest efficiency and the box charts of the HTM 4B reference and HTM 4B+MoO$_3$ cells are below, Figure 3-11 and Figure 3-12, respectively. For this reason, development studies with MoO$_3$ were not pursued further.
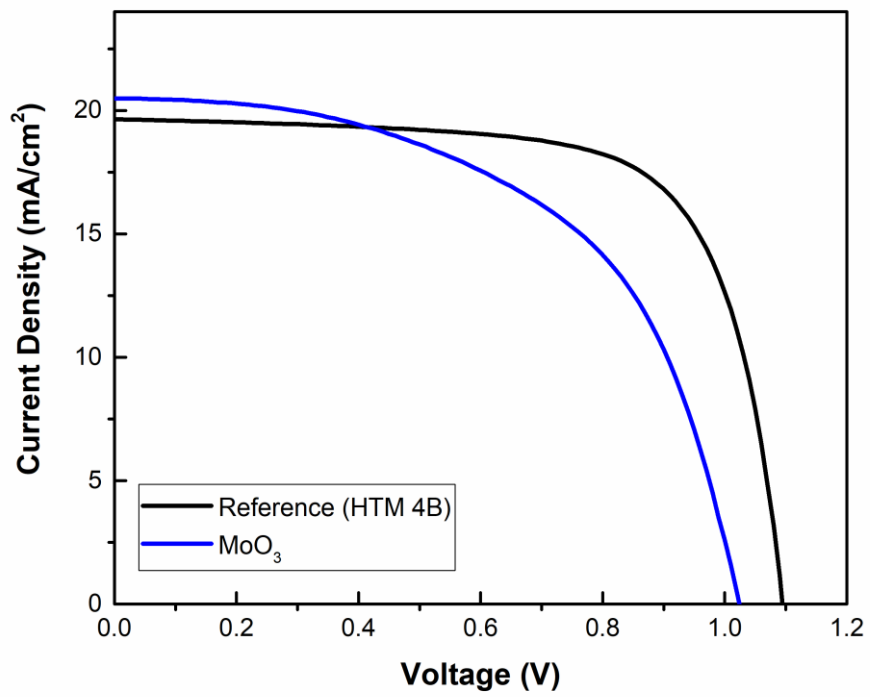
Figure 3-11. JV plot of perovskite solar cells with HTM 4B reference and HTM 4B + MoO$_3$ layer
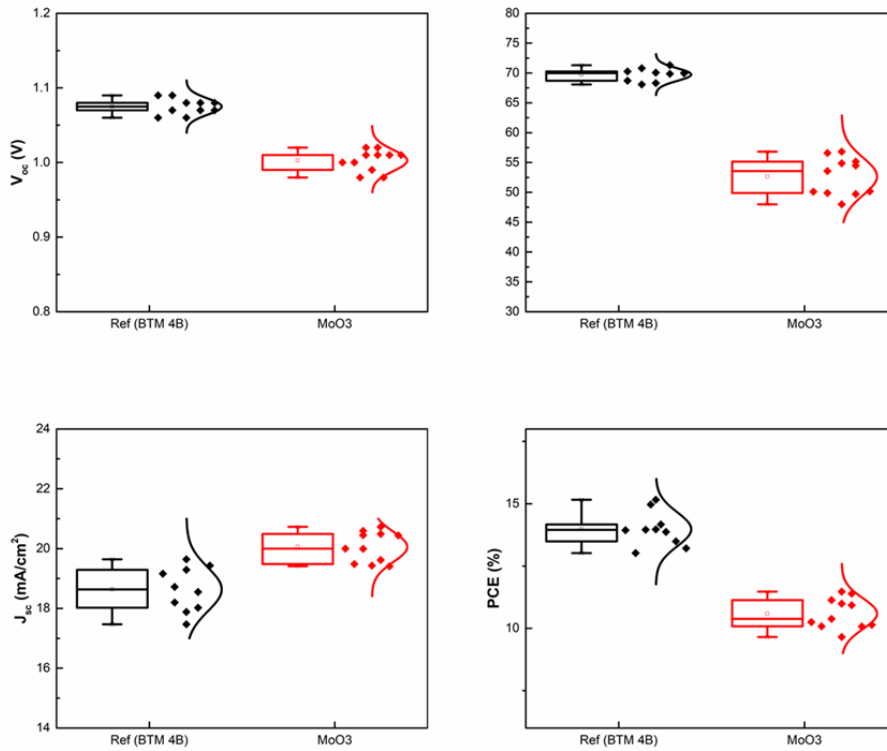
Figure 3-12. Box charts of HTM 4B reference cells and HTM 4B + MoO$_3$ layer cells (Voc, Jsc, FF% and PCE%)

A thin CuI layer, another known electron blocking layer, has been applied to the HTM 4B polymer layer as a second approach to prevent the current loss seen on the EQE graph[93,94]. CuI solution was prepared by dissolving 2.5 mg, 5.0 mg and 7.5 mg CuI in 1 mL acetonitrile solvent and coated between the hole transport layer and the metal electrode by the spin coating method with a rotation speed of 3000 rpm.

Table 3-6. Photovoltaic parameters of reference cell and cells containing different concentrations of CuI

HTM		V_{oc} (V)	J_{sc} (mA/cm^2)	FF (%)	PCE (%)
Reference (Spiro)	Average	1.13 ± 0.01	21.64 ± 0.70	76.28 ± 1.37	18.65 ± 0.60
	Highest	1.13	21.61	78.81	19.25
Reference – (HTM 4B)	Average	1.03 ± 0.02	19.47 ± 0.68	66.83 ± 2.37	13.35 ± 0.87
	Highest	1.04	20.64	67.77	14.55
HTM 4B + 2.5 mg/mL CuI	Average	1.03 ± 0.02	19.66 ± 0.85	67.06 ± 2.34	13.53 ± 1.06
	Highest	1.03	20.76	69.34	14.83
HTM 4B + 5.0 mg/mL CuI	Average	1.00 ± 0.01	19.48 ± 0.74	64.96 ± 2.28	12.60 ± 0.62
	Highest	1.00	20.05	67.42	13.52
HTM 4B + 7.5 mg/mL CuI	Average	1.01 ± 0.02	19.72 ± 0.52	67.46 ± 2.64	13.45 ± 0.82
	Highest	1.01	19.73	70.53	14.05

As seen in Table 3-6, the highest efficiency in the reference cell containing HTM 4B is 14.55% with J_{sc} of 20.64 mA/cm^2, V_{oc} of 1.04 V, and FF of 67.77%. In cells coated with CuI layer on HTM 4B polymer, the highest efficiency was obtained as 14.83% for 2.5 mg/mL CuI, 13.52% for 5.0 mg/mL CuI, and 14.05% for 7.5 mg/mL CuI, respectively. The average efficiency values of the cells are also given in the table above. Adding the CuI layer did not show the expected increase in terms of photovoltaic parameters of the cells. JV plot of the highest efficiency cells and box charts containing all cells produced are given in Figure 3-13 and Figure 3-14, respectively.
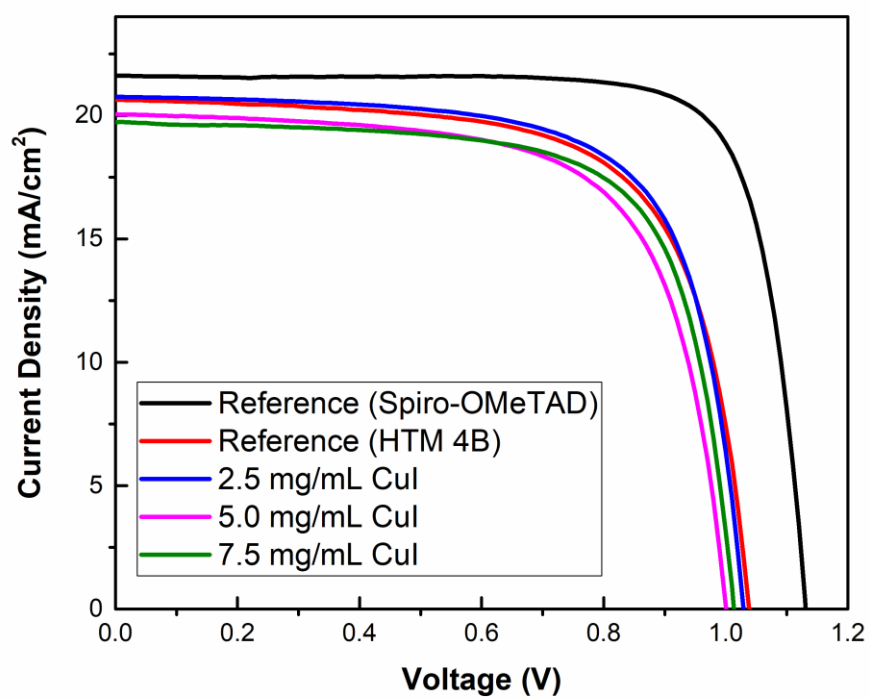
Figure 3-13. JV plot of reference cell and perovskite solar cells containing different concentrations of CuI
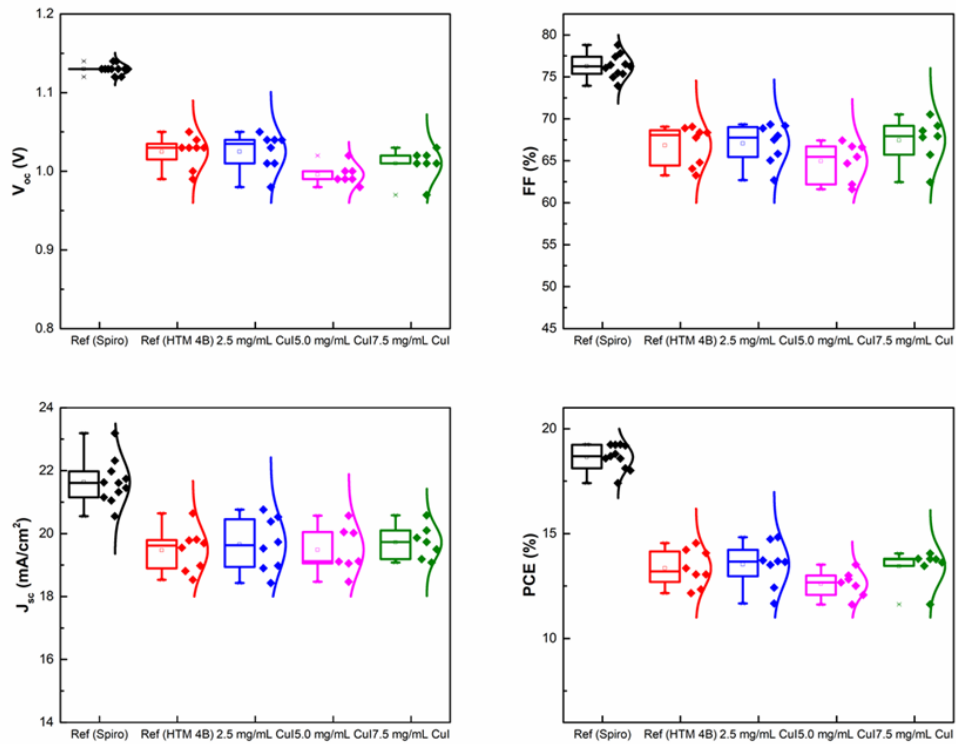
Figure 3-14. Box charts of the reference cell and perovskite solar cells containing different concentrations of CuI (Voc, Jsc, FF% ve PCE%)

3.1.1.4 Reproducibility and Hysteresis

Reproducibility is one of the essential features of perovskite solar cells. A histogram, which displays the statistical results of the fabricated cells[95], shows the PCE distribution for the reference and HTM 4B perovskite solar cells, which is given in Figure 3-15. Notably, the statistical results were derived from over 20 perovskite solar cell devices from multiple batches, indicating that our studies are repeatable. An average PCE of 14.27% was achieved over 20 devices with HTM 4B, and 65% of the fabricated devices have a PCE of >14%.
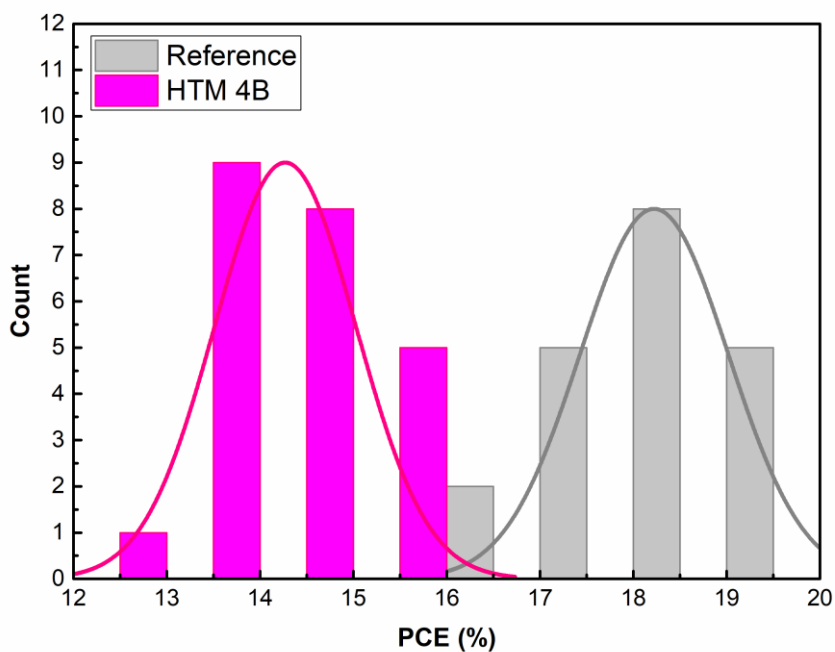
Figure 3-15. Histogram of reference and HTM 4B perovskite solar cells, over 20 devices.

Spiro-OMeTAD based reference cells and cells containing optimized and highest value HTM 4B polymer are given in Table 3-7. The highest efficiency was measured as 15.76% in the cells with the HTM 4B hole transport layer. J_{sc} is 20.34 mA/cm^2, V_{oc} is 1.02 V and FF is 75.96% for that cell.

Table 3-7. Reverse and forward scans of best devices of reference and HTM 4B cells

HTM		V_{oc} (V)	J_{sc} (mA/cm^2)	FF (%)	PCE (%)
Reference –	Reverse	1.13	21.18	79.67	19.07
(Spiro)	Forward	1.1	21.23	67.3	15.72
HTM 4B	Reverse	1.02	20.34	75.96	15.76
	Forward	0.98	20.26	68.95	13.69

HTM 4B polymer layer has a very good film quality and is compatible with the perovskite material. Compared with the doped Spiro-OMeTAD layer, the result obtained with the undoped HTM 4B polymer is quite promising according to the literature. The JV plot of the best cells with reverse and forward measurements cells fabricated is shown in Figure 3-16.
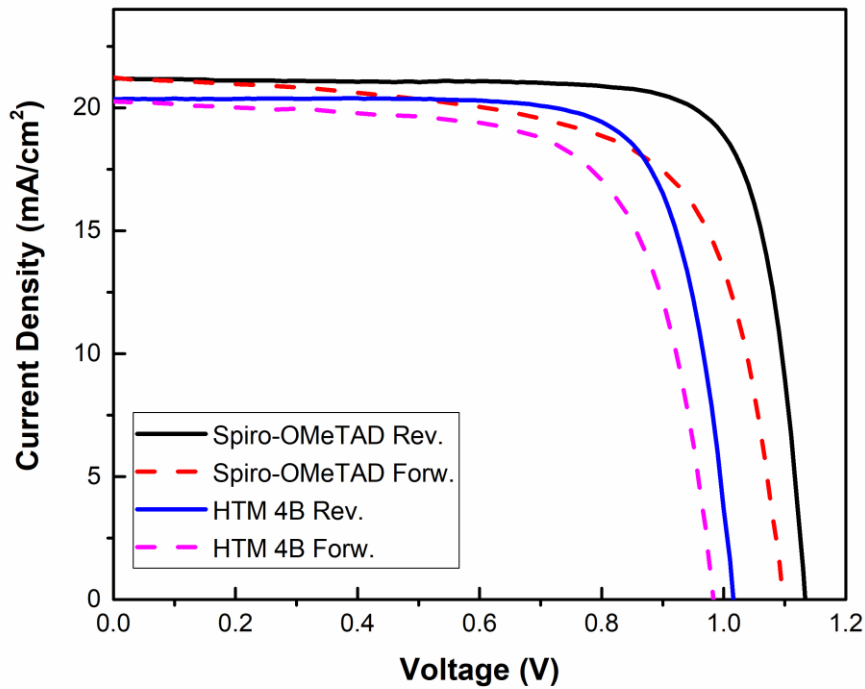
Figure 3-16. Reverse and forward scans of best devices of reference and HTM 4B cells

When evaluated in terms of hysteresis, the HTM 4B polymer shows good performance. The hysteresis values of the cells were calculated with the formula given as Equation 1. The hysteresis value for cells containing Spiro-OMeTAD was 17.57, while the hysteresis value for cells containing HTM 4B was calculated as 13.31. Addition of HTM 4B as a hole transport layer to the device structure instead of Spiro-OMeTAD decreased the hysteresis regarding to forward and reverse voltage scans significantly. As a result, the use of HTM 4B polymer as a hole transport layer gives a better result to solve the hysteresis problem experienced in normal structured perovskite solar cells.

$$Hysteresis\ Index = HI\ Index = \frac{PCE_{reverse} - PCE_{forward}}{PCE_{reverse}} \times 100\% \quad (Eqn\ 1)$$

3.1.2 Device performances of all synthesized DPP-based polymers

Other DPP-based polymers synthesized in our group were utilized as a hole transport layer were prepared with an optimized device structure of HTM 4B. Cell efficiencies were measure and results are detailed in Table 3-8. HTM 7C, HTM 10B, and HTM 10C polymers were prepared at a concentration of 7.5 mg/mL instead of 10 mg/mL (optimized concentration for HTM 4B) due to the high viscosities of the solutions at higher concentration.

Table 3-8. Device and photovoltaic parameters of all synthesized DPP-based polymers

HTM		Spin Rate		Voc (V)	Jsc (mA/cm2)	FF (%)	PCE (%)
4B	10 mg/mL in CB	2000 rpm	Average	0.99 ± 0.01	19.96 ± 0.74	71.68 ± 3.49	14.22 ± 0.93
			Highest	1.02	20.34	75.96	15.76
4C	10 mg/mL in CB	2000 rpm	Average	1.06 ± 0.01	19.02 ± 0.42	60.77 ± 3.45	12.29 ± 0.90
			Highest	1.06	19.78	63.56	13.33
6A	10 mg/mL in CB	2000 rpm	Average	0.88 ± 0.02	14.12 ± 0.71	47.91 ± 2.56	5.98 ± 0.50
			Highest	0.89	14.89	49.82	6.60
6B	10 mg/mL in CB	2000 rpm	Average	0.90 ± 0.09	14.65 ± 0.73	43.63 ± 4.09	5.77 ± 0.80
			Highest	0.91	15.07	49.23	6.75
6D	10 mg/mL in CB	2000 rpm	Average	0.94 ± 0.02	16.60 ± 0.69	48.64 ± 2.89	7.62 ± 0.77
			Highest	0.97	17.06	51.68	8.55
7A	10 mg/mL in CB	2000 rpm	Average	0.93 ± 0.01	16.93 ± 0.64	61.63 ± 3.25	9.75 ± 0.75
			Highest	0.96	17.17	67.89	11.19

7B	10 mg/mL in CB	2000 rpm	Average	0.99 ± 0.01	18.72 ± 0.61	57.73 ± 2.66	10.70 ± 0.63
			Highest	1.00	19.73	59.81	11.80
7C	7.5 mg/mL in CB	3000 rpm	Average	1.06 ± 0.02	20.25 ± 0.55	65.61 ± 1.91	14.04 ± 0.79
			Highest	1.08	20.68	68.71	15.35
9A	10 mg/mL in CB	2000 rpm	Average	0.87 ± 0.01	13.48 ± 0.60	41.58 ± 1.52	4.88 ± 0.28
			Highest	0.88	13.96	42.28	5.19
9B	10 mg/mL in CB	2000 rpm	Average	0.88 ± 0.02	18.90 ± 0.54	49.76 ± 1.74	8.33 ± 0.42
			Highest	0.91	19.95	51.35	9.32
9D	10 mg/mL in CB	2000 rpm	Average	1.00 ± 0.02	16.11 ± 1.05	49.91 ± 3.04	8.05 ± 0.91
			Highest	1.01	17.23	52.14	9.07
10B	8 mg/mL in CB:CF	2000 rpm	Average	1.01 ± 0.01	18.67 ± 0.50	65.59 ± 1.06	12.41 ± 0.63
			Highest	1.02	19.17	66.75	13.05
10C	7.5 mg/mL in CB	3000 rpm	Average	1.08 ± 0.01	20.37 ± 0.65	67.05 ± 0.82	14.71 ± 0.69
			Highest	1.09	21.12	67.73	15.59

When the table above was investigated, it was seen that the highest efficiency values were obtained in cells produced with HTM 4B, HTM 4C, HTM 7C, and HTM 10C polymers. While the highest efficiency of 20.06% was obtained in the reference cell (doped spiro), cells containing HTM 4B, HTM 4C, HTM 7C, and HTM 10C hole transport layers (undoped) worked with 15.76%, 13.33%, 15.35%, and 15.59% power conversion efficiencies, respectively (Table 3-9).

Table 3-9. Photovoltaic parameters of cells including reference and HTM 4B, HTM 4C, HTM 7C, HTM 10C

HTM		V_{oc} (V)	J_{sc} (mA/cm^2)	FF (%)	PCE (%)
Reference	Average	1.15 ± 0.02	22.14 ± 0.63	73.56 ± 3.63	18.77 ± 1.17
	Highest	1.16	22.99	75.24	20.06
HTM 4B	Average	0.99 ± 0.01	19.96 ± 0.74	71.68 ± 3.49	14.22 ± 0.93
	Highest	1.02	20.34	75.96	15.76
HTM 4C	Average	1.06 ± 0.01	19.02 ± 0.42	60.77 ± 3.45	12.29 ± 0.90
	Highest	1.06	19.78	63.56	13.33
HTM 7C	Average	1.06 ± 0.02	20.25 ± 0.55	65.61 ± 1.91	14.04 ± 0.79
	Highest	1.08	20.68	68.71	15.35
HTM 10C	Average	1.08 ± 0.01	20.37 ± 0.65	67.05 ± 0.82	14.71 ± 0.69
	Highest	1.09	21.12	67.73	15.59

Figure 3-17 displays the JV plot of the highest efficiency values of the cells containing the reference and HTM 4B, HTM 4C, HTM 7C and HTM 10C hole transport layers, and the box charts of all the cells produced are shown in Figure 3-18.
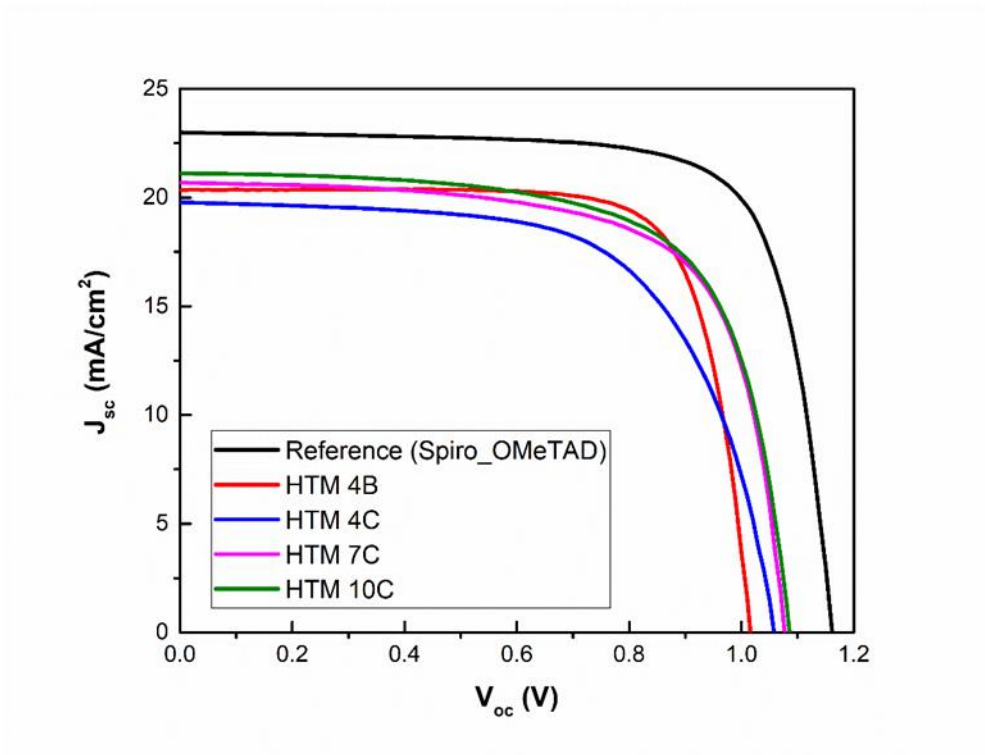
Figure 3-17. JV plot of best devices of reference and HTM 4B, HTM 4C, HTM 7C, HTM 10C
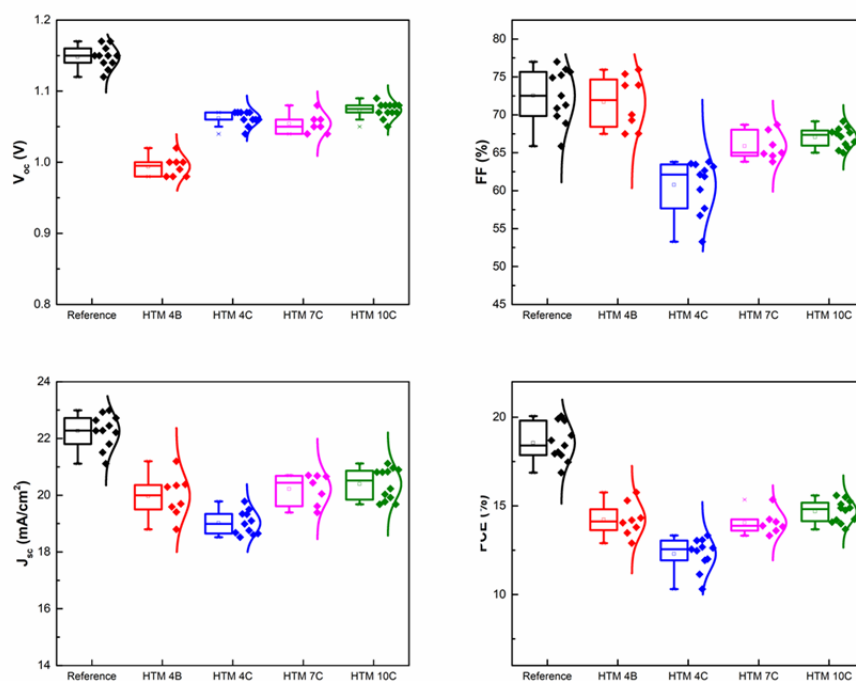
Figure 3-18. Box charts of reference and HTM 4B, HTM 4C, HTM 7C, HTM 10C cells (Voc, Jsc, FF% ve PCE%)

3.1.2.1 Stability

In order to observe the stability performances of the cells prepared with different polymer hole transport layers and Spiro-OMeTAD, the cells were kept at room temperature, 15% humidity, in the dark, and in an oxygen-containing environment for four months (approximately 3000 hours). When the efficiency values were measured at the end of four months, it was observed that the stability level obtained with the polymers was significantly better compared to Spiro-OMeTAD. At the end of four months, reference cells retained an average of 56% of efficiency, while HTM 4B retained 89%, HTM 7C 86%, HTM 10C 68%, and with the best performance, HTM 4C retained 93%. Other photovoltaic parameters can be found in Table 3-10.

Table 3-10. Photovoltaic parameters of cells including reference and HTM 4B, HTM 4C, HTM 7C, HTM 10C after four months

HTM		V_{oc} (V)	J_{sc} (mA/cm^2)	FF (%)	PCE (%)	SPO (%)
Reference	Average	1.01 ± 0.04	17.16 ± 1.73	61.03 ± 3.15	10.52 ± 1.26	56.0
	Highest	1.10	17.75	63.60	12.42	61.9
HTM 4B	Average	0.99 ± 0.02	18.65 ± 0.46	68.60 ± 2.95	12.63 ± 0.73	88.8
	Highest	1.00	18.72	73.17	13.70	86.9
HTM 4C	Average	0.99 ± 0.01	18.66 ± 0.50	61.70 ± 5.70	11.43 ± 1.43	93.0
	Highest	1.00	19.47	70.14	13.66	100
HTM 7C	Average	1.04 ± 0.01	17.91 ± 1.19	64.63 ± 3.38	12.09 ± 1.12	86.1
	Highest	1.06	19.08	68.37	13.83	90.1
HTM 10C	Average	1.03 ± 0.01	17.68 ± 1.26	55.13 ± 2.61	10.07 ± 1.24	68.5
	Highest	1.04	19.31	57.48	11.55	74.1

Bar graphs of the best devices in the measurements at the end of four months is given in comparison with fresh cells in Figure 3-19. When we look at the JV graphs of the best devices, we see that there was a severe loss of J_{sc} and FF in the reference cell compared to the cells containing polymer in the measurements after four months. Solar cells were containing polymer hole transport layers almost entirely preserved their efficiency during this time.
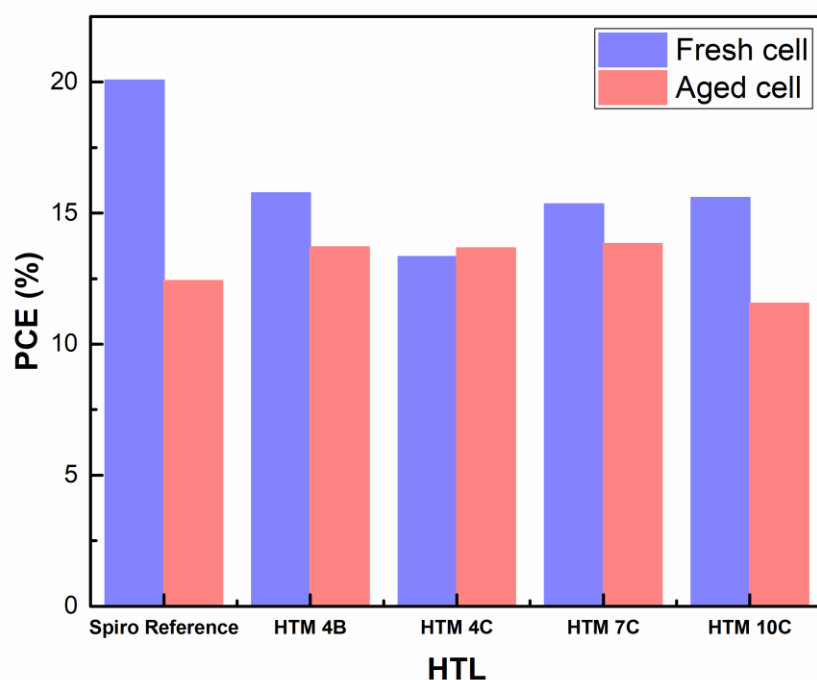
Figure 3-19. Bar graphs of best devices of aged and fresh reference and HTM 4B, HTM 4C, HTM 7C, HTM 10C cells

The contact angle images of the polymers coated as a hole transport layer on the perovskite layer are given in Figure 3-20. Looking at the images, the angle of the water with the perovskite film is 70.2°, while the angle measured in the reference cell containing Spiro-OMeTAD on perovskite is 85.9°. In films of a polymer layer on perovskite, this angle was measured as 87.4° for HTM 4B, 104.0° for HTM 4C, 101.8° for HTM 7C, and 99.8° for HTM 10C. It is seen that all polymer-containing films have a higher contact angle compared to the perovskite film and the reference sample. The measurement results prove that the polymer films have a highly hydrophobic surface, and according to the JV results, these results also positively affect cell stability. As a result, much more stable solar cells were produced with DPP-based polymers compared to pristine Spiro-OMeTAD perovskite solar cells.
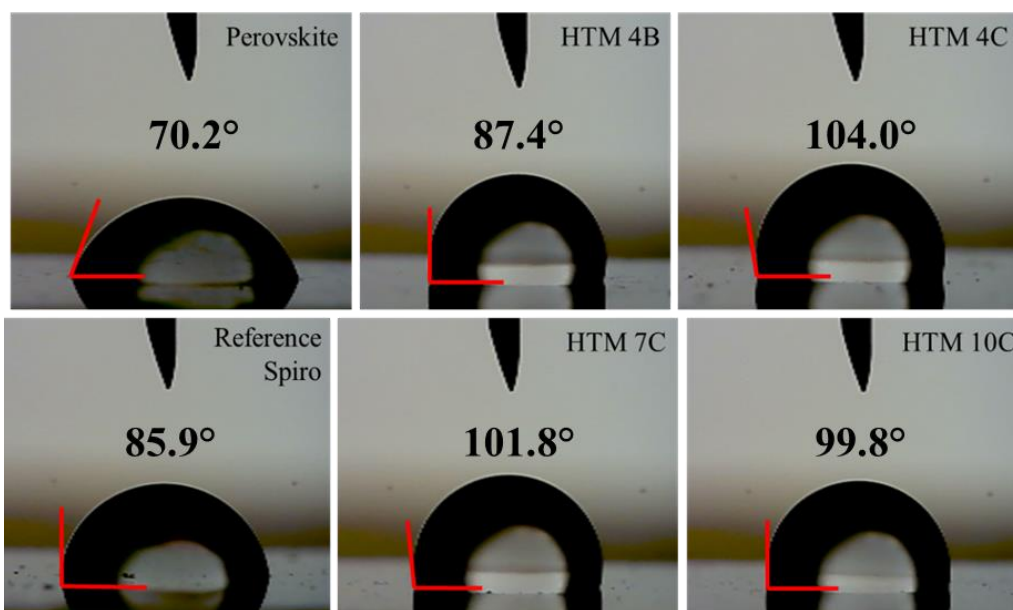
Figure 3-20. Water contact angle images of perovskite, reference and HTM 4B, HTM 4C, HTM 7C and HTM 10C coated layers on perovskite

3.2 Outlook of the Chapter

As mentioned, this chapter focuses on dopant-free organic DPP polymers because of their interest to researchers and applicability in the most recent generation of photovoltaic systems[96–98]. As explained in the previous section, HTM is an essential element in creating more efficient and stable PSCs. Besides providing high stability, the most significant advantage of polymer HTMs is that they can be optimized by synthesis for the desired performance. The doping phenomenon involves introducing one or more chemicals that can donate or remove electrons into the conductive material so that the material becomes negatively or positively charged; that is, it behaves like an n-doped or p-doped material, respectively. However, while doping generally increases hole mobility, it affects cell efficiency adversely. Since LiTFSI is a very hygroscopic salt, it causes the absorption of moisture into the HTM film or can generate pinholes in the film[99]. The aforementioned factors moved researchers towards the notion of dopant-free HTMs.

This chapter introduced DPP polymers with different aromatic groups and alkyl chains as HTMs in PSCs. First, we noticed that the branched alkyl chain group performed better than the linear alkyl chain group in the thiophene aromatic group-containing DPP polymer. Conversely, those with linear alkyl chains performed better in DPP polymers containing an aromatic furan group. However, despite experimenting with other alky chains and donor groups, we could not overcome the solubility issue in polymers containing furan. This resulted in the manufacture of low-quality films, leading to low cell efficiencies.

DPP polymers were synthesized according to a specific order, and it was planned to be compared and evaluated according to different donor groups and different alkyl chains. However, it is challenging to classify polymers and establish an association between them due to varying molecular weights and solubility issues. Furthermore, polymer solubility and film characteristics varied between different batches, resulting in fluctuations in device performance from batch to batch. Additionally, perovskite performance fluctuates throughout the year, it is inaccurate to draw a correlation between cells manufactured with polymer from various time periods.

In order to solve this problem, MoO_3 and CuI layers were coated between the HTM and Au layers and the device performances were examined, but the desired efficiency increase was not observed. Optimization studies will be carried out with other electron-blocking layer coatings in order to obtain better results.

As a result, it will be attempted to find an appropriate electron-blocking material to develop the device's efficiency. Furthermore, DPP polymers with good solubility and performance in various trials will be grouped, and simultaneous experiments will be conducted to compare device performance as a future work.

CHAPTER 4

PT-TPA as HTM in PSCs

In this chapter, a novel hole transport material, PT-TPA, (4.4'.4''.4'''-(pyrazine-2.3.5.6-tetrayl)tetrakis(N.N-bis(4-methoxyphenyl)aniline)) (Figure 4-1), is introduced as an alternative to Spiro-OMeTAD. Overall PT-TPA revealed appropriate characteristics as an HTL candidate in the n-i-p structure with promising photovoltaic performance, the most remarkable being remarkable stability compared to Spiro-OMeTAD. Chemical structure of PT-TPA molecule is given in Figure 4-1.
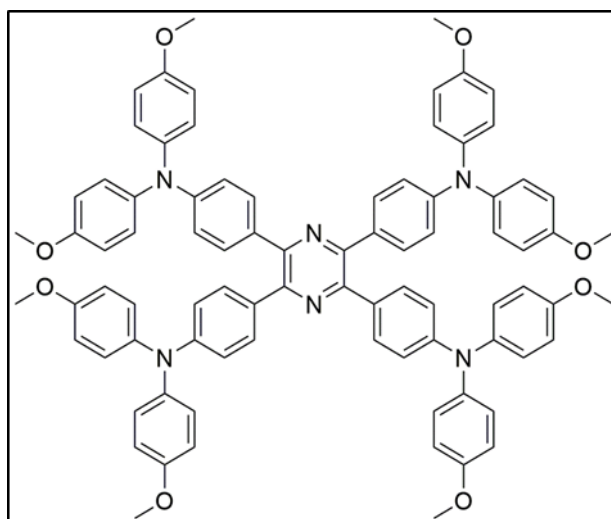
Figure 4-1. Chemical Structure of PT-TPA

It is important to note here that PT-TPA studies were carried out throughout in different periods of the year, and changes were observed in the photovoltaic parameters of the reference perovskite solar cells at different seasons of the year between periods. Therefore, different efficiency values were measured in different sets for the same reference cell due to this issue. Additionally, while the work of on the PT-TPA hole transport layer was continuing in progress, the material produced

was synthesized with again 4 different batches was used. Due to the fact that, minimal efficiency changes arising from the differences between batches are seen in the study results.

4.1   Results and Discussions

Our initial studies started with cyclic voltammetry (CV) and the UV-Vis absorbance measurements to determine the band gap of PT-TPA. E_{HOMO} is calculated as -5.40 eV from the CV measurement (Figure 4-2a). Using the ultraviolet–visible (UV–vis) absorption spectra and Tauc plots, the optical bandgap (Eg) of the perovskite films was calculated as 2.61 eV as shown in Figure 4-2b. Related band energy levels for PT-TPA film is given in Table 4-1.
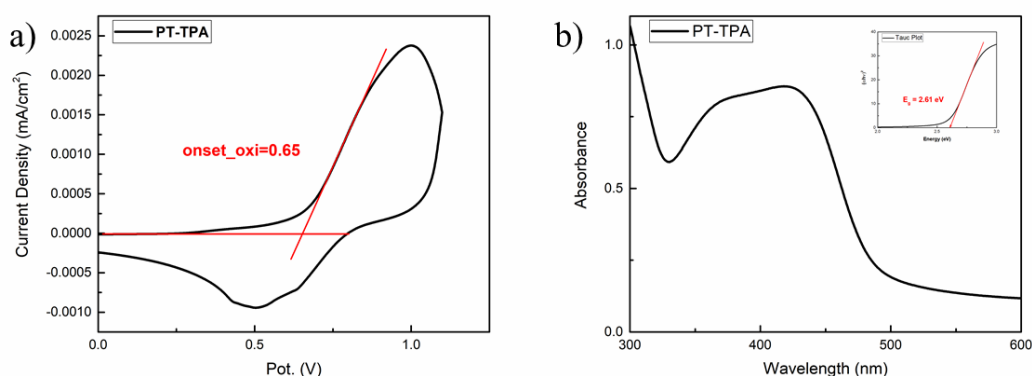
Figure 4-2. a) Cyclic voltammogram and b) UV-Vis absorbance spectrum of PT-TPA film

Table 4-1. Electrochemical data of PT-TPA

	Eg (eV)	HOMO (eV)	LUMO (eV)
PT-TPA	2.61	-5.40[a]	-2.79[b]

a: Experimental values (HOMO levels are measured by cyclic voltammetry).

b: Theoretical calculation values; $E_{LUMO} = E_{HOMO} + Eg$.
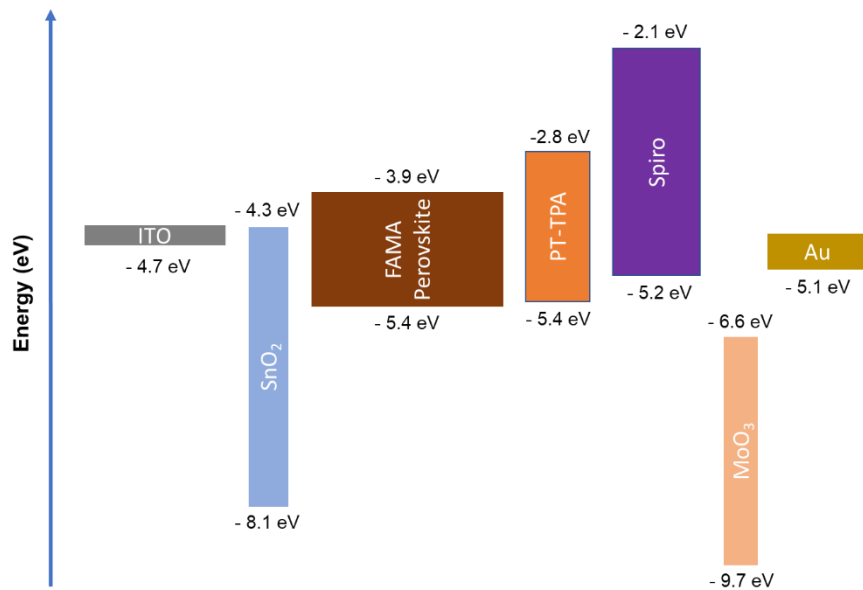
Figure 4-3. Energy level diagram of the corresponding materials used in perovskite solar cells

A very clear solution is obtained by dissolving it in dichlorobenzene with PT-TPA hole transport material (Figure 4-4a) and the film-forming capability of the solution is likewise excellent, since it covers the perovskite surface entirely and without aggregation (Figure 4-4b).
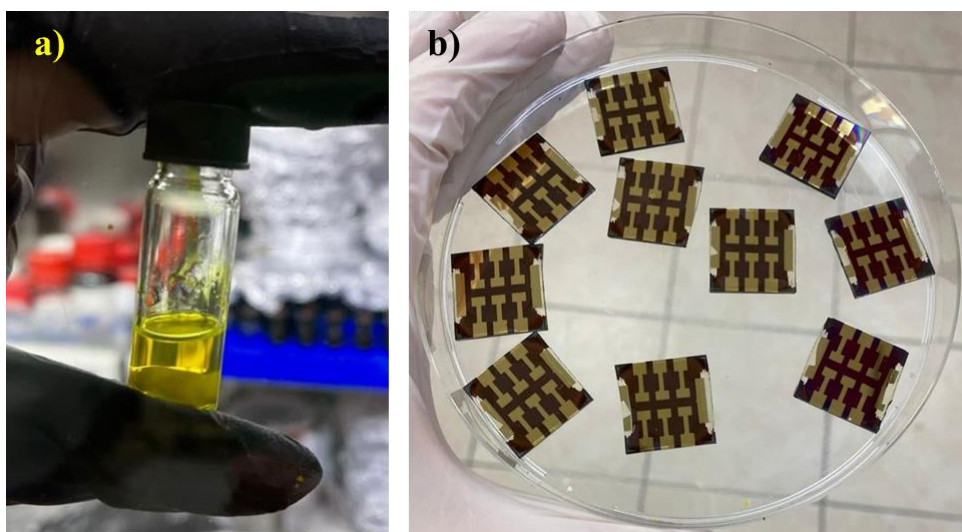
Figure 4-4. a) PT-TPA solution, b) device images coated with PT-TPA

SEM images clearly demonstrated that like spiro-OMeTAD, pin-hole free surface coating is obtained with PT-TPA. Since we aimed to achieve a dopant free HTM with PT-TPA, lower concentrations compared to Spiro-OMeTAD were used throughout our studies which resulted in thinner films and the thickness of the film was measured as 169 nm vs 240 nm for the reference. (PT-PA coated films viewed backwards)
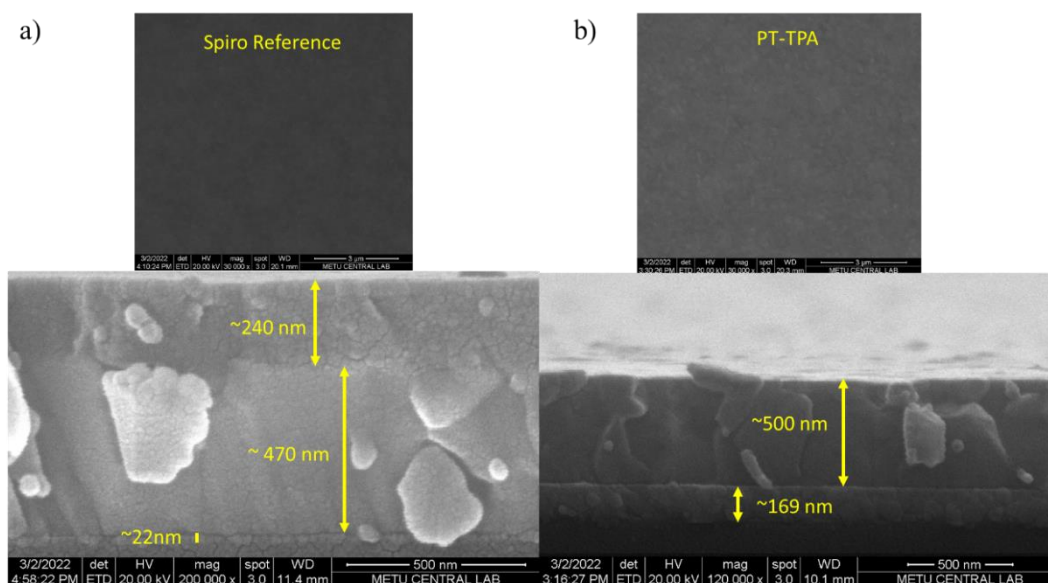
Figure 4-5. Top-view and cross-section SEM images of a) Spiro-OMeTAD and b) PT-TPA films with a device structure of ITO/SnO$_2$/Perovskite/HTM

PL spectra of the perovskite only, Spiro-OMeTAD coated and PT-TPA coated films are displayed in Figure 4-6. PT-TPA film was determined to have a slightly higher but comparable PL intensity compared to Spiro-OMeTAD, which demonstrated that PT-TPA can minimize radiation-free recombination and passivate the perovskite surface effectively.
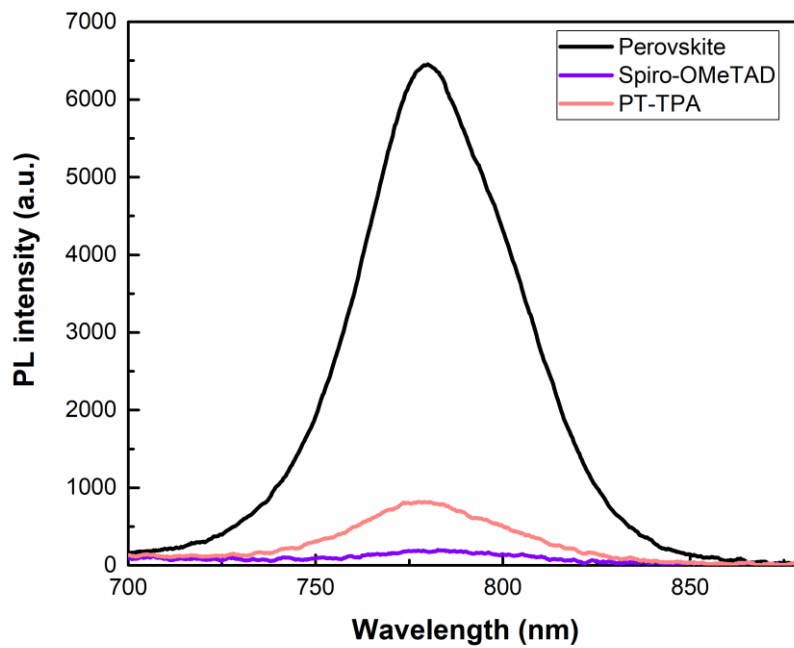
Figure 4-6. PL spectra of the perovskite, Spiro-OMeTAD and PT-TPA films

4.2 Device Optimizations

4.2.1 Concentration Optimization

The first study with the PT-TPA material was concentration optimization. Spiro-OMeTAD, the reference material for the hole transport layer, is commonly prepared at a 72.3 mg/mL concentration for the pristine perovskite solar cells in the literature. Since we are aiming dopant free hole transport layers, lower concentrations were aimed towards having thinner films to prevent hole conductivity issues. Hence while preparing PT-TPA solutions 3⁄4, 1⁄2 and 1⁄4 mass ratio with respect to Spiro-OMeTAD were calculated and solutions were prepared according to these quantities. When we look at the cell performances of the solutions prepared by dissolving 18 mg, 36 mg, and 54 mg of PT-TPA in 1 mL of dichlorobenzene, it was observed that the photovoltaic performances decreased as the amount of PT-TPA in the solution

increased. As the concentration increased and layer thickness increased, significant decrease in short circuit current and fill factor was observed. The mean efficiency value for the 18 mg/mL concentration was 13.78%, while it was 10.15% for 36 mg/mL and 6.90% for 54 mg/mL concentrations. Detailed photovoltaic parameters can be seen in Table 4-2. The efficiency of the cell working best at 18 mg/mL concentration was 15.35%, and with short circuit current (J_{sc}) of 19.86 mA/cm^2, open circuit voltage (V_{oc}) of 1.04 V and fill factor FF of 69.18%.

Table 4-2 Photovoltaic parameters of refererence cell and different concentrations of PT-TPA

HTM		V_{oc} (V)	J_{sc} (mA/cm^2)	FF (%)	PCE (%)
Reference	Average	1.07 ± 0.03	20.00 ± 0.61	68.21 ± 4.47	14.69 ± 1.20
	Highest	1.11	20.24	73.87	16.54
18 mg/mL	Average	1.04 ± 0.02	19.73 ± 0.37	67.44 ± 4.24	13.78 ± 0.90
	Highest	1.04	19.86	74.51	15.35
36 mg/mL	Average	1.04 ± 0.01	19.13 ± 0.43	50.86 ± 3.87	10.15 ± 0.70
	Highest	1.04	18.92	58.71	11.52
54 mg/mL	Average	1.01 ± 0.02	17.29 ± 1.44	39.40 ± 4.25	6.90 ± 1.06
	Highest	1.03	17.54	45.49	8.19

Box charts of all cells are shown in Figure 4-7. Efficiencies very close to the reference were obtained with 18 mg/mL, and studies were continued to optimize the concentration even further.
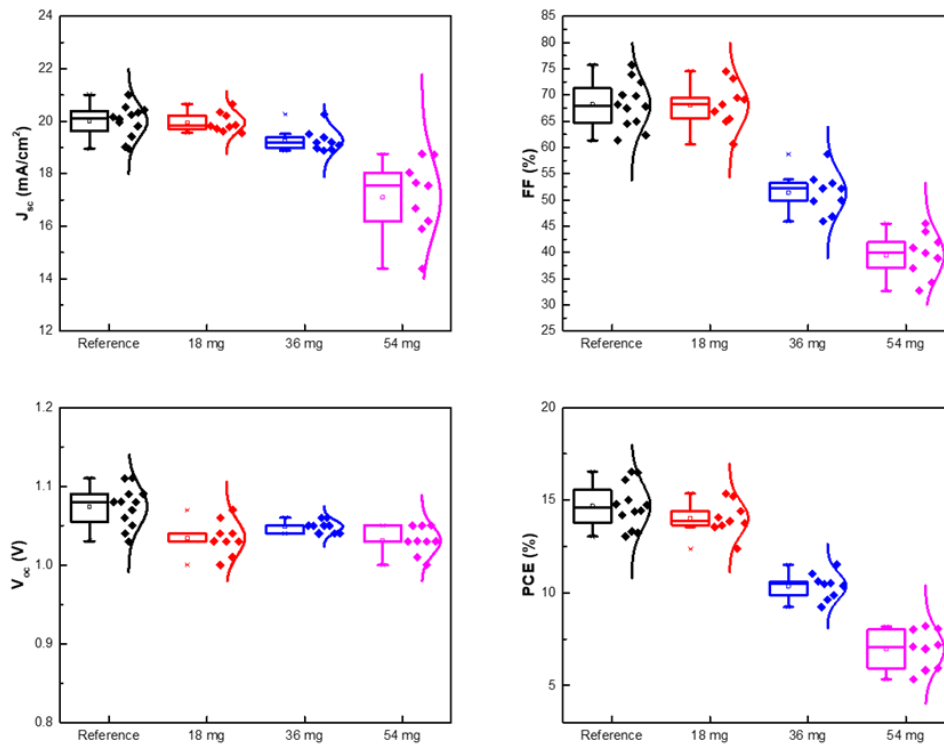
Figure 4-7. Box charts of different concentrations of PT-TPA (Voc, Jsc, FF% and PCE%)

Four solutions were prepared at 12, 15, 18, and 21 mg/mL concentrations in the following study. Although very close results were obtained, the best efficiency values were obtained with PT-TPA solution at a 15 mg/mL concentration (Table 4-3). The efficiency of the cell working best at this concentration was 14.56%, and the parameters were measured as J_{sc} 20.29 mA/cm^2, V_{oc} 1.04 V, and FF 69.18%, respectively.

Table 4-3. Photovoltaic parameters of cells including reference and PT-TPA hole transport layer prepared at different concentrations.

HTM		V_{oc} (V)	J_{sc} (mA/cm^2)	FF (%)	PCE (%)
Reference	Average	1.13 ± 0.01	20.70 ± 0.52	78.42 ± 1.07	18.40 ± 0.76
	Highest	1.16	21.15	80.70	19.75
12 mg/mL	Average	1.02 ± 0.01	19.06 ± 0.45	60.25 ± 3.93	11.66 ± 0.85
	Highest	1.02	19.30	66.28	13.05
15 mg/mL	Average	1.04 ± 0.01	19.98 ± 0.26	64.96 ± 2.32	13.41 ± 0.58
	Highest	1.04	20.29	69.18	14.56
18 mg/mL	Average	1.04 ± 0.01	19.46 ± 0.51	63.93 ± 2.81	12.87 ± 0.91
	Highest	1.05	19.92	67.44	14.05
21 mg/mL	Average	1.04 ± 0.02	19.32 ± 0.68	63.23 ± 3.47	12.70 ± 0.81
	Highest	1.04	20.37	64.72	13.67

Box charts of all cells produced are given in Figure 4-8. In the films prepared with 12 mg/mL, uniformity and coverage was an issue which is the main reason for the lower number of data points for 12 mg/mL seen in box charts. When considering the average values, the concentration with the best results was 15 mg/mL, and the remaining optimization studies were conducted at this concentration.
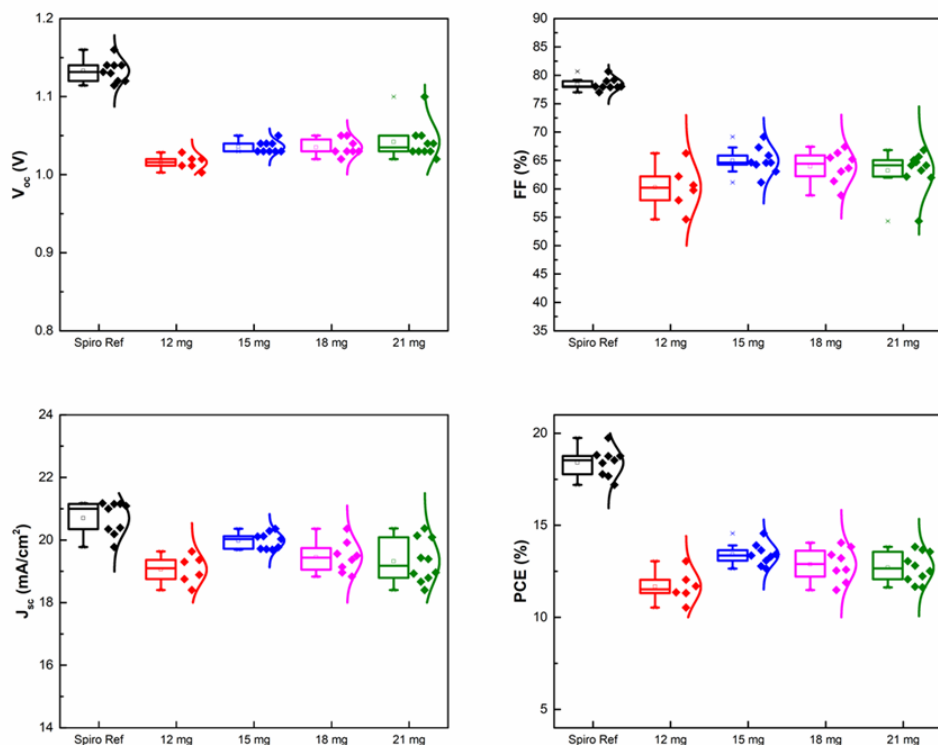
Figure 4-8. Box charts of cells including reference and PT-TPA hole transport layer prepared at different concentrations (V_{oc}, J_{sc}, FF% and PCE%)

4.2.1.1 Spin rate optimization

An optimization study for the spin rate was pursued after determining the optimal concentration for the PT-TPA. The samples were prepared at spin rates of 1000, 2000, 3000, 4000, and 5000 rpm, corresponding to the reference cell's spin rate of 3000 rpm. As spin rate was increased and thinner films were attained, the V_{oc} and FF values of the cells decreased, resulting in a slight drop in cell efficiency. This minimal decrease is attributed to lower uniformity and coverage at these spin rates.

Table 4-4 demonstrates that the best cell of this set was at 17.01% with spin rate of 1000 rpm. The cell other parameters were as follows: J_{sc} 21.68 mA/cm^2, V_{oc} 1.05V,

and FF 75.79%. Figure 4-9 depicts the JV plot best cells achieved at all spin speeds in this set.

Table 4-4. Photovoltaic parameters of cells including PT-TPA hole transport layer prepared at different spin speeds between 1000-5000 rpm

HTM		V_{oc} (V)	J_{sc} (mA/cm^2)	FF (%)	PCE (%)
1000 rpm	Average	1.04 ± 0.01	20.58 ± 0.66	73.66 ± 1.27	15.81 ± 0.77
	Highest	1.05	21.68	74.67	17.01
2000 rpm	Average	1.02 ± 0.01	20.94 ± 0.53	74.51 ± 1.42	15.92 ± 0.56
	Highest	1.04	21.19	75.79	16.70
3000 rpm	Average	1.00 ± 0.01	21.19 ± 0.52	74.41 ± 1.88	15.81 ± 0.60
	Highest	1.01	21.52	75.68	16.45
4000 rpm	Average	1.00 ± 0.02	20.98 ± 0.37	72.80 ± 1.82	15.21 ± 0.32
	Highest	1.02	21.27	72.95	15.83
5000 rpm	Average	0.99 ± 0.02	20.65 ± 0.79	71.82 ± 1.86	14.67 ± 0.75
	Highest	0.99	21.74	73.29	15.77
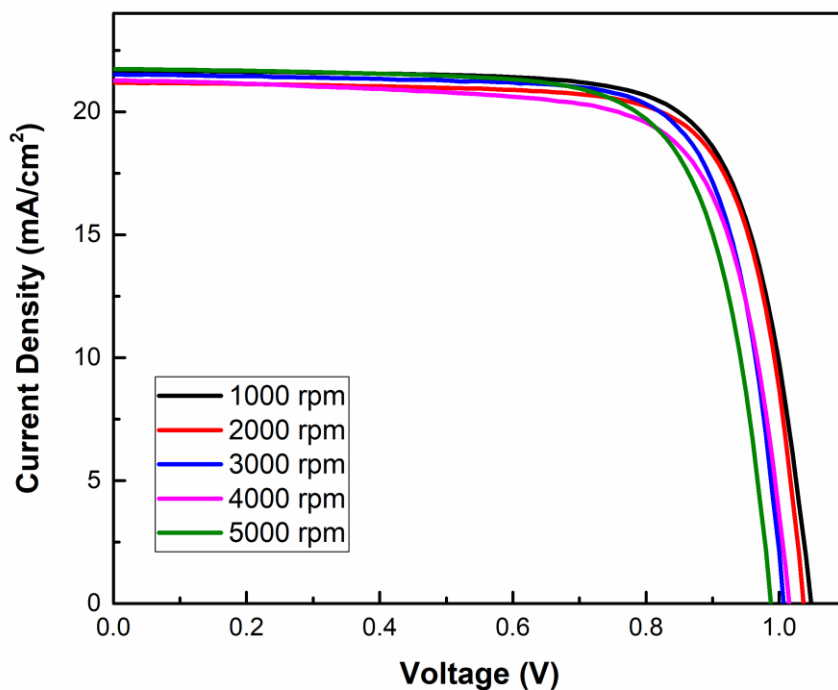
Figure 4-9 JV plot of best devices including PT-TPA hole transport layer at different spin speeds between 1000-5000 rpm

However, based on the average data, 15.81% efficiency was obtained with 1000 rpm, while 15.92% efficiency was obtained with 2000 rpm. In Figure 4-10, box charts of all of the cells fabricated are given. Considering these values, which are very close to each other, a more detailed optimization study was initiated.
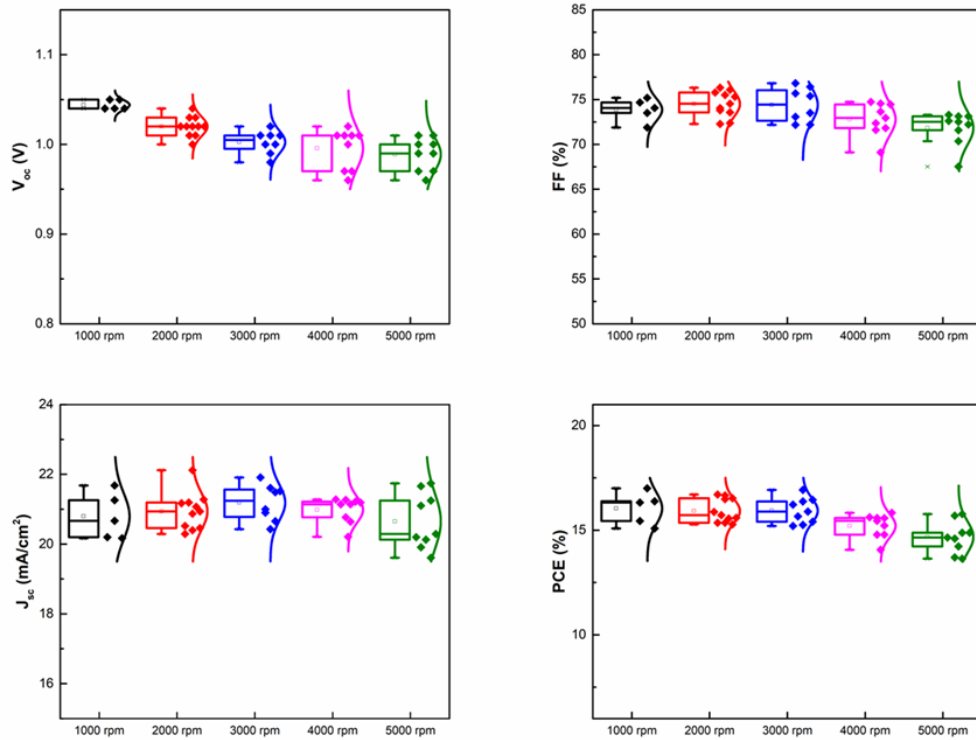
Figure 4-10. Box charts of cells including PT-TPA hole transport layer prepared at
spin speeds 1000-5000 rpm (V_{oc}, J_{sc}, FF% and PCE%)

In the next run, PT-TPA was coated with different spin speeds of 500, 1000, 1500, and 2000 rpm to find the optimal spin rate. In samples coated at 500 rpm, the PT-TPA layer was extraordinarily thick and hindered charge transmission. The best cell in this set was obtained with a spin speed of 2000 rpm and an efficiency of 16.65% (J_{sc} : 22.62 mA/cm^2, V_{oc} : 1.01 V, and FF : 72.88%). As shown in Table 4-5, the average value of J_{sc} increased from 500 rpm to 2000 rpm, and the maximum J_{sc} value was observed in the cells with 2000 rpm. The integrated J_{sc} values of solar cells were calculated to be 20.42 mA/cm^2, 20.63 mA/cm^2, 20.92 mA/cm^2, and 20.80 mA/cm^2 for 500, 1000, 1500, and 2000 rpm PT-TPA, respectively. They support the conclusions obtained from the J-V measurements. The graph in Figure 4-11 depicting external quantum efficiency (EQE) also confirms this J_{sc} improvement.

Figure 4-12 displays the JV plot of the best cells achieved at all spin speeds in this set.

Table 4-5. Photovoltaic parameters of cells including reference and PT-TPA hole transport layer prepared at different spin speeds between 500-2000 rpm

HTM		V_{oc} (V)	J_{sc} (mA/cm^2)	FF (%)	PCE (%)
Reference	Average	1.12 ± 0.01	20.41 ± 0.63	76.36 ± 1.58	17.46 ± 0.86
	Highest	1.14	21.17	77.93	18.81
500 rpm	Average	1.03 ± 0.01	19.61 ± 0.54	64.81 ± 2.75	13.04 ± 0.74
	Highest	1.03	20.51	68.53	14.48
1000 rpm	Average	1.03 ± 0.01	20.79 ± 0.52	68.33 ± 2.67	14.58 ± 0.88
	Highest	1.03	21.34	73.65	16.19
1500 rpm	Average	1.02 ± 0.01	20.62 ± 0.66	69.50 ± 1.05	14.67 ± 0.60
	Highest	1.03	21.59	69.58	15.47
2000 rpm	Average	1.01 ± 0.01	21.23 ± 0.71	72.58 ± 2.38	15.61 ± 0.61
	Highest	1.01	22.62	72.88	16.65
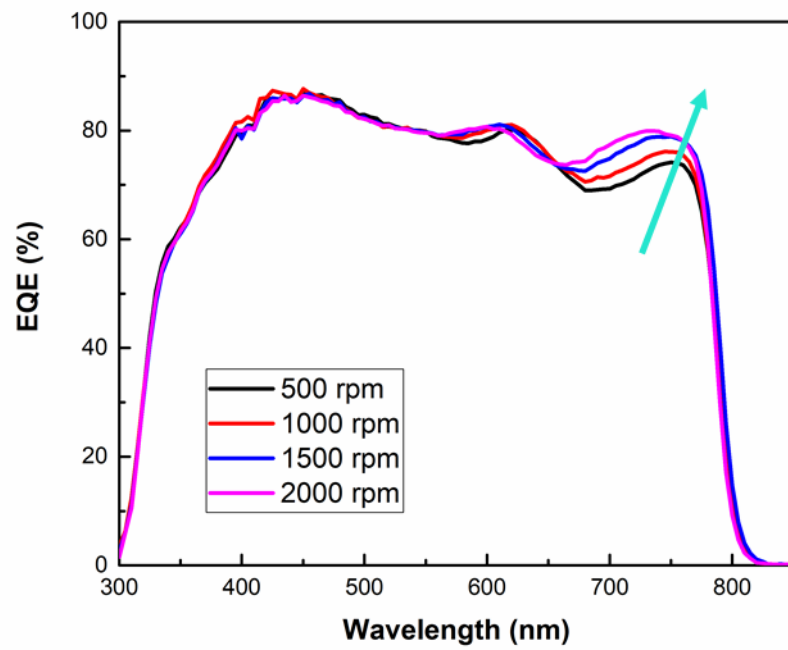
Figure 4-11. External quantum efficiency (EQE) graph of the PT-TPA hole transport layer with different spin speeds 500-2000 rpm
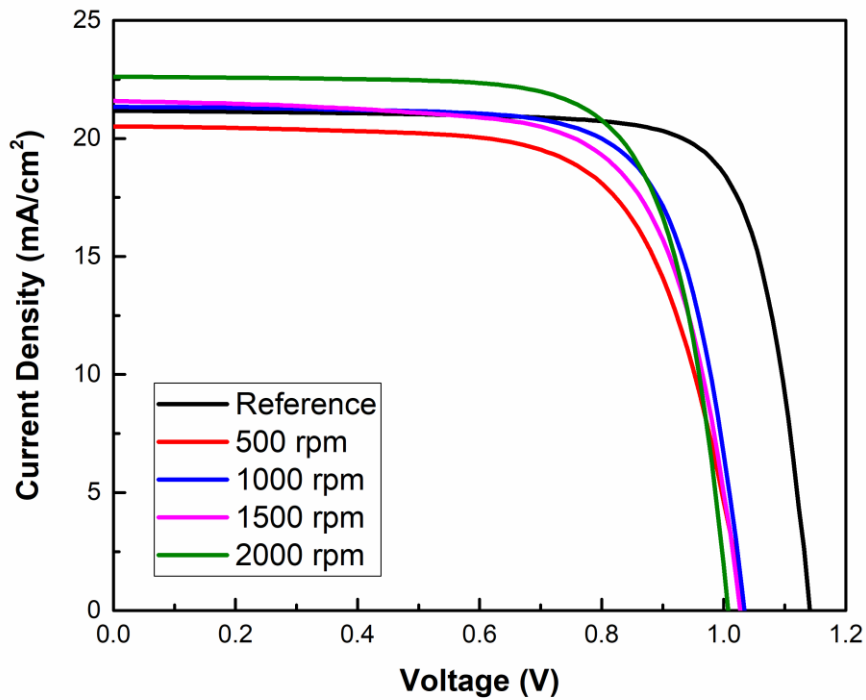
Figure 4-12. JV plot of best devices including reference and PT-TPA hole transport layer at different spin speeds between 500-2000 rpm

Considering the average values, the samples produced at 2000 rpm performed better than the others and had an efficiency of 15.61% on average. Other parameters of the cells are as follows J_{sc} 21.23 mA/cm^2, V_{oc} 1.01 V, and FF 72.58%, respectively. Box charts containing all the cells are depicted in the following Figure 4-13.
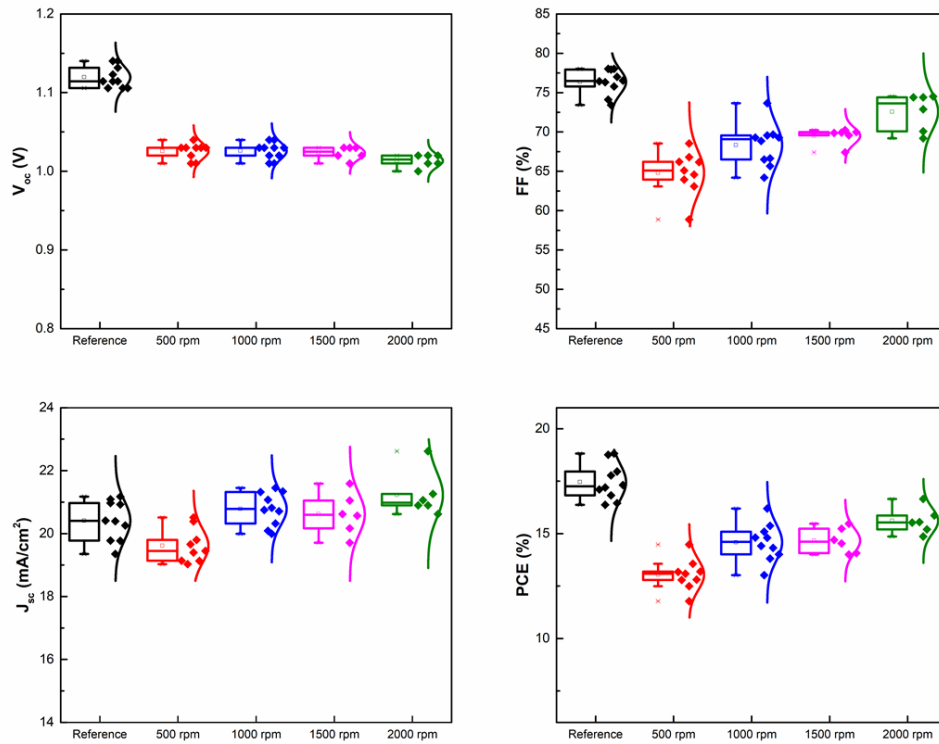
Figure 4-13. Box charts of cells including reference and PT-TPA hole transport layer prepared at spin speeds 500-2000 rpm (V_{oc}, J_{sc}, FF% and PCE%)

4.2.2   MoO$_3$ Layer on HTL

During the optimization studies, MoO$_3$ was coated by evaporation method and its thickness was 20 nm. In order to determine the optimal thickness of MoO$_3$ layer, samples were coated at 0, 5, 10, 20, and 30 nm in the set established for this purpose.

Table 4-6. Photovoltaic parameters of cells including MoO_3 layer on PT-TPA hole transport layer with different thicknesses

HTM		V_{oc} (V)	J_{sc} (mA/cm^2)	FF (%)	PCE (%)
No MoO$_3$	Average	0.98 ± 0.02	19.21 ± 0.95	59.83 ± 2.94	11.28 ± 1.06
	Highest	0.97	20.09	64.85	12.64
5 nm MoO$_3$	Average	1.04 ± 0.01	20.80 ± 0.44	74.20 ± 0.96	16,00 ± 0.49
	Highest	1.04	21.44	75.64	16.87
10 nm MoO$_3$	Average	1.02 ± 0.02	20.69 ± 0.44	72.01 ± 1.94	15.16 ± 1.94
	Highest	1.03	21.27	73.57	16.12
20 nm MoO$_3$	Average	0.98 ± 0.02	20.95 ± 0.56	68.13 ± 2.50	13.93 ± 0.88
	Highest	1.00	20.74	71.19	14.77
30 nm MoO$_3$	Average	0.87 ± 0.04	19.13 ± 1.07	46.74 ± 6.09	8.19 ± 0.95
	Highest	0.90	20.05	53.04	9.57

The most efficient cell was obtained with a 5 nm thick MoO_3 layer, as shown in the Table 4-6, and its efficiency was measured at 16.87%. This cell's other properties are as follows: J_{sc} 21.44 mA/cm^2, V_{oc} 1.04 V, and FF 75.64%. The best efficiencies obtained in other thicknesses were measured as 12.64% for no MoO_3, 16.12% for 10 nm MoO_3, 14.77% for 20 nm MoO_3 and 9.57% for 30 nm, respectively. The best cell graph in the corresponding JV plot is in Figure 4-14.
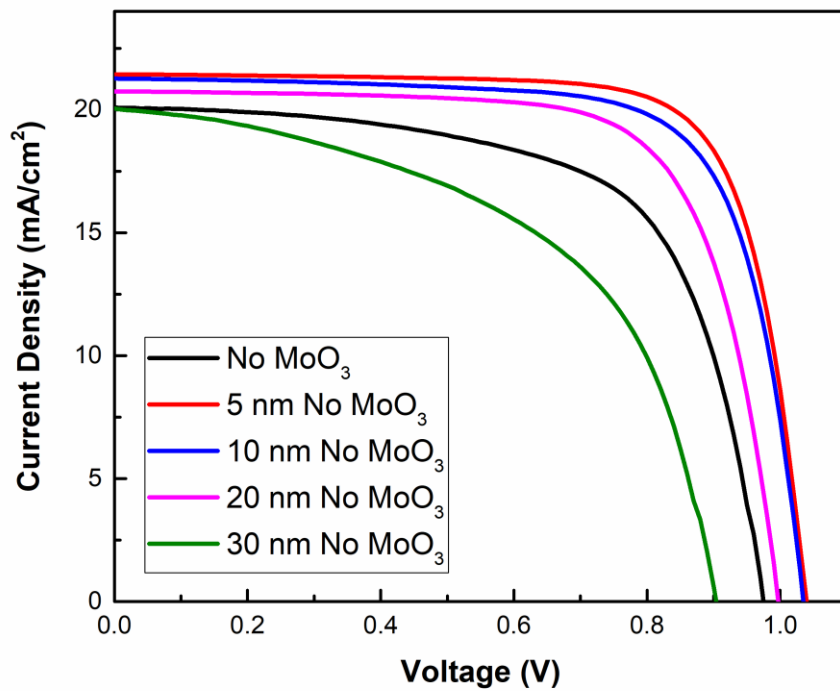
Figure 4-14. JV plot of cells including MoO₃ layer on PT-TPA hole transport layer with different thicknesses

As seen from the box chart in Figure 4-15, the MoO₃ layer with a thickness of 5 nm generated the best results for all parameters. The thickness of 30 nm MoO₃ acted as an insulating layer and number of functioning cells were low.
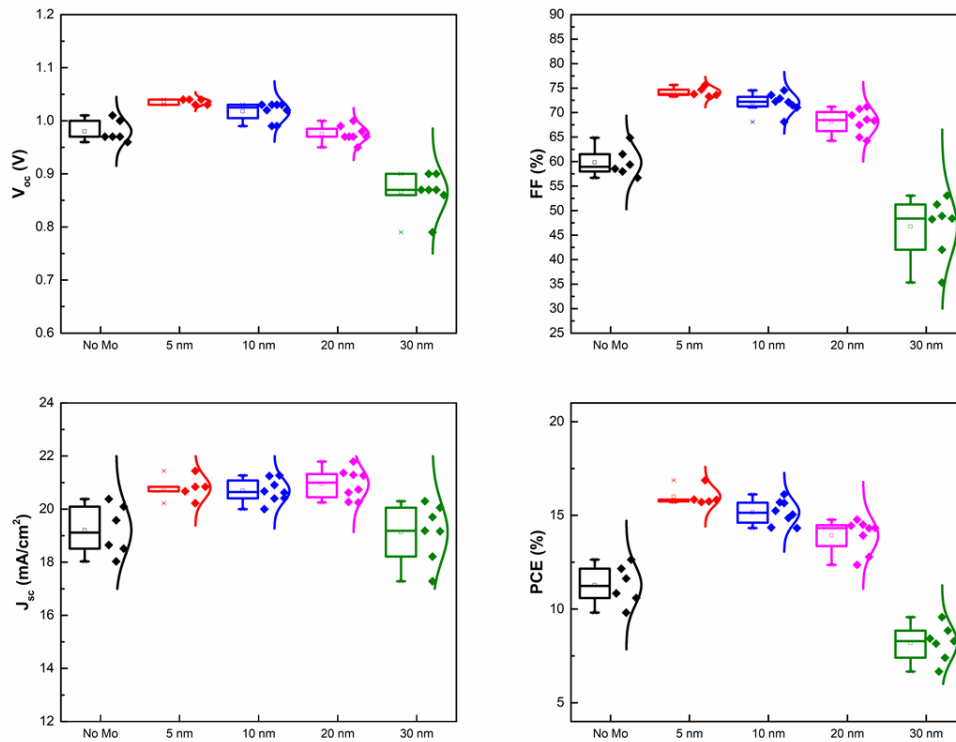
Figure 4-15. Box charts of cells including MoO_3 layer on PT-TPA hole transport layer with different thicknesses (V_{oc}, J_{sc}, FF%, PCE%)

EQE was performed on the cells with the highest efficiencies, and the cell containing MoO_3 with a thickness of 5 nm had the best performance, as predicted (Figure 4-16). The integrated J_{sc} results were calculated for no MoO_3, 5 nm MoO_3, 10 nm MoO_3 and 20 nm MoO_3 coated solar cells as 17.54 mA/cm^2, 21.31 mA/cm^2, 20.44 mA/cm^2, and 18.72 mA/cm^2, respectively which are consistent with the JV measurements. EQE measurements for cells with 30 nm MoO_3 were not conclusive.
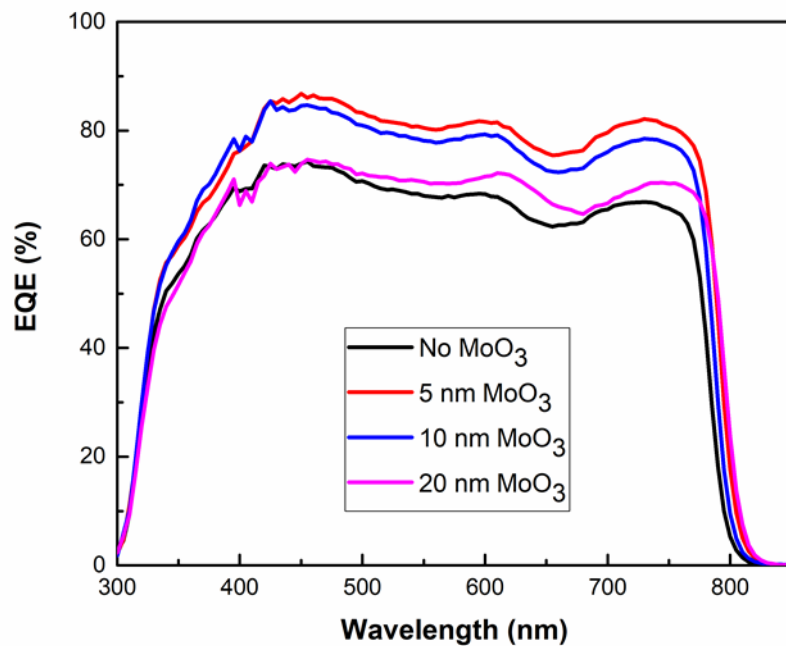
Figure 4-16. External quantum efficiency (EQE) graph of cells including MoO_3 layer on PT-TPA hole transport layer with different thicknesses

4.2.3 Reproducibility

As it is mentioned in Chapter 3, reproducibility is one of the key challenges of perovskite solar cells. A histogram graph in Figure 4-17, shows the PCE distribution for the reference and PT-TPA perovskite solar cells. Notably, the statistical results were derived from around 20 perovskite solar cell devices from multiple batches, indicates high reproducibility of cells produced with PT-TPA. An averaged PCE of 15.91% was achieved over 20 devices with HTM 4B, and the highest PCE is recorded as 17%.
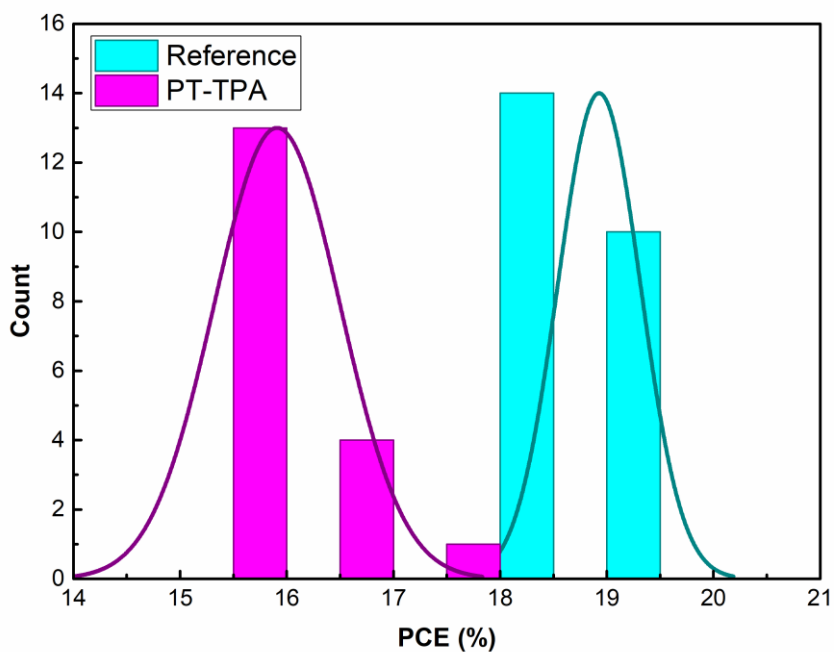
Figure 4-17. Histogram of reference and PT-TPA perovskite solar cells, around 20 devices.

Table 4-7. Photovoltaic parameters of cells including the statistical data of PT-TPA-based devices recorded from different batches of synthesis

HTM		V_{oc} (V)	J_{sc} (mA/cm^2)	FF (%)	PCE (%)
Reference (Spiro)	Average	1.12	20.93	80.77	18.93
	Highest	1.12	21.84	81.03	19.82
PT-TPA	Average	1.03	20.82	74.25	15.91
	Highest	1.05	21.09	77.06	17.00
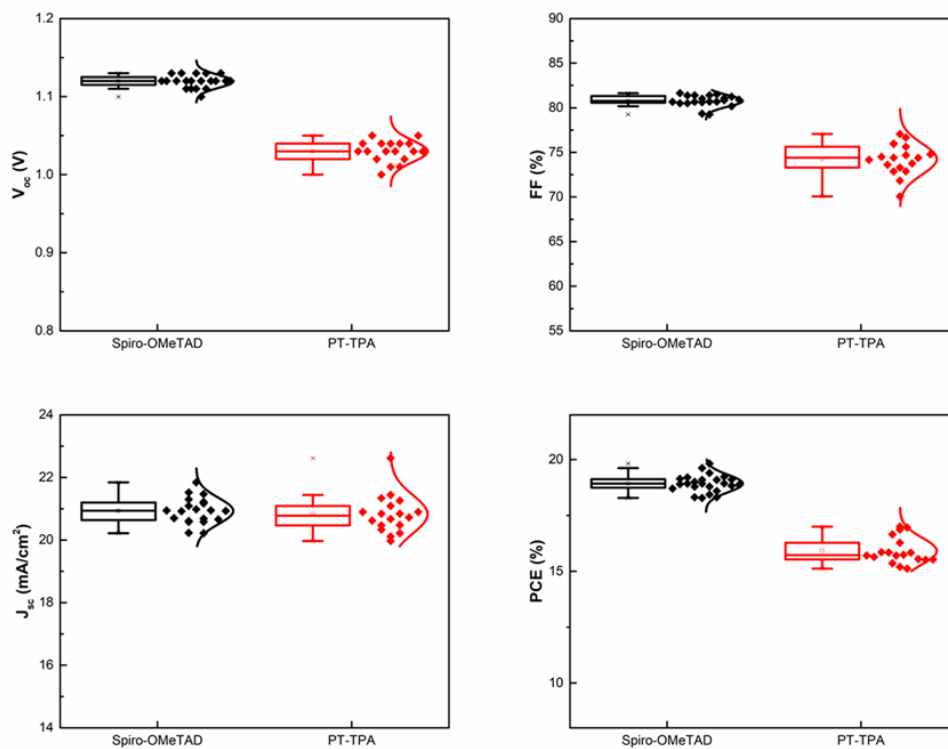
Figure 4-18. Box charts of the statistical data of PT-TPA-based devices recorded from different batches of synthesis.

The reverse-forward graph of the best Spiro-OMeTAD and PT-TPA coated cells is given in the Figure 4-19. Photovoltaic parameters are shown in the table Table 4-8.

Table 4-8. Photovoltaic parameters of cells including reverse and forward measurements of best devices of regular doped Spiro-OMeTAD (Reference) and PT-TPA

HTM		V_{oc} (V)	J_{sc} (mA/cm^2)	FF (%)	PCE (%)
Reference (Spiro)	Rev	1.12	21.84	81.03	19.82
	Forw.	1.10	21.88	60.04	14.45
PT-TPA	Rev	1.05	21.09	77.06	17.00
	Forw.	0.94	21.65	49.78	10.13
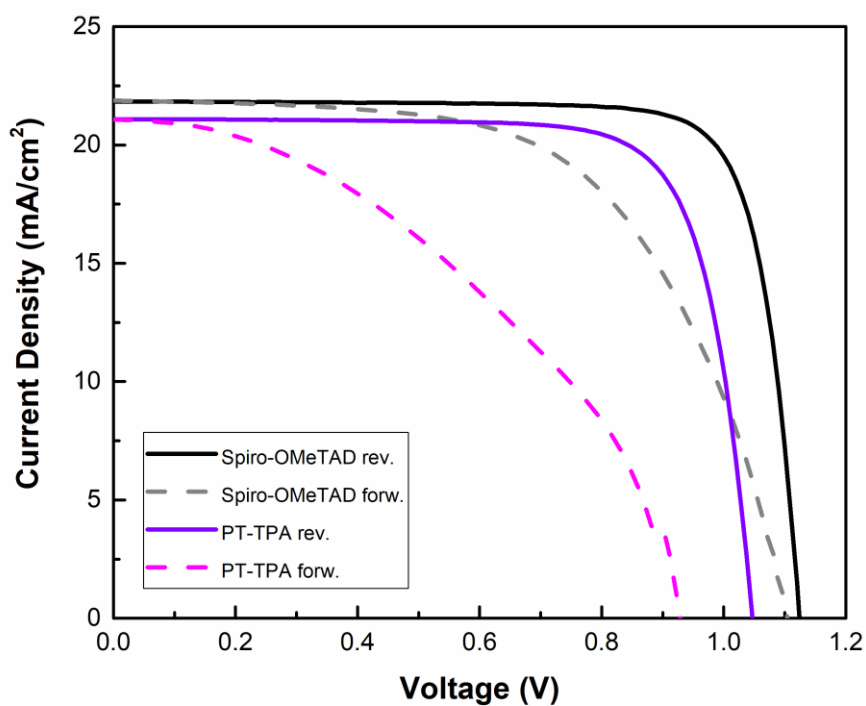
Figure 4-19. JV curves of reverse and forward measurements of best devices of regular doped Spiro-OMeTAD (Reference) and PT-TPA

4.2.4   Stability Tests of PT-TPA

Stability is one of the most critical factors for the development of perovskite solar cells as commercial products. Although Spiro-OMeTAD is appreciated in high-efficiency cell fabrications, it is a well-known fact that it is not an effective HTM in terms of cell stability. In order to compensate for the limited hole mobility of spiro-OMeTAD, it is necessary to use LiTFSI as a dopant, which is typically used in combination with tBP that both contribute to its solubility and improves the interfacial contacts, by taking into account the loss of stability[100]. It has been demonstrated that unoxidized Li^+ ions in the spiro-OMeTAD layer resulting from LiTFSI doping penetrate through the device into the perovskite layer. Li^+ can diffuse even more rapidly than the intrinsic perovskite ions due to its small size and strong diffusion tendency[101]. Another accepted stability problem for PSCs with doped spiro-OMeTAD HTLs is the hygroscopicity of LiTFSI[102,103]. For these reasons, stability studies were conducted to evaluate the performance of undoped PT-TPA as a hole transport layer.

To evaluate the stability of cells fabricated using PT-TPA, the cells were initially examined at ambient conditions, in the dark, at 85°C degrees. During the 5-hour tests, photovoltaic measurements of the cells were recorded, which are displayed in the Table 4-. The Figure 4-20 depicts the time-dependent PCE decrease of Spiro-OMeTAD-coated reference and PT-TPA HTM-coated cells.

Upon looking into the data, it was determined that the reference cell lost approximately 65% of its efficiency after one hour, whereas the PT-TPA-coated cell preserved 53.5% of its efficiency at the end of the five hours.

Table 4-9. Photovoltaic parameters of cells including ambient heat test
measurements of Spiro-OMeTAD and PT-TPA based cells

	Time	V_{oc} (V)	J_{sc} (mA/cm^2)	FF (%)	PCE (%)	SPO (%)
Spiro-OMeTAD	Start	1.13	21.18	72.89	17.44	100
	1 Hour	1.01	20.48	30.93	6.40	36.7
	3 Hours	1.12	9.00	0.37	0.04	-
	5 Hours	-	-	-	-	-
PT-TPA	Start	1.02	21.60	72.86	16.05	100
	1 Hour	0.97	21.47	52.30	10.89	67.9
	3 Hours	0.92	20.86	53.93	10.35	64.5
	5 Hours	0.90	20.73	46.03	8.59	53.5
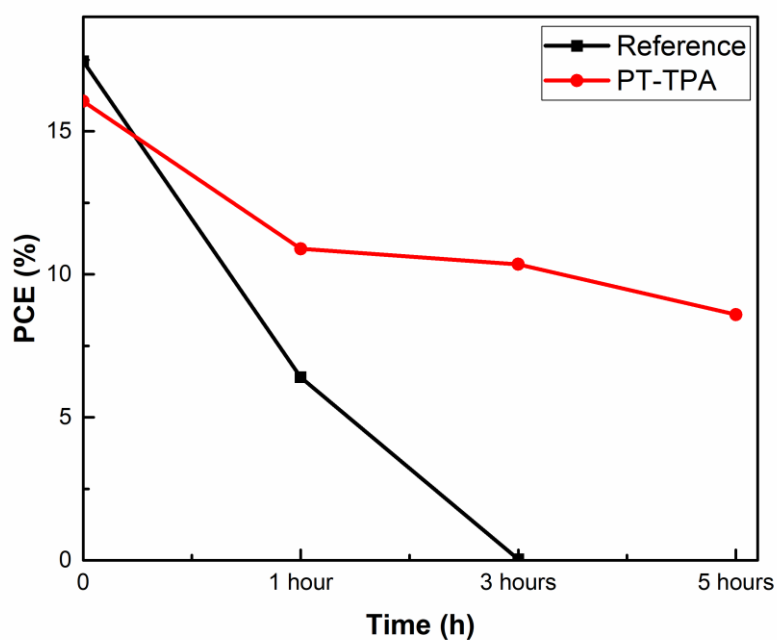
Figure 4-20. Time dependence of PCE(%) measurements of reference and PT-TPA
cells under heat treatment

The 85 °C test was also conducted within a glovebox to eliminate the impact of environmental factors. The tests proceeded until the end of the fifth day, as the glovebox-tested cells were more resilient. Throughout the temperature test, the cell efficiencies were monitored at regular intervals and are detailed in the Table 4-. The JV graphs of the reference and PT-TPA cells are derived from measurements performed at these time intervals and displayed in the Figure 4-21.

Table 4-10. Photovoltaic parameters of cells including glovebox heat test measurements of Spiro-OMeTAD and PT-TPA based cells

	Time	V_{oc} (V)	J_{sc} (mA/cm^2)	FF (%)	PCE (%)	SPO (%)
PT-TPA	Start	0.99	21.21	66.6	13.98	100
	1 Hour	0.98	20.71	66.59	13.52	96.7
	3 Hours	0.95	19.94	61.06	11.57	82.8
	5 Hours	0.93	20.34	58.05	10.98	78.5
	7 Hours	0.90	19.32	56.34	9.80	70.1
	24 Hours	0.90	20.41	50.68	9.31	66.6
	Day 5	0.83	18.05	49.02	7.35	52.6
Spiro-OMeTAD	Start	1.14	20.86	78.2	18.6	100
	1 Hour	1.04	17.11	61.44	10.94	58.8
	3 Hours	1.02	16.93	52.19	9.01	48.4
	5 Hours	1.04	17.15	53.89	9.61	51.7
	7 Hours	1.04	17.35	54.62	9.85	53.0
	24 Hours	1.04	17.02	53.79	9.52	51.2
	Day 5	0.14	1.98	47.62	0.13	-
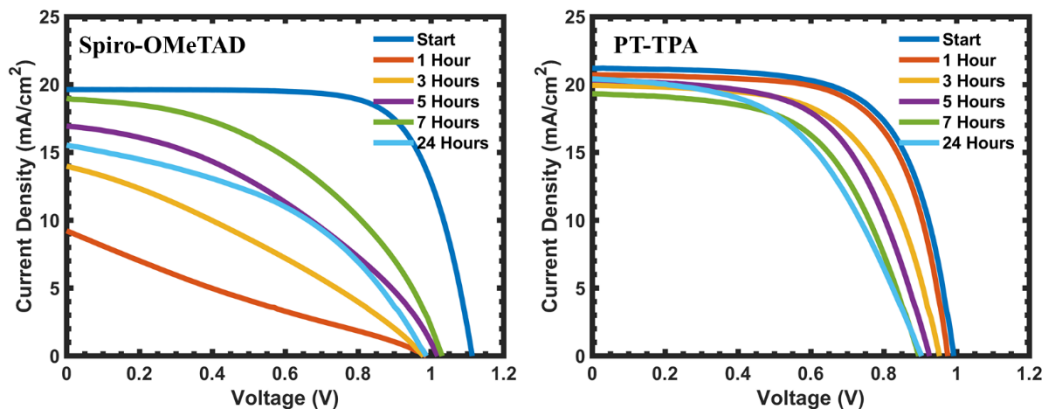
Figure 4-21. JV curves of reference and PT-TPA cells under heat treatment at glovebox

Observing the test results, it was discovered that the reference cell coated with Spiro-OMeTAD could only keep 58.8% of its efficiency after 1 hour, whereas the cell coated with PT-TPA kept 52.6% of its efficiency even after five days. According to the findings of the temperature testing, the PT-TPA HTL-produced cells exhibited much more excellent stability than the reference cells.

ITO/SnO$_2$/perovskite/Spiro-OMeTAD and ITO/SnO$_2$/perovskite/PT-TPA films were created and XRD measurements were conducted to investigate the heating test results further (Figure 4-22). In the heat-exposed Spiro-OMeTAD films, the intensity of the perovskite peak decreased while the intensity of the PbI$_2$ peak increased, as shown by XRD data. It is predicted that Spiro-OMeTAD-containing films will deteriorate, resulting in lower cell efficiencies.
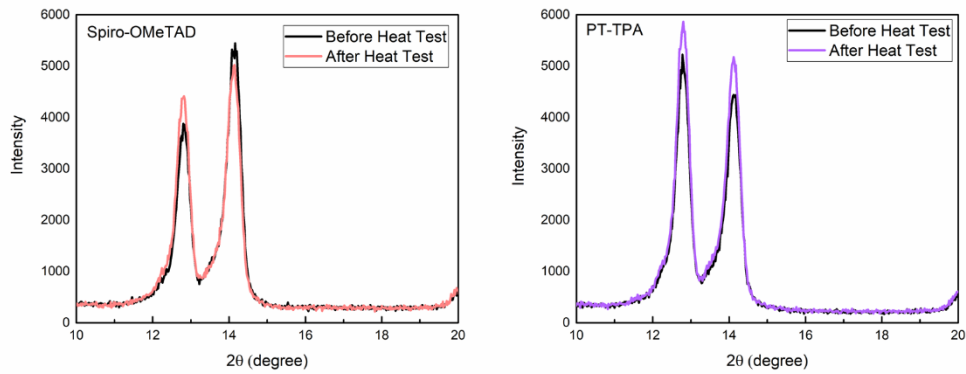
Figure 4-22. The XRD pattern of perovskite thin films with Spiro-OMeTAD and PT-TPA, before and after heat test

The photovoltaic performance of cells produced with Spiro-OMeTAD, as a reference and PT-TPA was monitored over a 70-day period at room temperature and 15% humidity (Figure 4-23). Cells prepared with Spiro-OMeTAD retained just 14.93% of their PCE% after 28 days, whilst there is no efficiency loss at PT-TPA-coated cells. At the end of 70 days, PT-TPA-coated cells maintained an efficiency of 96%, while Spiro-OMeTAD-coated cells were degraded.
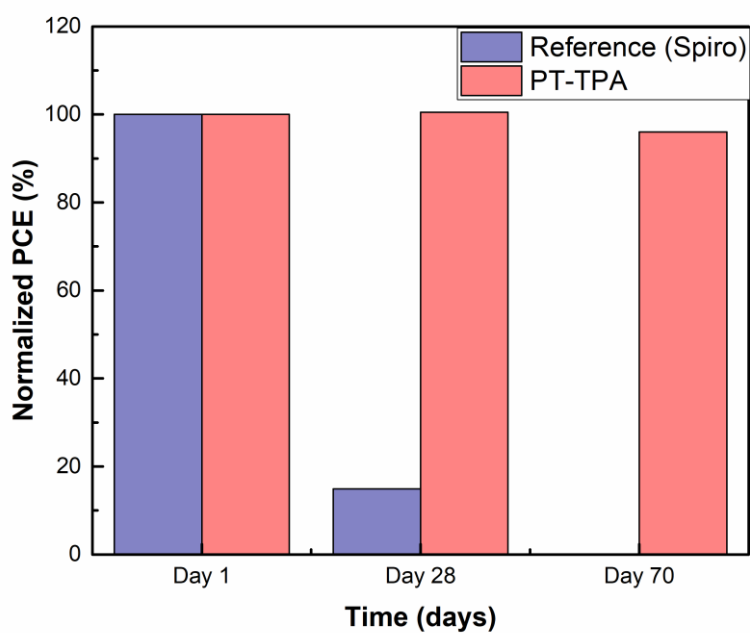
Figure 4-23. Time dependence of PCE(%) measurements of reference and PT-TPA cells at ambient conditions

Contact angle measurements were carried out since this remarkable stability performance could be attributed to the hydrophobic nature of PT-TPA. Considering the contact angle of PT-TPA-coated films, an angle of 92.04 degrees is measured. A hydrophobic surface was obtained with the PT-TPA material, positively affecting the stability of the cell (Figure 4-24).
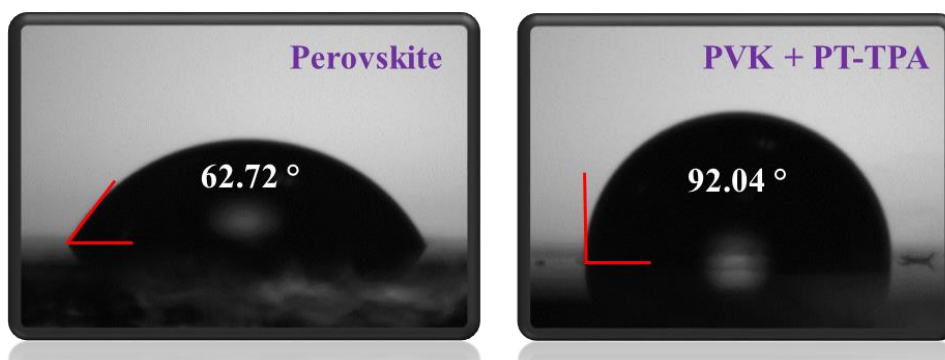
Figure 4-24. Contact angle images of perovskite and PT-TPA films

The J-V system was used to monitor maximum power point tracking (MPPT) for the light stability test. During the MPPT measurement, devices were set in ambient conditions (RH 20-40% and at room temperature) under continuous illumination of 1 sun. The cell efficiency, which started at 11.31% at the end of the 1800s, dropped to 10.15%. The stability of the PT-TPA-containing cell, which was studied under light for 1800s, was similarly quite good, with 86.5% efficiency saving detected after 1800 s (Figure 4-25).
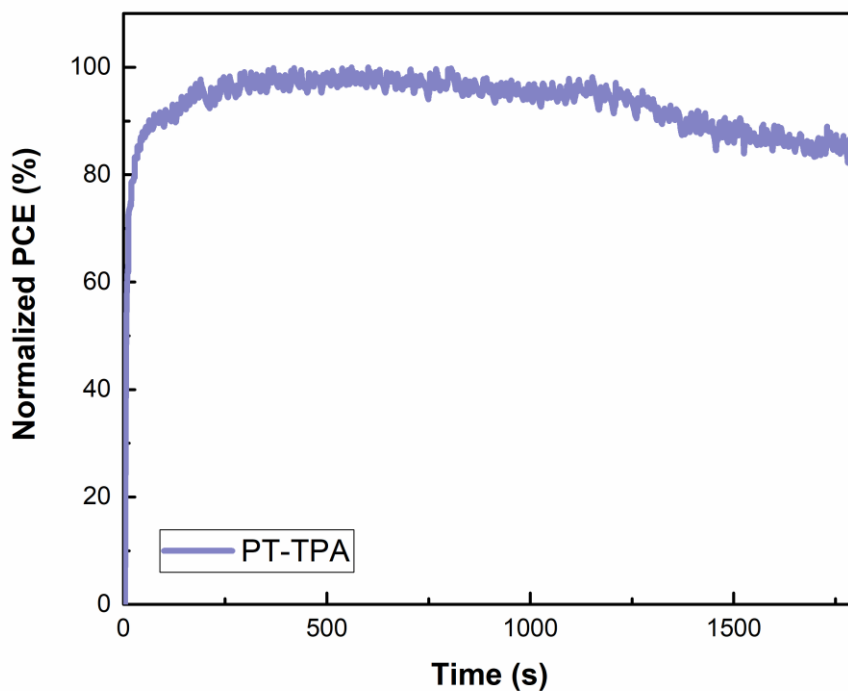
Figure 4-25. Time dependence of PCE(%) measurement of PT-TPA cell under light treatment

4.2.5 Encapsulation Tests

Encapsulation is essential in order to maintain the stable operation of solar cells in environmental conditions. For the encapsulation process, cells containing Spiro-OMeTAD and PT-TPA were laminated with Suryln material for 23 minutes at 100 °C. However, severe degradation occurred in the cells containing Spiro-OMeTAD due to the heat treatment, and the cell performance could not be measured. Consequently, JV measurements of the cell were not possible.

In PT-TPA solar cells, on the other hand, lamination was carried out successfully, and no performance degradation was observed in the 1-month measurement results.

Figure 4-26 depicts the JV measurement curves both before and after encapsulation. Table 4- displays the 1-month measurement parameters.
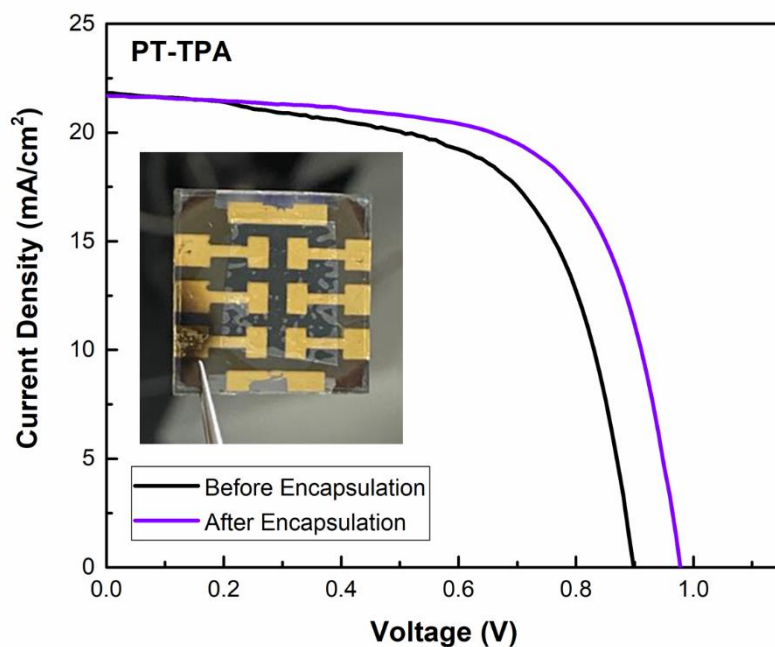
Figure 4-26. JV curves of PT-TPA cell before and after encapsulation

Table 4-11. Photovoltaic parameters of PT-TPA based cells with encapsulation

PT-TPA	V_{oc} (V)	J_{sc} (mA/cm^2)	FF (%)	PCE (%)
Before Enc	0.90	21.82	62.47	12.27
After Enc (Day 1)	0.98	21.70	65.84	14.00
After Enc (Day 13)	0.94	22.10	64.42	13.44
After Enc (Day 35)	0.92	22.79	62.77	13.16

Cells performance loss after heat treatment was reported in cells utilizing Spiro-OMeTAD as the hole transport layer due to deformation. It has been noted in the literature that the creation of voids in the Spiro-OMeTAD layer, and not the perovskite layer, is responsible for the high-temperature deformation[104,105]. The creation of voids is fundamentally linked to the release of doping components by spiro-OMeTAD at elevated temperatures. The size of the voids grew with the temperature beginning at 80 degrees, resulting in the cells' distortion. Another study claims that, even though spiro-OMeTAD has a melting point of 245 °C, even pristine Spiro-OMeTAD is prone to crystallization when subjected to 100 °C thermal stress, which disrupts interface contact [106]. The presence of p-dopants makes thermal stability poorer and was shown to reduce the stability of the amorphous Spiro-OMeTAD phase because the oxidized form of the material has a lower glass transition temperature[107]. The efficiency of PSCs including doped spiro-OMeTAD HTLs decreases fast at temperatures as low as 85 °C, although the vast majority of perovskites and other PSC components are thermally durable in this temperature range[108].

4.3   Outlook of the Chapter

HTMs are employed to transport positive charges (holes) from the perovskite light-absorbing layer to the electrode in perovskite solar cells. As mentioned before, traditional HTMs used in perovskite solar cells are often based on organic materials, such as Spiro-OMeTAD, that contain electron-withdrawing dopants, such as Li-TFSI and tbP. However, these dopants can cause instability issues and lower the efficiency of solar cells. There has been growing interest in recently creating dopant-free HTMs as an alternative to traditional HTMs.

TPA-based hole transport materials (HTMs) are a promising alternative to traditional HTMs in perovskite solar cells due to their excellent hole transport properties and

improved stability. They can improve the long-term stability of the perovskite material since TPA-based materials are more resistant to thermal and light-induced degradation, reducing the risk of performance degradation over time.

As a TPA-based hole transport material, PT-TPA has also shown high success in long-term stability. With the effect of being a dopant-free HTL, no efficiency loss was observed under heat and light treatment.

However, it should be noted that the performance of PT-TPA can still be further optimized, particularly regarding the compatibility with other device components like the perovskite layer.

CHAPTER 5

NOVEL P-TYPE DOPANT for HOLE TRANSPORT LAYER

The vast majority of p-type semiconductors used in HTLs have inherently insufficient conductivity and low hole mobility. As indicated, the hole mobility for undoped spiro-OMeTAD is about $10^{-5} - 10^{-7}$ cm^2 V^{-1}s^{-1}, which is insufficient to extract photogenerated holes from the perovskite layer and inhibit non-radioactive charge recombination.

Thus, the HOMO levels of pristine undoped organic HTMs are frequently high (4.9 to 5.1 eV), generating an energy gap between the HOMO levels of perovskites (5.4 to 5.6 eV), resulting in a barrier for hole transport and loss at open-circuit voltage.

Commonly, additive engineering is used to improve the electrical properties of HTMs and develop HTMs for n–i–p PSCs in terms of hole mobility and energy level alignment in order to avoid these limitations.

P-type dopants are impurities introduced to the bulk matrix of HTMs to modify their electronic status and semiconductor properties; p-doping approach for HTMs (mainly for organic HTMs) are often employed to boost the PCE of n–i–p devices by improving hole extraction and transport. The roles of p-type dopants in HTLs for PSCs are as follows; a) enhance the hole concentration of HTM, resulting in several times higher hole mobility than the undoped one, b) decrease the HOMO level of HTM toward the valence band of perovskites which expedite hole transport from perovskite layers to HTLs.

The doping process occurs indirectly and it is non-quantitative. There is a complex reaction pathway involving a two-step redox process where the oxidation of spiro-OMeTAD is promoted by Li-TFSI, as shown in eqn (1) and (2).

This reaction is slow and environment dependent, which often takes one night or even longer and is susceptible to water, oxygen, and light.

In the initial oxidation of spiro-OMeTAD by dioxygen, oxygen radicals could form. Subsequently, these oxygen radicals are removed by Li-TFSI. The remaining Li^+ cation forms a Li_xO_y species, and the TFSI anion traps/stabilizes the oxidized spiro-OMeTAD (spiro-OMeTAD$^{\bullet+}$).

$$\text{Spiro-OMeTAD} + O_2 \leftrightarrow \text{Spiro-OMeTAD}^{\bullet+}O_2^{\bullet-} \qquad (1)$$

$$\text{Spiro-OMeTAD}^{\bullet+}O_2^{\bullet-} + \text{Li-TFSI} \leftrightarrow \text{Spiro-OMeTAD}^{\bullet+}\text{TFSI}^- + Li_xO_y \qquad (2)$$

LiTFSI tends to absorb water from air and aggregate in the spiro-OMeTAD film, affecting the interfacial energy level, adhesion, and morphology. Moreover, Li^+ ions in the spiro- OMeTAD layer can migrate across the perovskite layer and accumulate in the ETL, which has an impact on the efficiency, hysteresis, and degradation of PSCs. The factors above fail to meet the performance and stability demands of commercial PSCs.
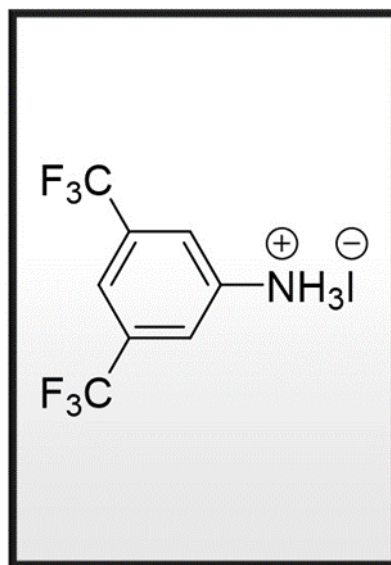
Figure 5-1. Schematic of chemical structure of 3,5-Bistrifluoromethyl-
Phenylammonium iodide (CFF)

5.1   Results and Discussions

This chapter includes the incorporation of a novel p-type dopant, CFF, into perovskite solar cells by doping spiro-OMeTAD. In this context, concentration, spin rate optimization was performed, and cell efficiencies and stability was evaluated in detail.

Standard doped HTM (spiro-OMeTAD with LiTFSI), the undoped HTM (spiro-OMeTAD with no additives) and novel dopant utilized HTM (spiro-OMeTAD with CFF) were prepared to compare the film characteristics. The standard doped HTM solution was prepared by dissolving 72.3 mg of Spiro-OMeTAD in 1 mL chlorobenzene followed by addition 28.8 μL of 4-tert-butylpyridine (tBP) and 17.5 μL from a stock solution of 520 mg/mL of lithium bis(trifluoromethylsulphonyl)imide (Li-TFSI) in acetonitrile (ACN).   The CFF solution was prepared by dissolving 30 mg CFF in 1 mL ACN. For undoped HTM; the spiro was dissolved in CB and stored in the glovebox. Standard doped spiro-OMeTAD was kept in glovebox for 2-3 h before spin coating and CFF doped spiro-

OMeTAD was kept in glovebox for 10-15 min before spin coating. The image of the solution doped with CFF is given in the Figure 5-2.
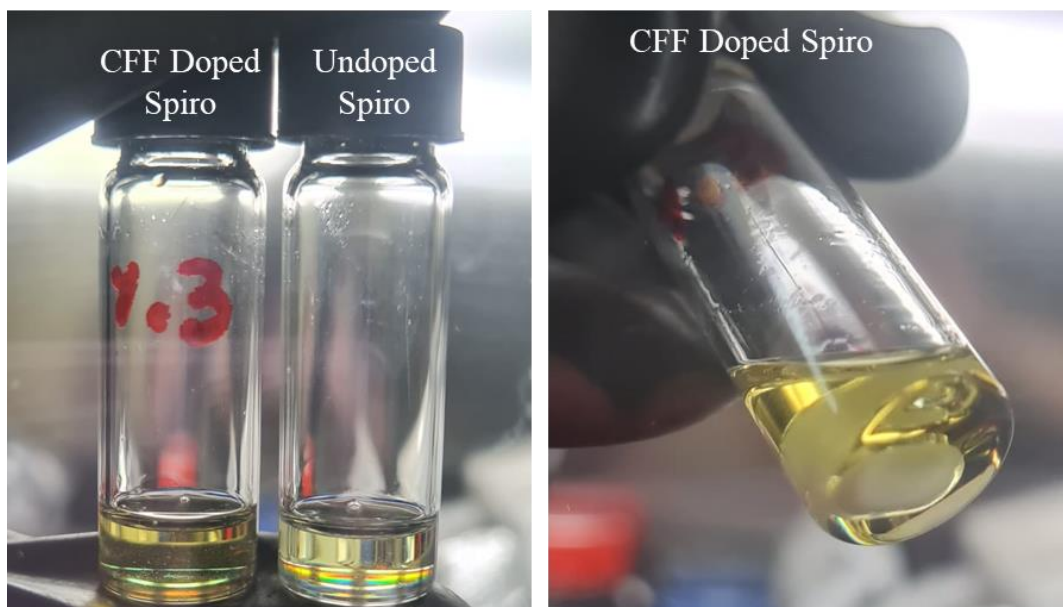
Figure 5-2. Photos of 3% CFF-doped and undoped-spiro solutions.

5.1.1 Concentration Optimization

As a first study, spiro-OMeTAD was doped with 1.0, 2.5, 5.0 and 7.5% CFF solution to optimize the amount of dopant used. The highest efficiency was obtained as 15.37 % with 2.5% CFF doped device. The short circuit current density (J_{sc}) value of the cell was measured as 21.25 mA/cm^2, the open circuit voltage (V_{oc}) was 1.08 V, and the fill factor (FF%) value was 66.97. Looking at the mean values, the values of 13.19%, 14.26%, 14.38%, and 12.99% were measured for 1.0, 2.5, 5.0 and 7.5% CFF doped devices, respectively (

Table 5-1). As a result of the average values, 2.5% CFF doping concentration was chosen as the optimum. JV curves of best devices with the doping concentrations of 1.0, 2.5, 5.0 and 7.5% CFF were given at Figure 5-3.

116

Table 5-1. Photovoltaic parameters of different concentrations between 1.0% and 7.5% of CFF in HTM

HTM		V_{oc} (V)	J_{sc} (mA/cm^2)	FF (%)	PCE (%)
Undoped	Average	0.72	14.43	28.20	2.89
Spiro-OMeTAD	Highest	0.91	18.17	27.59	4.56
1.0% CFF Doped	Average	1.07	20.80	59.13	13.19
	Highest	1.07	21.47	63.34	14.56
2.5% CFF Doped	Average	1.08	20.18	65.52	14.26
	Highest	1.08	21.25	66.97	15.37
5.0% CFF Doped	Average	1.07	20.90	64.32	14.38
	Highest	1.08	21.3	65.07	14.97
7.5% CFF Doped	Average	1.06	20.53	59.40	12.99
	Highest	1.07	21.62	62.37	14.43
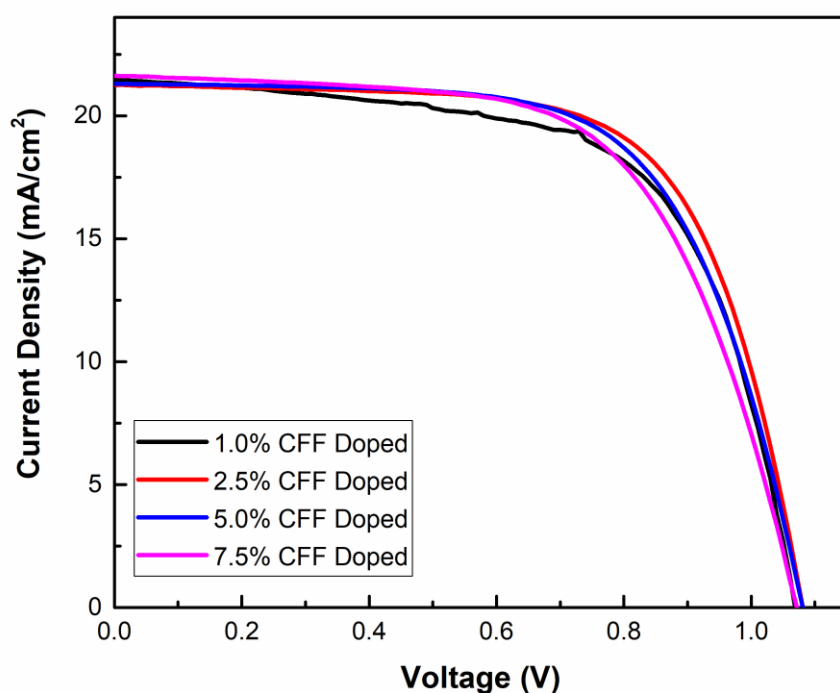
Figure 5-3. JV curve of different concentrations between 1.0% and 7.5% of CFF in HTM

Next, a more comprehensive concentration analysis was conducted. The highest efficiency was obtained as 17.77 % with 3% CFF doped device. The short circuit current density (J_{sc}) value of the cell was measured as 23.23 mA/cm^2, the open circuit voltage (V_{oc}) was 1.09 V, and the fill factor (FF%) value was 70.16. Looking at the mean values, the values of 15.88%, 15.57%, 15.23%, and 13.74% were measured for 3, 4, 5, and 6% CFF doped devices, respectively (Table 5-2). As a result of the average values, 3% CFF doping concentration was chosen as the optimum concentration. JV curves of best devices with the doping concentrations of 3, 4, 5, and 6% CFF weren given at Figure 5-3.

Table 5-2. Photovoltaic parameters of different concentrations between 3% and 6% of CFF in HTM

HTM		V_{oc} (V)	J_{sc} (mA/cm^2)	FF (%)	PCE (%)
3% CFF Doped	Average	1.09	21.74	66.79	15.88
	Highest	1.09	23.23	70.16	17.77
4% CFF Doped	Average	1.10	21.62	65.42	15.57
	Highest	1.11	23.09	67.50	17.30
5% CFF Doped	Average	1.10	21.56	64.28	15.23
	Highest	1.11	22.24	69.87	17.25
6% CFF Doped	Average	1.08	21.70	58.45	13.74
	Highest	1.09	22.04	63.19	15.18
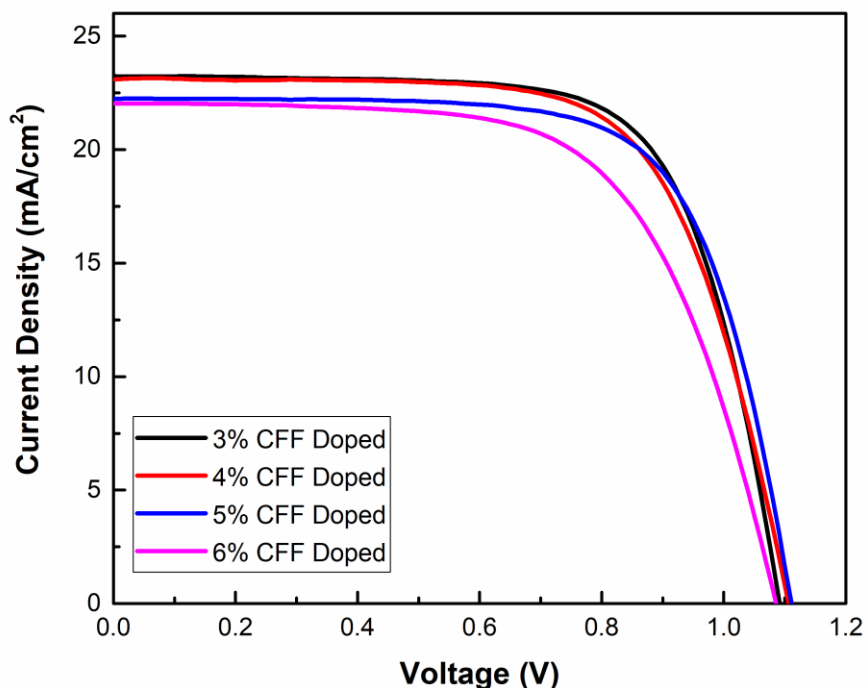
Figure 5-4. JV curve of different concentrations between 3% and 6% of CFF in HTM

5.1.2 Spin-Rate Optimization

In the final stage of the optimization, films with different spin speeds were prepared in order to optimize the thickness of the film further. Since the regular spiro-OMeTAD solution was coated at 3000 rpm, the spin speed range of the CFF-doped films was selected between 2000 rpm and 5000 rpm.

The highest efficiency was obtained as 16.77 % with 3000 rpm. The short circuit current density (J_{sc}) value of the cell was measured as 22.11 mA/cm^2, the open circuit voltage (V_{oc}) was 1.10 V, and the fill factor (FF%) value was 68.91. Looking at the mean values, the values of 14.89%, 15.64%, 15.18%, and 14.87% were measured for CFF doped devices with a spin rates at 2000, 3000, 4000 and 5000 rpm, respectively (Table 5-3). As a result of the average values, **3**000 rpm spin rate was

chosen as the optimum. JV curves of best devices with the differen spin rates are given at Figure 5-4.

Table 5-3. Photovoltaic parameters of different spin rates of CFF doped HTM between 2000 and 5000 rpm

HTM		V_{oc} (V)	J_{sc} (mA/cm^2)	FF (%)	PCE (%)
Regular doped Spiro-OMeTAD (Spiro Reference)	Average	1.07	21.53	76.48	17.69
	Highest	1.10	22.94	74.73	18.86
2000 rpm CFF Doped	Average	1.09	22.06	62.04	14.89
	Highest	1.10	23.12	62.51	15.90
3000 rpm CFF Doped	Average	1.09	21.65	65.99	15.64
	Highest	1.10	22.11	68.91	16.77
4000 rpm CFF Doped	Average	1.10	21.57	64.21	15.18
	Highest	1.10	22.39	66.02	16.26
5000 rpm CFF Doped	Average	1.08	21.56	63.73	14.87
	Highest	1.09	23.14	63.97	16.14
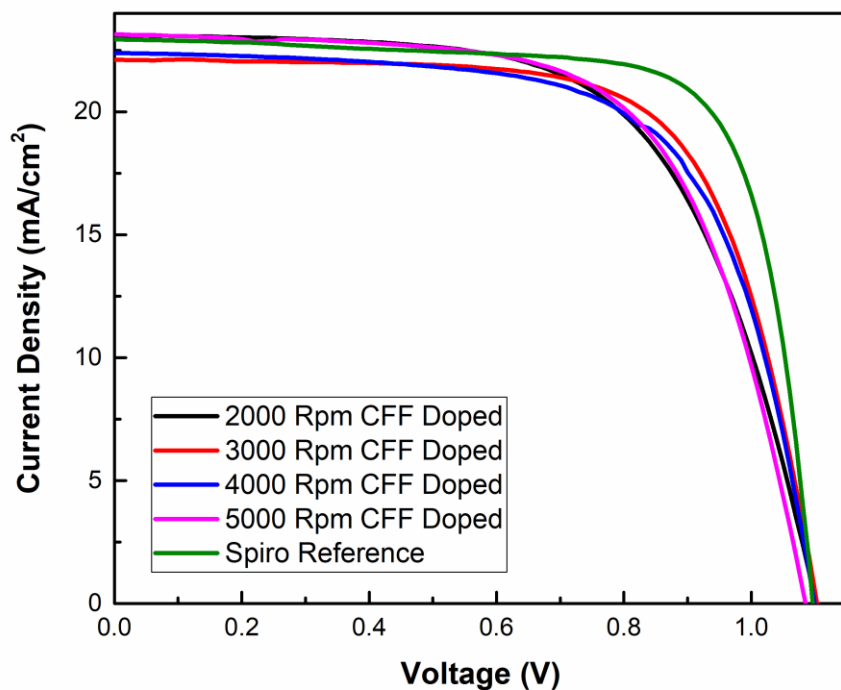
Figure 5-5. JV curves of reference and CFF-doped HTMS with different spin speeds between 2000 and 5000 rpm

The optimal coating rate and rotation speed for the CFF-doped hole transport solution, according to the optimization studies, were determined to be 3% and 3000 rpm, respectively.

Table 5-4. Photovoltaic parameters of best devices of reference and CFF-Doped cells

HTM		V_{oc} (V)	J_{sc} (mA/cm^2)	FF (%)	PCE (%)
Reference Spiro-OMeTAD	Reverse	1.10	22.94	74.73	18.86
	Forward	1.08	23.00	70.08	17.41
3% CFF Doped Spiro-OMeTAD	Reverse	1.09	23.23	70.16	17.77
	Forward	1.02	23.25	61.40	14.56

When the best efficient cell obtained with CFF-doped solution with these ratios is compared with the cell containing regular doped Spiro-OMeTAD, and it was observed that comparable performance were achieved. Photovoltaic parameters of the cells are given in Table 5-4. The JV curve of reverse and forward measurements of cells can be seen in Figure 5-6.
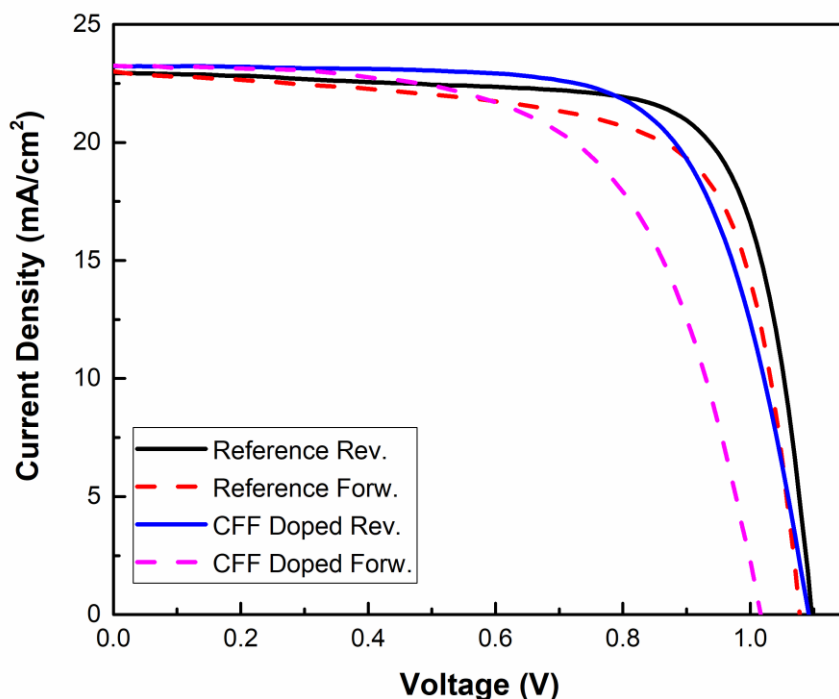
Figure 5-6. JV curves of reverse and forward measurements of reference and CFF-doped champion devices

Perovskites exhibit strong light emission intensity due to the radiative recombination of photogenerated electrons and holes[109]. Commonly, when coated with HTMs, a significant decrease in the emission signals was observed due to extraction of holes. When PL intensities of standard and CFF doped spiro-OMeTAD are compared, the PL intensity of standard doped Spiro-OMETAD film is relatively low according to CFF doped films indicating highly efficient hole transport efficiencies between the perovskite films and the HTMs (Figure 5-7). Although the film doped with 3% CFF has a lower density than other ratios, the fact that it is pretty high compared to the regular doped spiro film indicates that there is no effective hole transport.
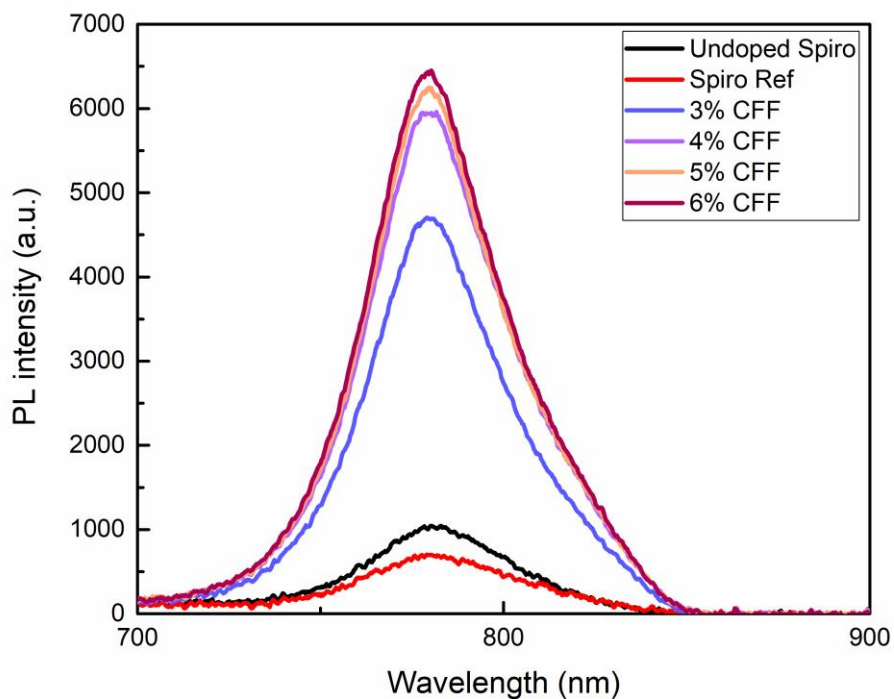
Figure 5-7. PL spectra of ITO/SnO$_2$/FAMA Perovskite covered by doped- and undoped- Spiro-OMeTAD samples at an excitation wavelength of 530 nm.

In order to confirm that CFF is an appropriate p-type dopant for Spiro-OMeTAD, the conductivities of pristine, regular and CFF-doped Spiro-OMeTAD with different concentrations were investigated. Increasing trend of conductivity of the Spiro-OMeTAD film at different doping ratios of CFF dopant is given in Figure 5-8.
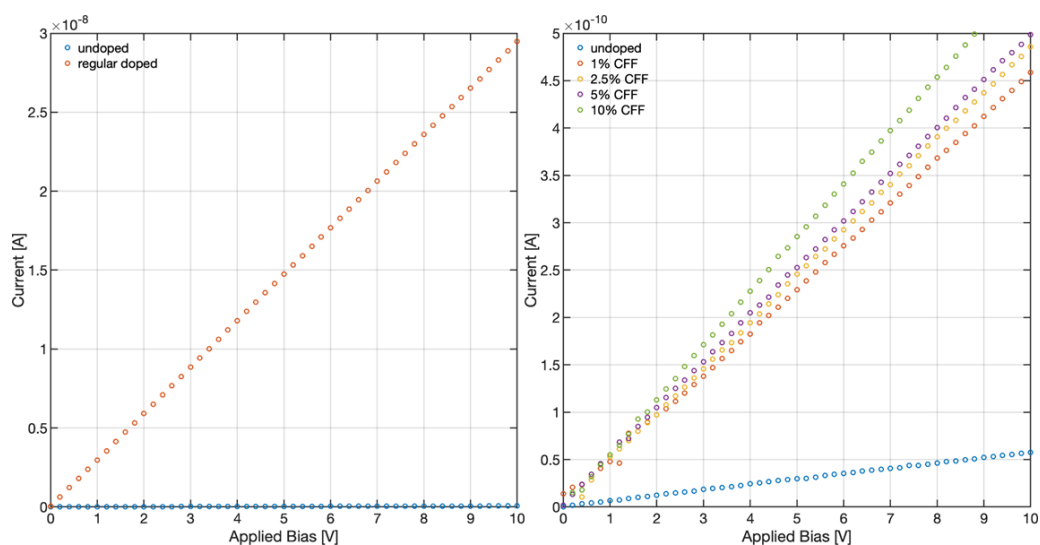
Figure 5-8. Current−voltage plot with the structure of ITO/doped- and un-doped spiro-OMeTAD/Au.

HTM	Conductivity (S·cm^{-1})
Undoped Spiro	1.55e^{-8}
1% CFF Doped	1.23e^{-7}
2.5% CFF Doped	1.33e^{-7}
5% CFF Doped	1.35e^{-7}
10% CFF Doped	1.55e^{-7}
Regular Doped Spiro	8.03e^{-6}

The film conductivity of spiro-OMeTAD is enhanced after CFF doping which was calculated by testing hole-only diodes with top Au electrodes. For CFF dopant-based HTLs, the conductivity was improved an order of magnitude, with the highest conductivity of 1.55×10^{-7} S·cm^{-1} was achieved 10% CFF doping. In the literature, there are studies showing a successful doping example with an increase in conductivity at similar magnitudes[110,111]. CFF doping increases the hole mobility of spiro-OMeTAD, which contributes to the effective transport and extraction of holes

125

in solar cells. It is clear that the doping intensity was quite lower compared to Li based doping of spiro-OMeTAD. However, apparently from device performance data the level of doping achieved with LiTFSI is not required for high performance and is the main reason for the instability observed in these devices. Studies related to stability of devices with different dopants was investigated in details and results are summarized in next section.

5.1.3 Stability

As mentioned in the sections above, the Spiro-OMeTAD stability problem issues stands as an important problem on the way to the commercialization and development of perovskite solar cells. Since the efficiency of cells produced with undoped Spiro is very low, Spiro-OMeTAD hole transport material is used together with Li-TFSI and tBP dopants to produce highly efficient solar cells. These dopants very negatively affect the stability of cells produced with Spiro-OMeTAD. In order to solve this problem, We have achieved very high comparable efficiencies with the CFF as a doping material we introduced. Even in terms of stability, CFF-doped cells are quite ahead of regular-doped Spiro-OMeTAD and here we investigated the effect on stability in resulting PSCs. Devices prepared with both CFF and LiTFSI were measured as they are fabricated and kept in ambient conditions (room temperature and 15% moisture).

Table 5-5. Photovoltaic parameters of fresh and aged devices of reference and CFF-doped

		V_{oc} (V)	J_{sc} (mA/cm^2)	FF (%)	PCE (%)	SPO (%)
Regular Doped Spiro (Reference)	Fresh	1.14	20.99	79.70	19.07	100
	Day 20	1.00	18.89	29.41	5.57	29.2
	Day 60	-	-	-	-	
	Day 90	-	-	-	-	
CFF Doped Spiro	Fresh	1.02	19.81	77.07	15.58	100
	Day 20	1.05	20.25	76.63	16.23	104.2
	Day 60	1.05	20.10	69.89	14.69	94.3
	Day 90	1.04	19.91	65.19	13.50	86.6

Looking at the measurement results given in detail in Table 5-5, it is seen that; While the reference cells lost about 70% of its efficiency at the end of 20 days, no results were obtained in the 60 and 90 day measurements. While no efficiency loss was observed at the end of 20 days with CFF-doped cell, it was observed that 86.6% of the cell efficiency was kept at the end of 90 days. The bar graph where you can see the time dependent cell efficiencies comparatively is given in Figure 5-9.
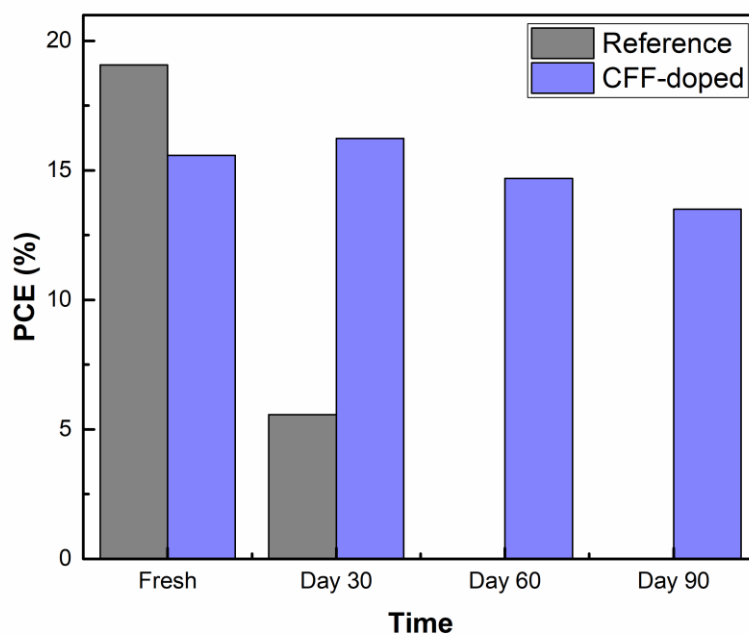
Figure 5-9. Bar graphs of best devices of aged and fresh reference and CFF-doped devices

Contact angle measurements were carried out to inspect the surface of the film. As a consequence of these studies, it was determined that CFF-doped films were slightly higher than undoped Spiro and the regular-doped Spiro. This shows that the surface of CFF-doped films is more hydrophobic. Contact angle images are given at Figure 5-10.
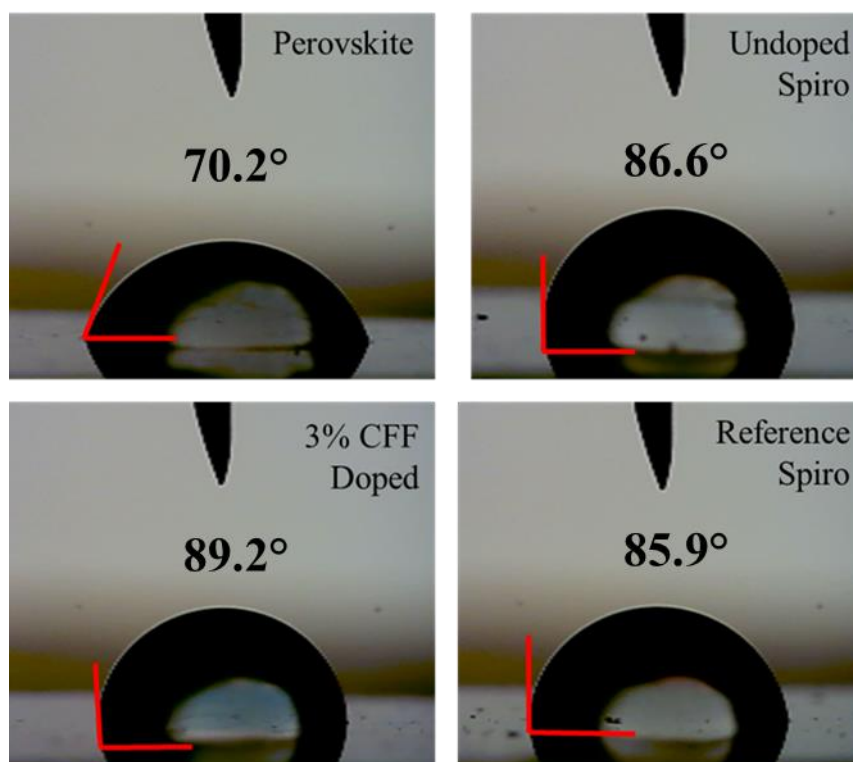
Figure 5-10. Contact angle images of perovskite, undoped Spiro, reference Spiro and 3%CFF-doped Spiro

5.2 Outlook of the Chapter

In this part of the thesis, a novel p-type dopant, CFF, was introduced with promising results. While CFF-doped devices were highly efficient as regular doped devices, they were also as stable as undoped devices. As a result of conductivity data, it is observed that CFF material doped Spiro-OMeTAD less than regular dopants. However, it is enough to improve the hole transport properties of Spiro-OMeTAD material. As a result, it can be claimed that there is no need for regular dopants to get highly efficient solar cells. Additionally, CFF dopant material optimization studies will continue regarding solution concentration and film thickness for further improvement. Also, more appropriate perovskite structures will be tried to improve cell efficiency. Lastly, more conductive alternatives of the CFF molecule will be synthesized and integrated into HTM for the doping process to observe the development.

CHAPTER 6

LARGE CATION BASED 2D PASSIVATION of 3D PEROVSKITE

The passivation of perovskite layers has become increasingly important in the field of photovoltaic research. The need for passivation arises from surface defects that creates an environment for the electron-hole recombination, thus decreasing the efficiency of the solar cells. Passivation can increase the efficiency of solar cells by reducing the number of defects that can lead to recombination occurring at the interface between the active layer and the hole-transporting material.

Surface passivation involves applying a thin layer of passivating molecules to the surface of a perovskite film, which modifies the defect centers. This technique has been successfully implemented and demonstrated to improve the efficiency and lifetime of perovskite-based solar cells. Structural deformities such as grain boundary defects or crystallographic defects are observed during the formation of solution-processed perovskite films. In any solar cell, the passivation of the surface defects is always the most crucial task since deficiencies (in other words presence of dangling bonds) are often generated on the surface[112,113]. It is known that the recombination of defects in the bulk or on the surface of the perovskite absorber layer strongly impacts the V_{oc} of the solar cells[112,114–116].

Among different materials used for surface passivation of perovskite films, organic ammonium halide salts have shown promising results[117–119]. Ammonium cations in organic halide salts passivate negatively charged defects on the surface by electrostatic interactions such as ionic and hydrogen bonding.

Phenylmethylammonium iodide (PMAI) salts can passivate the perovskite material, thereby increasing its photovoltaic efficiency. PMAI salts can be used in perovskite solar cells to improve their performance by reducing surface defects, creating an efficient and stable planar structure and scavenging deep-level traps[120]. Passivation of the perovskite material using PMAI salts involves introducing the PMAI layer on

the perovskite material to form a stable interface between the perovskite material and the hole transport layer. This layer helps to reduce the rate of charge recombination, increasing the cell's overall stability. The ammonium cation in PMAI helps to passivate the charged traps at the surface of perovskite films, whilst the hydrophobic aromatic phenyl group helps to improve environmental stability by covering perovskite layer[121]. As a result, nonradiative charge recombination is minimized, and the open-circuit voltage (V_{oc}) of perovskite solar cells is increased[122,123]. In this part of the thesis, 3 novel PMAI based ammonium cations have been utilized for passivation perovskite solar cells and improved performance compared to that of unpassivated cells, with an increase in V_{oc}, efficiency and stability was demonstrated.

Phenylmethylammonium iodide (PMAI) salts linked to different aromatic functional groups ((4-(thiophene-2-yl)phenyl)methanaminium iodide, (4-(selenophene-2-yl)phenyl)methanaminium iodide and (4-(furan-2-) yl)phenyl)methanaminium iodide) were synthesized, and the effects of these salts on cell performance and the stability of cells were investigated by various characterization methods. Salts are indicated by the abbreviations TPMAI, SPMAI, and FPMAI, respectively (Figure 6-1a). Perovskite solar cells were fabricated in the n-i-p configuration with the structure of Glass/FTO/c-TiO$_2$/m-TiO$_2$/SnO$_2$/Perovskite/PMAI-based salts/Spiro-OMeTAD/Au (Figure 6-1b).
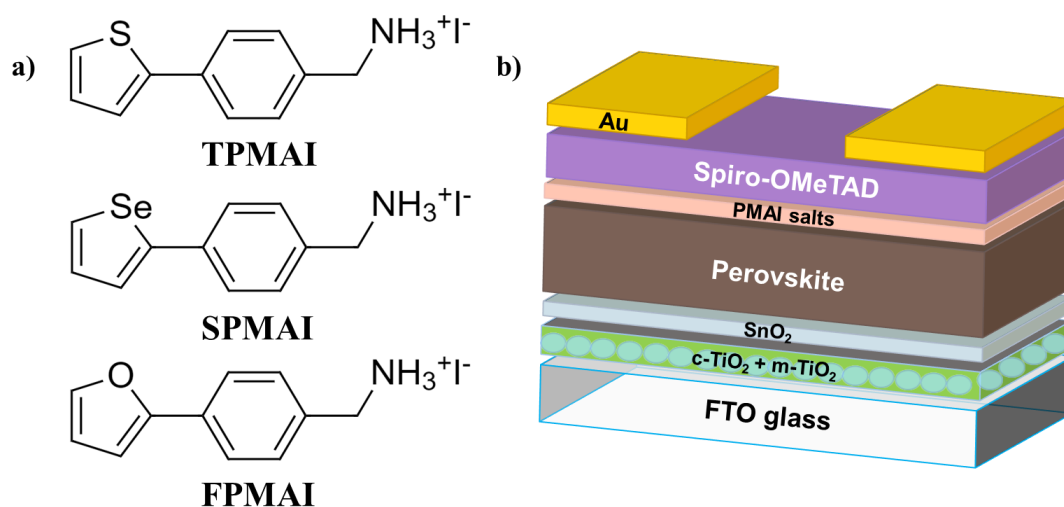
Figure 6-1. a) Molecular structures of TPMAI, SPMAI and FPMAI salts b) Schematic of the device structure

6.1 Preliminary Studies

The preliminary studies of the organic ammonium salts presented in this chapter were conducted in the ODTU-GUNAM laboratory, and highly encouraging results were obtained with the (4-(thiophen-2-yl)phenyl)methanaminium iodide (TPMAI) salt.

First the concentration optimization was conducted. The average and highest device parameters were listed in the Table 6-1 below. The highest average PCE was obtained with 5 mg/mL TPMAI as 21.24% with J_{sc} at 24.1 mA/cm^2. EQE measurements revealed an integrated J_{sc} of 22.8 mA/cm^2 which is within the acceptable 5% difference range. Increasing the concentration even further (6 mg/mL TPMAI) led to a decrease in average PCE due to lower FF. Independent of the concentration a noticeable enhancement was achieved in V_{oc}. Detailed cell measurements can be found in the box charts in Figure 6-2.

Table 6-1. Photovoltaic parameters of reference, 3 mg/mL, 4 mg/mL, 5 mg/mL, and 6 mg/mL TPMAI cells

HTM		V_{oc} (V)	J_{sc} (mA/cm^2)	FF (%)	PCE (%)
Spiro Reference	Average	1.10	22.19	81.34	19.78
	Highest	1.09	22.67	82.78	20.46
3 mg/mL TPMAI	Average	1.14	22.50	80.21	20.63
	Highest	1.14	22.48	81.76	21.33
4 mg/mL TPMAI	Average	1.15	21.68	80.84	20.12
	Highest	1.15	22.75	80.98	21.19
5 mg/mL TPMAI	Average	1.16	23.00	79.75	21.24
	Highest	1.16	24.15	80.06	22.43
6 mg/mL TPMAI	Average	1.15	23.01	75.00	19.86
	Highest	1.16	22.45	77.13	20.09

For the reference device highest PCE was 20.46% with a J_{sc} of 22.67 mA/cm^2, and its integrated J_{sc} was calculated as 21.65 mA/cm^2 from the EQE measurements.
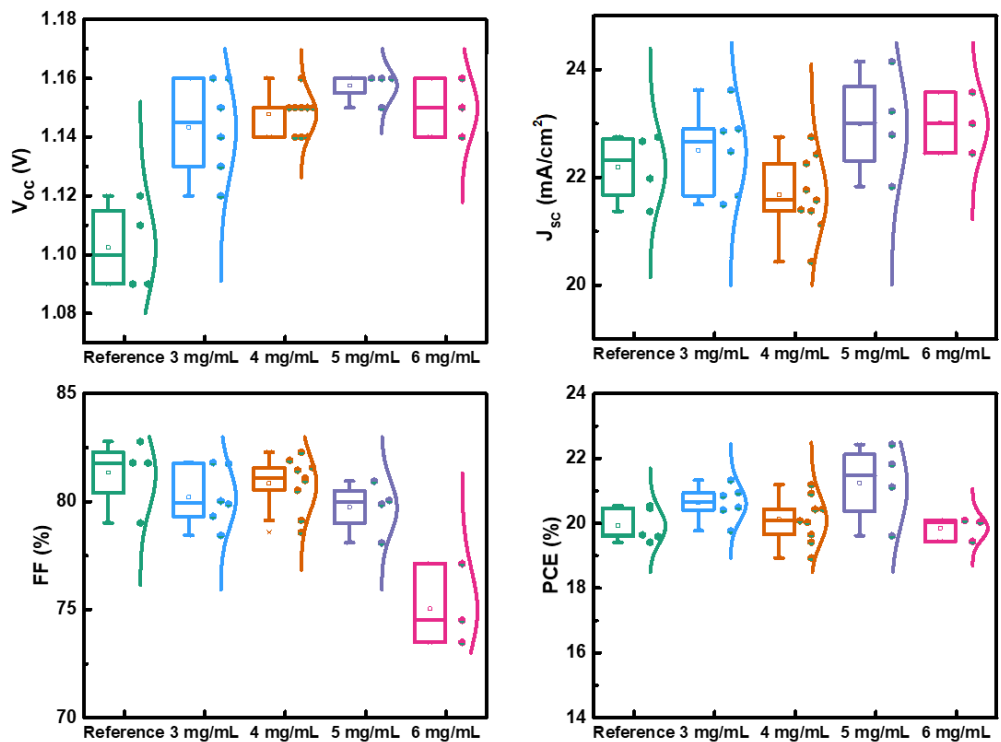
Figure 6-2. Box charts of reference, 3 mg/mL, 4 mg/mL, 5 mg/mL, and 6 mg/mL TPMAI cells
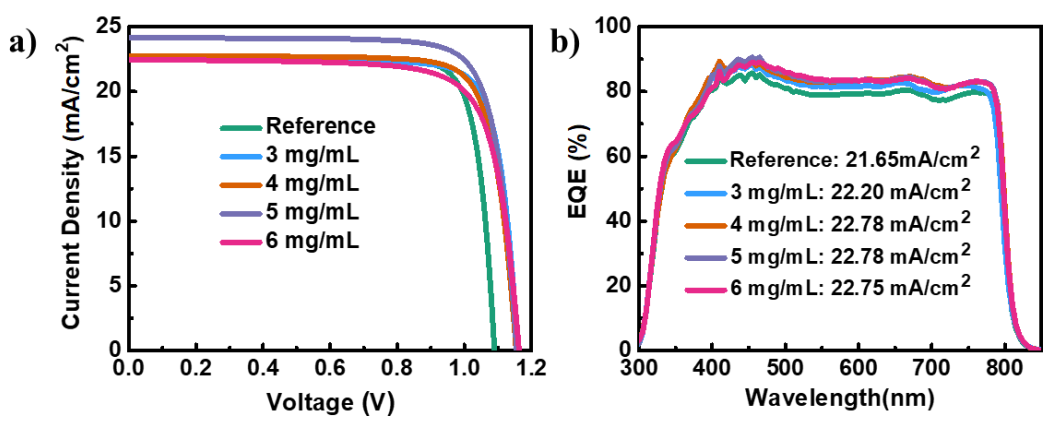
Figure 6-3. a) JV curves and b) EQE spectra of the reference and TPMAI, SPMAI and FMAI champion devices and calculated photocurrent values

TPMAI has shown to have significant potential as a passivation material which enabled cells with efficiencies exceeding 22%. FPMAI and SPMAI salts, which are derivatives of TPMAI, were synthesized after these initial promising results and further studies as a set were conducted with a collaboration with Prof. Nazeeruddin's group at EPFL.

6.2   Results and Discussion

Firstly, X-ray diffraction (XRD) analysis was performed to demonstrate whether these salts resulted in formation of a 2D perovskite layer on the 3D perovskite. It was observed that although the salts reduced the amount of PbI_2 on the perovskite surface, they did not form a 2D layer. As mentioned earlier, the formation of the 2D layer is associated with formation of new peaks below 10º. Looking at the XRD models in Figure 6-4, no new peak formation was observed below 10º.
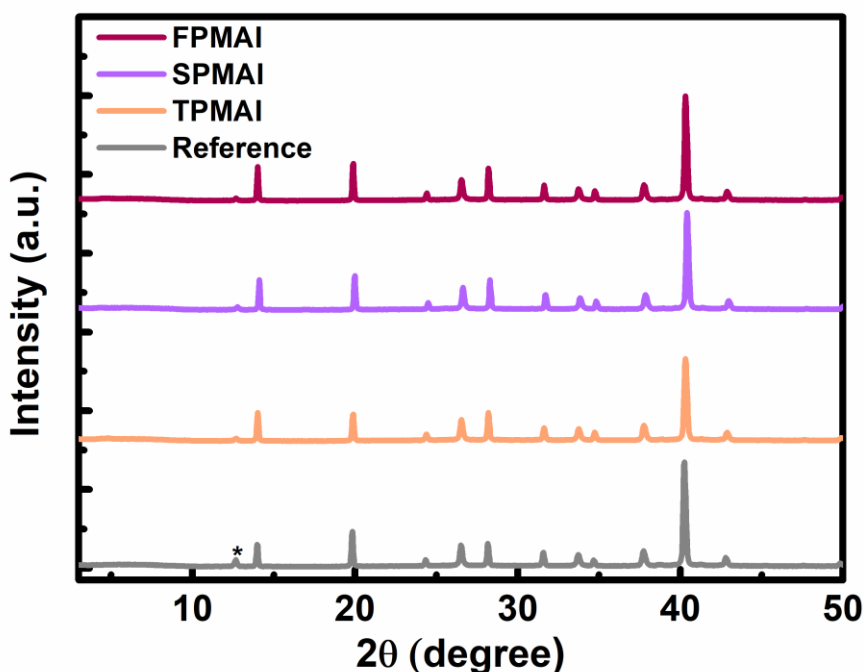
Figure 6-4. XRD pattern of reference 3D perovskite, TPMAI, SPMAI, and FPMAI-treated perovskite films. The * symbol represents the PbI_2 diffraction peak.

Then, SEM images were taken to observe the changes caused by TPMAI, SPMAI and FPMAI salts on the 3D perovskite surface. As seen in the surface SEM images in Figure 6-5, all three salts caused significant change in the 3D perovskite surface. It is clear from in the SEM images that the PbI$_2$ crystals (shiny point in the reference SEM) on the reference film are considerably reduced in the salt-treated films, and these images match the XRD analysis results.
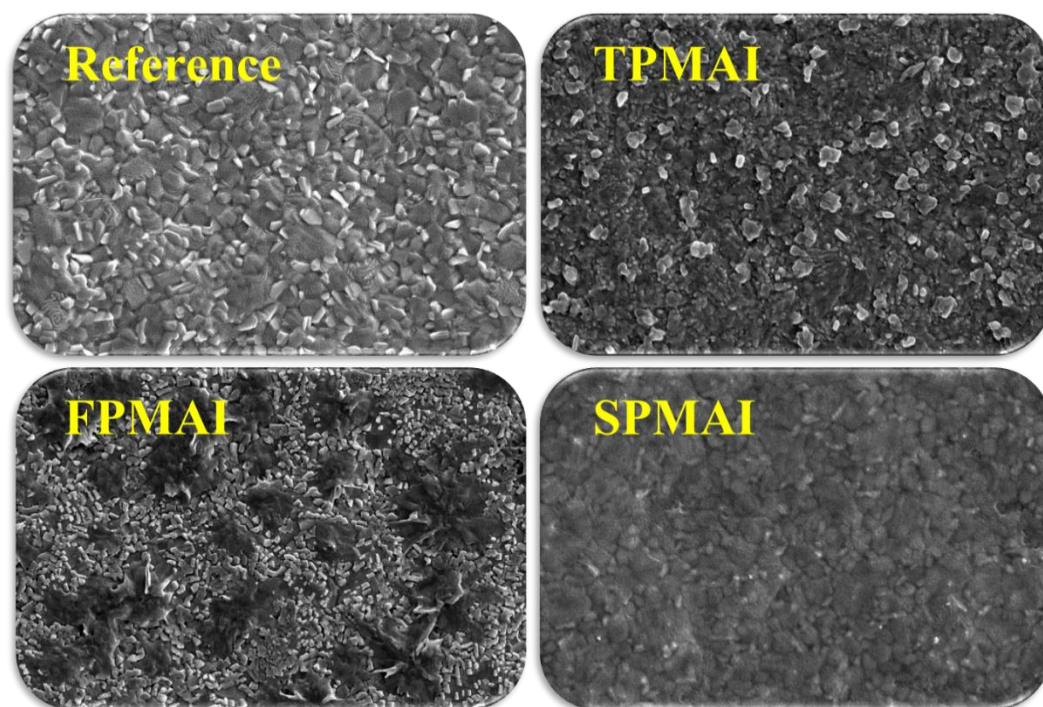
Figure 6-5. Top view SEM images of reference, TPMAI, SPMAI and FPMAI films.

The graph given in Figure 6-6a shows the absorption spectra of the reference and salt-coated films. As seen from the graph, the salts do not contribute to the absorption of the reference film. The photoluminescence (PL) spectra of pristine and salt-treated films are displayed in Figure 6-6a. The PL measurements were performed with the intention of determining the passivation effects upon salt treatment. The films were excited at 450 nm.
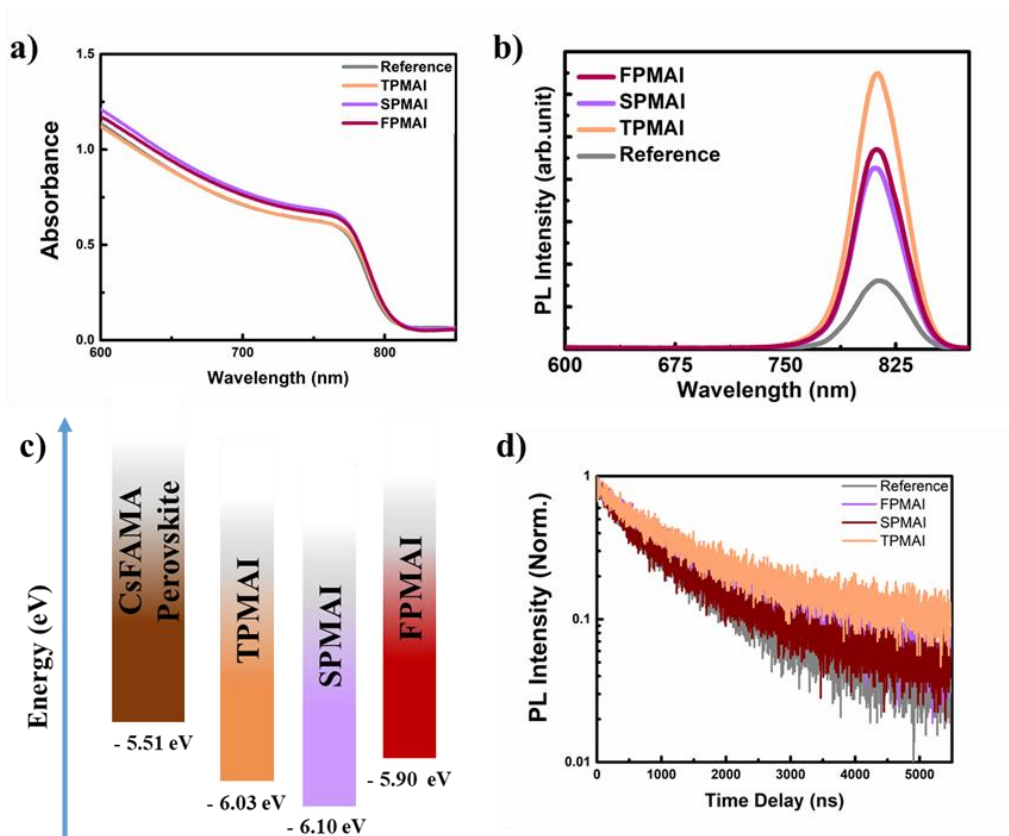
Figure 6-6. a) Absorption spectra of reference, TPMAI, SPMAI and FPMAI films. b) PL spectra of reference, TPMAI, SPMAI and FPMAI films, c) Energy level diagram of reference perovskite and PMAI salts, d) TRPL spectra of reference, TPMAI, SPMAI and FPMAI films

A significant increasing trend in PL intensity was observed for all three salts. These results show that the salts reduce radiation-free recombination and passivate pin holes found in the 3D perovskite or on its surface. When the salts were compared among themselves, it was observed that the organic salt of TPMAI containing the thiophene group had a much higher PL intensity than the other salts. The reason for the difference in increase among these salts from a chemical perspective is under investigation using DFT calculations. According to the TRPL data (Figure 6-6d), the highest lifetime is observed with TPMAI salt, which is in line with the hypothesis about the passivation of iodine traps and the consequent reduction of trap concentration as compared to the reference, SPMAI, and FPMAI salts.

The ionization energies of the reference and salt coated 3D films were determined via ultraviolet photoelectron spectroscopy (UPS) to be -5.51, -6.03, -6.10, and -5.90 eV for the reference, TPMAI, SPMAI, and FPMAI films, respectively. The schematic of energy level diagram of reference and TPMAI, SPMAI, FPMAI treated films is displayed in Figure 6-6c. UPS spectra of reference and TPMAI, SPMAI, FPMAI treated films were given in Figure 6-7.
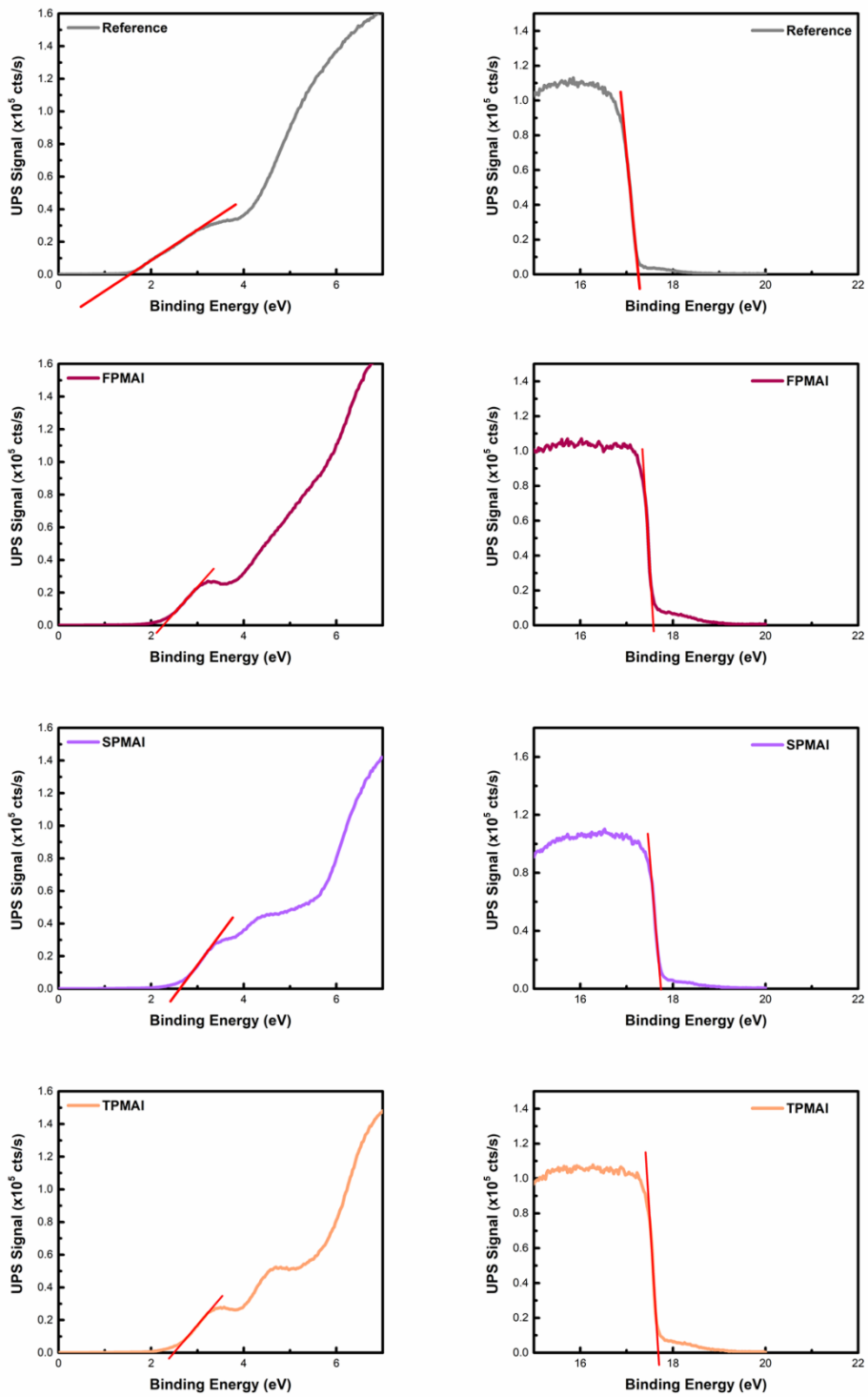
Figure 6-7. UPS spectra of the reference and TPMAI, SPMAI and FPMAI films

In the box charts shown in Figure 6-8, the average open-circuit voltage (V_{OC}), short-circuit current density (J_{SC}), fill factor (FF), and power conversion efficiencies (PCE) of the reference and solar cells treated with TPMAI, SPMAI and FPMAI salts are given. While the average open-circuit voltages were 1.08 V for the reference cell, this value was measured as 1.13, 1.11 and 1.12 V for salts, respectively. While these results are consistent with the PL spectrum and confirmed that organic ammonium salts passivate the reference perovskite film surface and reduce the defects. When the short-circuit current densities are examined, it has been observed that there is no significant difference between the salt-passivated cells and the reference cells. These results are also consistent with the absorption spectrum. The reference cell has an average PCE of 20.63%, while it is 22.93% for TPMAI, 21.45% for SPMAI and 21.87% for FPMAI.
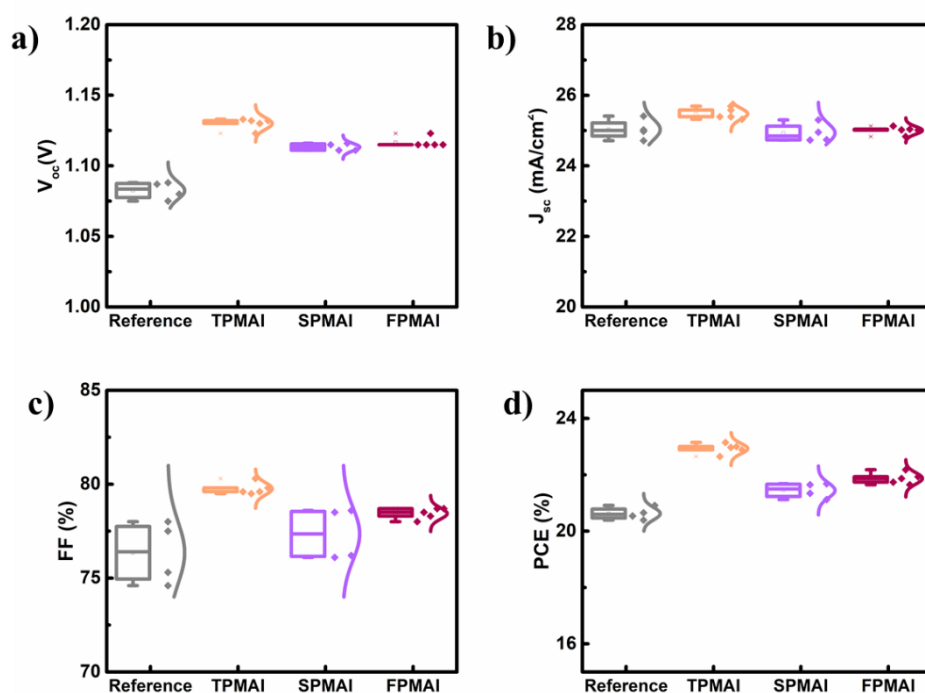
Figure 6-8. Box charts of reference solar cells treated with PMAI salts with different functional groups; a) V_{OC}, b) J_{SC}, c) FF, and d) PCE.

Looking at the current-voltage graphs in Figure 6-9, the highest efficiency of the reference cell was measured as 20.91%, while the highest cell efficiency was 23.15% for TPMAI, 21.65% for SPMAI and 22.18% for FPMAI. The photovoltaic cell parameters shown in Table 6-2 show that promising results were obtained with salt-containing cells. Looking at the results, it was observed that the cells produced with selenophene salts had lower efficiency than the others. One reason behind this decrease is believed to arise from the relatively poor solubility of selenophene salt.
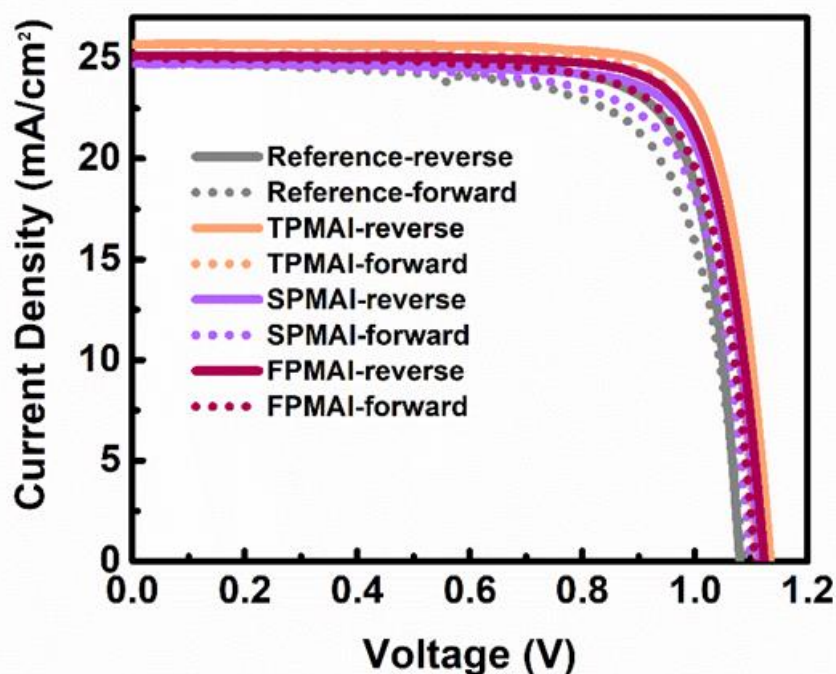
Figure 6-9. J-V curves of the reference and TPMAI, SPMAI and FMAI champion devices simulated under one sun illumination

Table 6-2. Reverse and forward measurement J–V parameters of champion reference, TPMAI, SPMAI and FPMAI cells.

	V_{oc} (V)	J_{sc} (mA/cm²)	FF %	PCE % (the highest)	Hysteresis Index (%)
Reference – reverse	1.08	24.98	77.5	20.91	7.75
Reference – forward	1.09	24.83	71.4	19.29	
TPMAI – reverse	1.13	25.69	79.6	23.15	-
TPMAI – forward	1.11	25.66	78.5	22.37	3.37
SPMAI – reverse	1.12	24.73	78.5	21.65	-
SPMAI – forward	1.10	24.87	73.4	20.09	7.20
FPMAI – reverse	1.12	25.13	78.7	22.18	-
FPMAI – forward	1.11	25.04	76.0	21.12	4.78

Further measurements of these cells were performed, and percent hysteresis indices were calculated. These values were calculated as 7.75% for the reference cell, 3.37% for TPMAI, 7.20% for SPMAI and 4.78% for FPMAI cells. These results show that ion migration slows down in cells containing salt layers, thus increasing intracellular stability.

The integrated current values of the champion cells were measured by external quantum efficiency analysis. The values are shown in Figure 6-10, and the results obtained are consistent with the current density results from the J-V measurements.
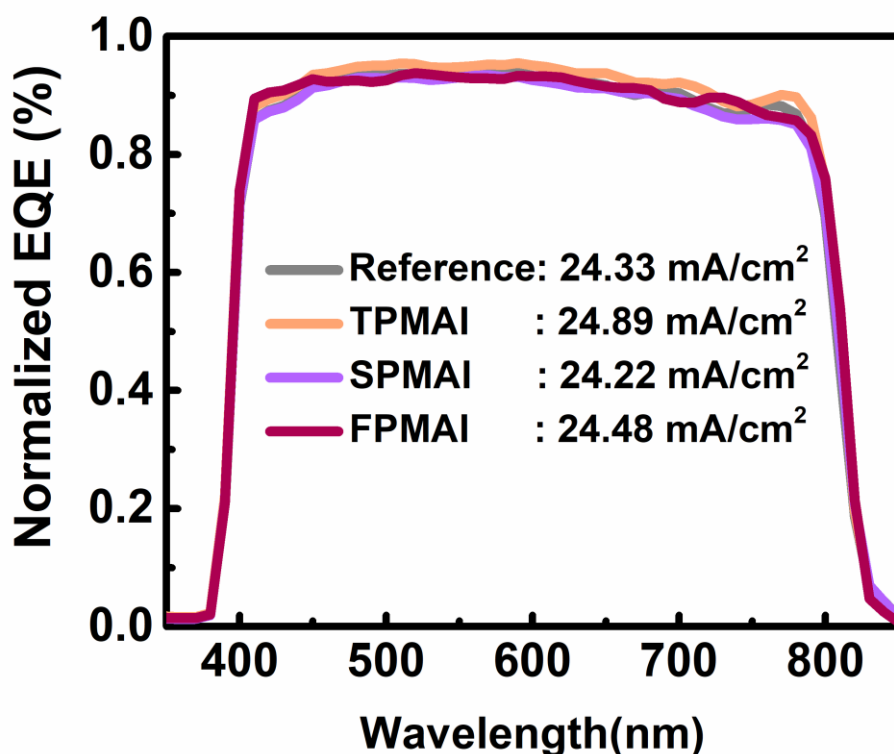
Figure 6-10. EQE spectra of the reference and TPMAI, SPMAI and FMAI champion devices and calculated photocurrent values

Aside from surface characterization and cell measurements, research was carried out to determine the impact of TPMAI, SPMAI, and FPMAI salts on cell stability. In order to determine the stability of the devices, a 1250-hour stability test was conducted, and the results were recorded (Figure 6-11a). The reference cell had a 50% loss of efficiency after 1250 hours, whereas PMAI-salt-treated cells performed excellently. TPMAI-treated cell retained nearly all the cell efficiency after 1250 hours, placing it among the best cells in the literature in terms of both stability and cell efficiency. Contact angle measurements were conducted to the reference and

salt-treated films to understand the films' water resistance (Figure 6-11b). As a result of this analysis, it was observed that the film treated with thiophene had the highest angle (79.3°) and the most hydrophobic surface. The film containing the furan aromatic group also has a higher angle than the reference cell. However, it was observed that the film containing selenophene group salt was not as resistant to water which clearly correlated with stability studies.
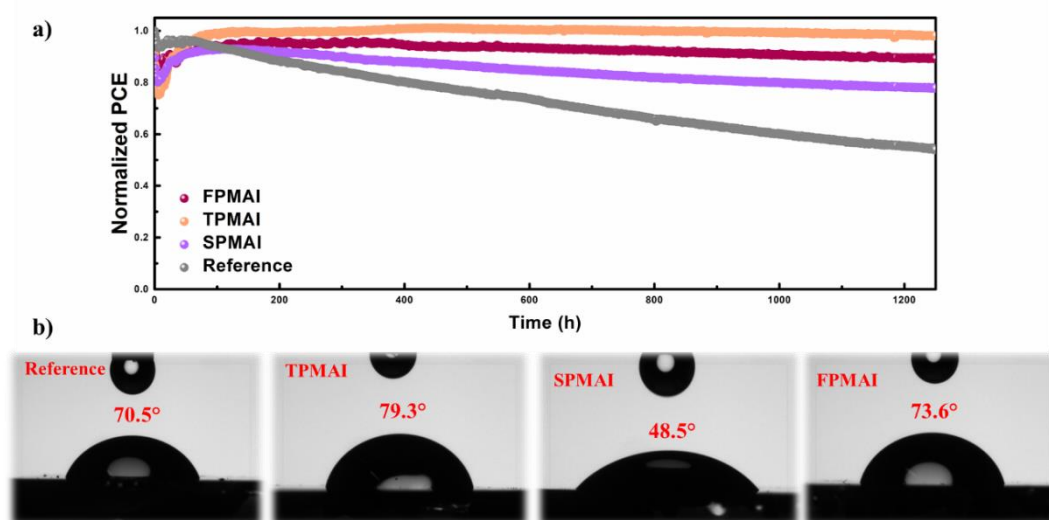
Figure 6-11. a) Comparative operational stability of perovskite devices with and without salt treatment. The devices were measured under a nitrogen environment at room temperature under constant illumination (LED source, ≈1 Sun) at a maximum power point for 1250 h. b) Contact angle images of reference, TPMAI, SPMAI ve FPMAI films

CHAPTER 7

CONCLUSION

This thesis focused on developing hole transport layers and passivation of perovskite layer to enhance charge collections, stability and photovoltaic performance of perovskite solar cells. A wide range of polymeric and small molecule hole transport materials were investigated and their performance was evaluated. Effective doping of spiro-OMeTAD with a novel dopant and successful large cation passivation of 3D perovskite were also demonstrated.

The general finding in this work can be summarized as follows:

i) High performance perovskite solar cells can be achieved by implementation of appropriate dopant-free hole transport materials.

ii) It is possible to obtain good efficiencies by using a novel dopant in smaller amounts than dopants in standard recipes and achieve excellent cell stability.

iii) The interfaces in perovskite solar cells play a very important role in device performance and novel salts introduced in this thesis demonstrate effective passivation materials and enabled realization of highly efficient and extremely stable perovskite solar cells.

In more detail:

In Chapter 3, a systematical investigation of the effect of different aromatic groups and alkyl chains on the optical and electrochemical properties as well as solar cell performance of DPP-based HTMs was discussed. Even though these HTMs were designed and synthesized in a systematical order, differences in molecular weights and film morphologies showed significant influence on cell parameters, thus preventing us from drawing clear conclusions. In future work, the cell performances

will be compared by conducting simultaneous experimental sets with the best-performing polymers, and the relationship between the efficiencies and the chemical structure of the polymers will be explored.

In Chapter 4, dopant-free PT-TPA molecule was introduced an efficient hole transport layer in perovskite solar cells and the effect on the performance and cell stability is investigated. Although a low efficiency has been obtained according to the results of TPA-based molecules in recent years, the 17% efficiency of PT-TPA HTM is still significantly relevant among undoped HTMs. One envisioned reason Since the reason for the relatively low efficiency is the surface compatibility between the HTM and perovskite layers, PT-TPA material will be tested with other perovskite formulations and their photovoltaic performances will be observed. It is important to note here that the most substantial aspect of PT-TPA HTM was its contribution to cell stability. PT-TPA-based cells, which perform very well under temperature and light, showed a very satisfactory performance with almost no loss of efficiency at the end of 70 days under ambient conditions.

In Chapter 5, the incorporation of CFF as a p-type dopant to Spiro-OMeTAD demonstrated great doping ability with improved PSC device efficiency high as 17.8%. Furthermore, it had no unfavourable impact on cell stability like traditional dopant molecules. At the end of the 90-day measurement, while the regular doped cell had no response, it was observed that 87% of the efficiency of the CFF-doped cell was retained. These results provide new insight into HTM doping for applications in PSCs. Related derivates of CFF are currently being synthesized in our labs and their performance with respect to CFF will be evaluated in the future.

In Chapter 6, PMAI based salts have been successfully used to improve the performance of perovskite solar cells, with increased efficiency, stability and reduced surface defects. PMAI-passivated perovskite solar cells displayed improved performance compared to that of unpassivated cells, with an increase of up to 16% in average efficiency and up to 50% in cell stability.

REFERENCES

(1)   Johnstone, N.; Haščič, I.; Popp, D. Renewable Energy Policies and Technological Innovation: Evidence Based on Patent Counts. Environ Resour Econ (Dordr) 2010, 45 (1), 133–155. https://doi.org/10.1007/S10640-009-9309-1/METRICS.

(2)   Raut, K. H.; Chopde, H. N.; Deshmukh, D. W. A Review on Comparative Studies of Diverse Generation in Solar Cell. International Journal of Electrical Engineering and Ethics 1.

(3)   Khatibi, A.; Razi Astaraei, F.; Ahmadi, M. H. Generation and Combination of the Solar Cells: A Current Model Review. Energy Sci Eng 2019, 7 (2), 305–322. https://doi.org/10.1002/ESE3.292.

(4)   Chopra, K. L.; Paulson, P. D.; Dutta, V. Thin-Film Solar Cells: An Overview. Progress in Photovoltaics: Research and Applications 2004, 12 (2–3), 69–92. https://doi.org/10.1002/PIP.541.

(5)   Polman, A.; Knight, M.; Garnett, E. C.; Ehrler, B.; Sinke, W. C. Photovoltaic Materials: Present Efficiencies and Future Challenges. Science (1979) 2016, 352   (6283). https://doi.org/10.1126/SCIENCE.AAD4424/SUPPL_FILE/POLMAN.SM. PDF.

(6)   Green, M. A. Third Generation Photovoltaics: Solar Cells for 2020 and Beyond. Physica E Low Dimens Syst Nanostruct 2002, 14 (1–2), 65–70. https://doi.org/10.1016/S1386-9477(02)00361-2.

(7)   Parida, B.; Iniyan, S.; Goic, R. A Review of Solar Photovoltaic Technologies. Renewable and Sustainable Energy Reviews 2011, 15, 1625–1636. https://doi.org/10.1016/j.rser.2010.11.032.

(8)   Kojima, A.; Teshima, K.; Shirai, Y.; Miyasaka, T. Organometal Halide Perovskites as Visible-Light Sensitizers for Photovoltaic Cells. J Am Chem Soc 2009, 131 (17), 6050–6051. https://doi.org/10.1021/JA809598R/SUPPL_FILE/JA809598R_SI_001.PDF.

(9)   Best Research-Cell Efficiency Chart | Photovoltaic Research | NREL. https://www.nrel.gov/pv/cell-efficiency.html (accessed 2023-01-15).

(10)   Kim, H. S.; Lee, C. R.; Im, J. H.; Lee, K. B.; Moehl, T.; Marchioro, A.; Moon, S. J.; Humphry-Baker, R.; Yum, J. H.; Moser, J. E.; Grätzel, M.; Park, N. G. Lead Iodide Perovskite Sensitized All-Solid-State Submicron Thin Film Mesoscopic Solar Cell with Efficiency Exceeding 9%. Scientific Reports 2012 2:1 2012, 2 (1), 1–7. https://doi.org/10.1038/srep00591.

(11)   Lee, M. M.; Teuscher, J.; Miyasaka, T.; Murakami, T. N.; Snaith, H. J. Efficient Hybrid Solar Cells Based on Meso-Superstructured Organometal Halide Perovskites. Science (1979) 2012, 338 (6107), 643–647. https://doi.org/10.1126/SCIENCE.1228604/SUPPL_FILE/LEE.SM.PDF.

(12)   Jeong, J.; Kim, M.; Seo, J.; Lu, H.; Ahlawat, P.; Mishra, A.; Yang, Y.; Hope, M. A.; Eickemeyer, F. T.; Kim, M.; Yoon, Y. J.; Choi, I. W.; Darwich, B. P.; Choi, S. J.; Jo, Y.; Lee, J. H.; Walker, B.; Zakeeruddin, S. M.; Emsley, L.; Rothlisberger, U.; Hagfeldt, A.; Kim, D. S.; Grätzel, M.; Kim, J. Y. Pseudo-Halide Anion Engineering for α-FAPbI3 Perovskite Solar Cells. Nature 2021 592:7854 2021, 592 (7854), 381–385. https://doi.org/10.1038/s41586-021-03406-5.

(13)   Nazir, G.; Lee, S. Y.; Lee, J. H.; Rehman, A.; Lee, J. K.; Seok, S. Il; Park, S. J. Stabilization of Perovskite Solar Cells: Recent Developments and Future Perspectives. Advanced Materials 2022, 34 (50), 2204380. https://doi.org/10.1002/ADMA.202204380.

(14)   Tan, Z. K.; Moghaddam, R. S.; Lai, M. L.; Docampo, P.; Higler, R.; Deschler, F.; Price, M.; Sadhanala, A.; Pazos, L. M.; Credgington, D.; Hanusch, F.; Bein, T.; Snaith, H. J.; Friend, R. H. Bright Light-Emitting Diodes Based on Organometal Halide Perovskite. Nat Nanotechnol 2014, 9 (9), 687–692. https://doi.org/10.1038/NNANO.2014.149.

(15)   Kim, Y. H.; Cho, H.; Heo, J. H.; Kim, T. S.; Myoung, N. S.; Lee, C. L.; Im, S. H.; Lee, T. W. Multicolored Organic/Inorganic Hybrid Perovskite Light-Emitting Diodes. Advanced Materials 2015, 27 (7), 1248–1254. https://doi.org/10.1002/ADMA.201403751.

(16)   Dou, L.; Yang, Y. (Micheal); You, J.; Hong, Z.; Chang, W.-H.; Li, G.; Yang, Y. Solution-Processed Hybrid Perovskite Photodetectors with High Detectivity. Nature Communications 2014 5:1 2014, 5 (1), 1–6. https://doi.org/10.1038/ncomms6404.

(17)   Wang, K.-L.; Zhou, Y.-H.; Lou, Y.-H.; Wang, Z.-K. Perovskite Indoor Photovoltaics: Opportunity and Challenges. Chem Sci 2021, 12 (36), 11936–11954. https://doi.org/10.1039/D1SC03251H.

(18)   Song, Z.; Watthage, S. C.; Phillips, A. B.; Heben, M. J. Pathways toward High-Performance Perovskite Solar Cells: Review of Recent Advances in Organo-Metal Halide Perovskites for Photovoltaic Applications. https://doi.org/10.1117/1.JPE.6.022001 2016, 6 (2), 022001. https://doi.org/10.1117/1.JPE.6.022001.

(19)   Watthage, S. C.; Song, Z.; Phillips, A. B.; Heben, M. J. Evolution of Perovskite Solar Cells. Perovskite Photovoltaics: Basic to Advanced Concepts and Implementation 2018, 43–88. https://doi.org/10.1016/B978-0-12-812915-9.00003-4.

(20)   Luo, S.; Daoud, W. A. Recent Progress in Organic–Inorganic Halide Perovskite Solar Cells: Mechanisms and Material Design. J Mater Chem A Mater 2015, 3 (17), 8992–9010. https://doi.org/10.1039/C4TA04953E.

(21)   Seo, J. Y.; Akin, S.; Zalibera, M.; Preciado, M. A. R.; Kim, H. S.; Zakeeruddin, S. M.; Milić, J. V.; Grätzel, M. Dopant Engineering for Spiro-OMeTAD Hole-Transporting Materials towards Efficient Perovskite Solar Cells. Adv Funct Mater 2021, 31 (45), 2102124. https://doi.org/10.1002/ADFM.202102124.

(22)   Zhao, Q.; Wu, R.; Zhang, Z.; Xiong, J.; He, Z.; Fan, B.; Dai, Z.; Yang, B.; Xue, X.; Cai, P.; Zhan, S.; Zhang, X.; Zhang, J. Achieving Efficient Inverted Planar Perovskite Solar Cells with Nondoped PTAA as a Hole Transport Layer. Org Electron 2019, 71, 106–112. https://doi.org/10.1016/J.ORGEL.2019.05.019.

(23)   Han, W.; Ren, G.; Liu, J.; Li, Z.; Bao, H.; Liu, C.; Guo, W. Recent Progress of Inverted Perovskite Solar Cells with a Modified PEDOT:PSS Hole Transport Layer. ACS Appl Mater Interfaces 2020, 12 (44), 49297–49322. https://doi.org/10.1021/ACSAMI.0C13576/ASSET/IMAGES/LARGE/AM 0C13576_0014.JPEG.

(24)   Jung, E. H.; Jeon, N. J.; Park, E. Y.; Moon, C. S.; Shin, T. J.; Yang, T. Y.; Noh, J. H.; Seo, J. Efficient, Stable and Scalable Perovskite Solar Cells Using Poly(3-Hexylthiophene). Nature 2019 567:7749 2019, 567 (7749), 511–515. https://doi.org/10.1038/s41586-019-1036-3.

(25)   Gil, B.; Yun, A. J.; Lim, J.; Cho, J.; Kim, B.; Ryu, S.; Kim, J.; Park, B. Design of SnO2 Electron Transport Layer in Perovskite Solar Cells to Achieve 2000 h Stability Under 1 Sun Illumination and 85 °C. Adv Mater Interfaces 2023, 2202148. https://doi.org/10.1002/ADMI.202202148.

(26)   Kim, H. S.; Park, N. G. Parameters Affecting I-V Hysteresis of CH3NH3PbI3 Perovskite Solar Cells: Effects of Perovskite Crystal Size and Mesoporous TiO2 Layer. Journal of Physical Chemistry Letters 2014, 5 (17), 2927–2934. https://doi.org/10.1021/JZ501392M/SUPPL_FILE/JZ501392M_SI_001.PD F.

(27) Liu, C.; Wu, W.; Zhang, D.; Li, Z.; Ren, G.; Han, W.; Guo, W. Effective Stability Enhancement in ZnO-Based Perovskite Solar Cells by MACl Modification. J Mater Chem A Mater 2021, 9 (20), 12161–12168. https://doi.org/10.1039/D1TA02697F.

(28) Roose, B.; Baena, J. P. C.; Gödel, K. C.; Graetzel, M.; Hagfeldt, A.; Steiner, U.; Abate, A. Mesoporous SnO2 Electron Selective Contact Enables UV-Stable Perovskite Solar Cells. Nano Energy 2016, 30, 517–522. https://doi.org/10.1016/J.NANOEN.2016.10.055.

(29) Ke, W.; Fang, G.; Liu, Q.; Xiong, L.; Qin, P.; Tao, H.; Wang, J.; Lei, H.; Li, B.; Wan, J.; Yang, G.; Yan, Y. Lowerature Solution-Processed Tin Oxide as an Alternative Electron Transporting Layer for Efficient Perovskite Solar Cells. J Am Chem Soc 2015, 137 (21), 6730–6733. https://doi.org/10.1021/JACS.5B01994/SUPPL_FILE/JA5B01994_SI_001. PDF.

(30) Jiang, Q.; Chu, Z.; Wang, P.; Yang, X.; Liu, H.; Wang, Y.; Yin, Z.; Wu, J.; Zhang, X.; You, J. Planar-Structure Perovskite Solar Cells with Efficiency beyond 21%. Advanced Materials 2017, 29 (46), 1703852. https://doi.org/10.1002/ADMA.201703852.

(31) Kung, P. K.; Li, M. H.; Lin, P. Y.; Chiang, Y. H.; Chan, C. R.; Guo, T. F.; Chen, P. A Review of Inorganic Hole Transport Materials for Perovskite Solar Cells. Adv Mater Interfaces 2018, 5 (22), 1800882. https://doi.org/10.1002/ADMI.201800882.

(32) Arora, N.; Dar, M. I.; Hinderhofer, A.; Pellet, N.; Schreiber, F.; Zakeeruddin, S. M.; Grätzel, M. Perovskite Solar Cells with CuSCN Hole Extraction Layers Yield Stabilized Efficiencies Greater than 20%. Science (1979) 2017, 358 (6364), 768–771. https://doi.org/10.1126/SCIENCE.AAM5655/SUPPL_FILE/AAM5655_AR ORA_SM.PDF.

(33)   Islam, M. B.; Yanagida, M.; Shirai, Y.; Nabetani, Y.; Miyano, K. NiOx Hole Transport Layer for Perovskite Solar Cells with Improved Stability and Reproducibility. ACS Omega 2017, 2 (5), 2291–2299. https://doi.org/10.1021/ACSOMEGA.7B00538/ASSET/IMAGES/LARGE/ AO-2017-00538G_0007.JPEG.

(34)   Mahajan, P.; Padha, B.; Verma, S.; Gupta, V.; Datt, R.; Tsoi, W. C.; Satapathi, S.; Arya, S. Review of Current Progress in Hole-Transporting Materials for Perovskite Solar Cells. Journal of Energy Chemistry 2022, 68, 330–386. https://doi.org/10.1016/J.JECHEM.2021.12.003.

(35)   Rajeswari, R.; Mrinalini, M.; Prasanthkumar, S.; Giribabu, L. Emerging of Inorganic Hole Transporting Materials For Perovskite Solar Cells. The Chemical Record 2017, 17 (7), 681–699. https://doi.org/10.1002/TCR.201600117.

(36)   Chen, J.; Park, N. G. Inorganic Hole Transporting Materials for Stable and High Efficiency Perovskite Solar Cells. Journal of Physical Chemistry C 2018, 122 (25), 14039–14063. https://doi.org/10.1021/ACS.JPCC.8B01177/ASSET/IMAGES/LARGE/JP-2018-01177T_0022.JPEG.

(37)   Singh, R.; Singh, P. K.; Bhattacharya, B.; Rhee, H. W. Review of Current Progress in Inorganic Hole-Transport Materials for Perovskite Solar Cells. Appl Mater Today 2019, 14, 175–200. https://doi.org/10.1016/J.APMT.2018.12.011.

(38)   Arumugam, G. M.; Karunakaran, S. K.; Liu, C.; Zhang, C.; Guo, F.; Wu, S.; Mai, Y. Inorganic Hole Transport Layers in Inverted Perovskite Solar Cells: A Review. Nano Select 2021, 2 (6), 1081–1116. https://doi.org/10.1002/NANO.202000200.

(39)   Gil, B.; Yun, A. J.; Lee, Y.; Kim, J.; Lee, B.; Park, B. Recent Progress in Inorganic Hole Transport Materials for Efficient and Stable Perovskite Solar

Cells. Electronic Materials Letters 2019, 15 (5), 505–524. https://doi.org/10.1007/S13391-019-00163-6/FIGURES/12.

(40)   Bakr, Z. H.; Wali, Q.; Fakharuddin, A.; Schmidt-Mende, L.; Brown, T. M.; Jose, R. Advances in Hole Transport Materials Engineering for Stable and Efficient Perovskite Solar Cells. Nano Energy 2017, 34, 271–305. https://doi.org/10.1016/J.NANOEN.2017.02.025.

(41)   Ke, Q. bin; Wu, J. R.; Lin, C. C.; Chang, S. H. Understanding the PEDOT:PSS, PTAA and P3CT-X Hole-Transport-Layer-Based Inverted Perovskite Solar Cells. Polymers 2022, Vol. 14, Page 823 2022, 14 (4), 823. https://doi.org/10.3390/POLYM14040823.

(42)   Zhang, F.; Yao, Z.; Guo, Y.; Li, Y.; Bergstrand, J.; Brett, C. J.; Cai, B.; Hajian, A.; Guo, Y.; Yang, X.; Gardner, J. M.; Widengren, J.; Roth, S. v.; Kloo, L.; Sun, L. Polymeric, Cost-Effective, Dopant-Free Hole Transport Materials for Efficient and Stable Perovskite Solar Cells. J Am Chem Soc 2019, 141 (50), 19700–19707. https://doi.org/10.1021/JACS.9B08424/ASSET/IMAGES/LARGE/JA9B08 424_0005.JPEG.

(43)   Astridge, D. D.; Hoffman, J. B.; Zhang, F.; Park, S. Y.; Zhu, K.; Sellinger, A. Polymer Hole Transport Materials for Perovskite Solar Cells via Buchwald-Hartwig Amination. ACS Appl Polym Mater 2021, 3 (11), 5578–5587. https://doi.org/10.1021/ACSAPM.1C00891/ASSET/IMAGES/LARGE/AP1 C00891_0004.JPEG.

(44)   Kim, G. W.; Kang, G.; Malekshahi Byranvand, M.; Lee, G. Y.; Park, T. Gradated Mixed Hole Transport Layer in a Perovskite Solar Cell: Improving Moisture Stability and Efficiency. ACS Appl Mater Interfaces 2017, 9 (33), 27720–27726.

https://doi.org/10.1021/ACSAMI.7B07071/ASSET/IMAGES/LARGE/AM-2017-07071P_0005.JPEG.

(45)   Kim, G. W.; Kang, G.; Kim, J.; Lee, G. Y.; Kim, H. il; Pyeon, L.; Lee, J.; Park, T. Dopant-Free Polymeric Hole Transport Materials for Highly Efficient and Stable Perovskite Solar Cells. Energy Environ Sci 2016, 9 (7), 2326–2333. https://doi.org/10.1039/C6EE00709K.

(46)   Yin, X.; Song, Z.; Li, Z.; Tang, W. Toward Ideal Hole Transport Materials: A Review on Recent Progress in Dopant-Free Hole Transport Materials for Fabricating Efficient and Stable Perovskite Solar Cells. Energy Environ Sci 2020, 13 (11), 4057–4086. https://doi.org/10.1039/D0EE02337J.

(47)   Li, S.; Cao, Y. L.; Li, W. H.; Bo, Z. S. A Brief Review of Hole Transporting Materials Commonly Used in Perovskite Solar Cells. Rare Metals 2021 40:10 2021, 40 (10), 2712–2729. https://doi.org/10.1007/S12598-020-01691-Z.

(48)   Murugan, P.; Hu, T.; Hu, X.; Chen, Y. Advancements in Organic Small Molecule Hole-Transporting Materials for Perovskite Solar Cells: Past and Future. J Mater Chem A Mater 2022, 10 (10), 5044–5081. https://doi.org/10.1039/D1TA11039J.

(49)   Zhu, W.; Zhou, K.; Fo, Y.; Li, Y.; Guo, B.; Zhang, X.; Zhou, X. Rational Design of Small Molecule Hole-Transporting Materials with a Linear π-Bridge for Highly Efficient Perovskite Solar Cells. Physical Chemistry Chemical Physics 2022, 24 (31), 18793–18804. https://doi.org/10.1039/D2CP02036J.

(50)   Wang, Y.; Chen, W.; Wang, L.; Tu, B.; Chen, T.; Liu, B.; Yang, K.; Koh, C. W.; Zhang, X.; Sun, H.; Chen, G.; Feng, X.; Woo, H. Y.; Djurišić, A. B.; He, Z.; Guo, X. Dopant-Free Small-Molecule Hole-Transporting Material for Inverted Perovskite Solar Cells with Efficiency Exceeding 21%. Advanced Materials 2019, 31 (35), 1902781. https://doi.org/10.1002/ADMA.201902781.

(51) Rodríguez-Seco, C.; Cabau, L.; Vidal-Ferran, A.; Palomares, E. Advances in the Synthesis of Small Molecules as Hole Transport Materials for Lead Halide Perovskite Solar Cells. Acc Chem Res 2018, 51 (4), 869–880. https://doi.org/10.1021/ACS.ACCOUNTS.7B00597/ASSET/IMAGES/LARGE/AR-2017-00597P_0013.JPEG.

(52) Desoky, M. M. H.; Bonomo, M.; Buscaino, R.; Fin, A.; Viscardi, G.; Barolo, C.; Quagliotto, P. Dopant-Free All-Organic Small-Molecule HTMs for Perovskite Solar Cells: Concepts and Structure–Property Relationships. Energies 2021, Vol. 14, Page 2279 2021, 14 (8), 2279. https://doi.org/10.3390/EN14082279.

(53) Bach, U.; Lupo, D.; Comte, P.; Moser, J. E.; Weissörtel, F.; Salbeck, J.; Spreitzer, H.; Grätzel, M. Solid-State Dye-Sensitized Mesoporous TiO2 Solar Cells with High Photon-to-Electron Conversion Efficiencies. Nature 1998 395:6702 1998, 395 (6702), 583–585. https://doi.org/10.1038/26936.

(54) Krüger, J.; Plass, R.; Cevey, L.; Piccirelli, M.; Grätzel, M.; Bach, U. High Efficiency Solid-State Photovoltaic Device Due to Inhibition of Interface Charge Recombination. Appl Phys Lett 2001, 79 (13), 2085. https://doi.org/10.1063/1.1406148.

(55) Noh, J. H.; Jeon, N. J.; Choi, Y. C.; Nazeeruddin, M. K.; Grätzel, M.; Seok, S. il. Nanostructured TiO2/CH3NH3PbI3 Heterojunction Solar Cells Employing Spiro-OMeTAD/Co-Complex as Hole-Transporting Material. J Mater Chem A Mater 2013, 1 (38), 11842–11847. https://doi.org/10.1039/C3TA12681A.

(56) Snaith, H. J.; Grätzel, M. Enhanced Charge Mobility in a Molecular Hole Transporter via Addition of Redox Inactive Ionic Dopant: Implication to Dye-Sensitized Solar Cells. Appl Phys Lett 2006, 89 (26), 262114. https://doi.org/10.1063/1.2424552.

(57)   Noh, J. H.; Jeon, N. J.; Choi, Y. C.; Nazeeruddin, M. K.; Grätzel, M.; Seok,
         S. il. Nanostructured TiO2/CH3NH3PbI3 Heterojunction Solar Cells
         Employing Spiro-OMeTAD/Co-Complex as Hole-Transporting Material. J
         Mater   Chem   A   Mater   2013,   1   (38),   11842–11847.
         https://doi.org/10.1039/C3TA12681A.

(58)   Pfeiffer, M.; Leo, K.; Zhou, X.; Huang, J. S.; Hofmann, M.; Werner, A.;
         Blochwitz-Nimoth, J. Doped Organic Semiconductors: Physics and
         Application in Light Emitting Diodes. Org Electron 2003, 4 (2–3), 89–103.
         https://doi.org/10.1016/J.ORGEL.2003.08.004.

(59)   Fantacci, S.; de Angelis, F.; Nazeeruddin, M. K.; Grätzel, M. Electronic and
         Optical Properties of the Spiro-MeOTAD Hole Conductor in Its Neutral and
         Oxidized Forms: A DFT/TDDFT Investigation. Journal of Physical
         Chemistry C 2011, 115 (46), 23126–23133.
         https://doi.org/10.1021/JP207968B/SUPPL_FILE/JP207968B_SI_001.PDF.

(60)   Cappel, U. B.; Daeneke, T.; Bach, U. Oxygen-Induced Doping of Spiro-
         MeOTAD in Solid-State Dye-Sensitized Solar Cells and Its Impact on
         Device Performance. Nano Lett 2012, 12 (9), 4925–4931.
         https://doi.org/10.1021/NL302509Q/SUPPL_FILE/NL302509Q_SI_001.P
         DF.

(61)   Wang, S.; Yuan, W.; Meng, Y. S. Spectrum-Dependent Spiro-OMeTAD
         Oxidization Mechanism in Perovskite Solar Cells. ACS Appl Mater
         Interfaces 2015, 7 (44), 24791–24798.
         https://doi.org/10.1021/ACSAMI.5B07703/ASSET/IMAGES/AM-2015-
         07703F_M010.GIF.

(62)   Snaith, H. J.; Abate, A.; Ball, J. M.; Eperon, G. E.; Leijtens, T.; Noel, N. K.;
         Stranks, S. D.; Wang, J. T. W.; Wojciechowski, K.; Zhang, W. Anomalous
         Hysteresis in Perovskite Solar Cells. Journal of Physical Chemistry Letters
         2014, 5 (9), 1511–1515.

https://doi.org/10.1021/JZ500113X/SUPPL_FILE/JZ500113X_SI_001.PDF
.

(63)   Zhang, T.; Chen, H.; Bai, Y.; Xiao, S.; Zhu, L.; Hu, C.; Xue, Q.; Yang, S. Understanding the Relationship between Ion Migration and the Anomalous Hysteresis in High-Efficiency Perovskite Solar Cells: A Fresh Perspective from Halide Substitution. Nano Energy 2016, 26, 620–630. https://doi.org/10.1016/J.NANOEN.2016.05.052.

(64)   Wei, J.; Zhao, Y.; Li, H.; Li, G.; Pan, J.; Xu, D.; Zhao, Q.; Yu, D. Hysteresis Analysis Based on the Ferroelectric Effect in Hybrid Perovskite Solar Cells. Journal of Physical Chemistry Letters 2014, 5 (21), 3937–3945. https://doi.org/10.1021/JZ502111U/SUPPL_FILE/JZ502111U_SI_001.PDF
.

(65)   Li, Z.; Xiao, C.; Yang, Y.; Harvey, S. P.; Kim, D. H.; Christians, J. A.; Yang, M.; Schulz, P.; Nanayakkara, S. U.; Jiang, C. S.; Luther, J. M.; Berry, J. J.; Beard, M. C.; Al-Jassim, M. M.; Zhu, K. Extrinsic Ion Migration in Perovskite Solar Cells. Energy Environ Sci 2017, 10 (5), 1234–1242. https://doi.org/10.1039/C7EE00358G.

(66)   Bai, Y.; Meng, X.; Yang, S. Interface Engineering for Highly Efficient and Stable Planar P-i-n Perovskite Solar Cells. Adv Energy Mater 2018, 8 (5), 1701883. https://doi.org/10.1002/AENM.201701883.

(67)   Zheng, X.; Chen, B.; Dai, J.; Fang, Y.; Bai, Y.; Lin, Y.; Wei, H.; Zeng, X. C.; Huang, J. Defect Passivation in Hybrid Perovskite Solar Cells Using Quaternary Ammonium Halide Anions and Cations. Nature Energy 2017 2:7 2017, 2 (7), 1–9. https://doi.org/10.1038/nenergy.2017.102.

(68)   Zhao, T.; Chueh, C. C.; Chen, Q.; Rajagopal, A.; Jen, A. K. Y. Defect Passivation of Organic-Inorganic Hybrid Perovskites by Diammonium Iodide toward High-Performance Photovoltaic Devices. ACS Energy Lett 2016, 1 (4), 757–763.

https://doi.org/10.1021/ACSENERGYLETT.6B00327/ASSET/IMAGES/LARGE/NZ-2016-00327P_0006.JPEG.

(69)   Mahdi Tavakoli, M.; Bi, D.; Pan, L.; Hagfeldt, A.; Mohammed Zakeeruddin, S.; Grätzel, M.; Tavakoli, M. M.; Bi, D.; Pan, L.; Hagfeldt, A.; Zakeeruddin, S. M.; Grätzel, M. Adamantanes Enhance the Photovoltaic Performance and Operational Stability of Perovskite Solar Cells by Effective Mitigation of Interfacial Defect States. Adv Energy Mater 2018, 8 (19), 1800275. https://doi.org/10.1002/AENM.201800275.

(70)   Wang, F.; Geng, W.; Zhou, Y.; Fang, H.-H.; Tong, C.-J.; Antonietta Loi, M.; Liu, L.-M.; Zhao, N.; Wang, F.; Zhou, Y.; Zhao, N.; Geng, W.; Tong, C.; Liu, L.; Fang, H.; Loi, M. A. Phenylalkylamine Passivation of Organolead Halide Perovskites Enabling High-Efficiency and Air-Stable Photovoltaic Cells. Advanced Materials 2016, 28 (45), 9986–9992. https://doi.org/10.1002/ADMA.201603062.

(71)   Isakova, A.; Topham, P. D. Polymer Strategies in Perovskite Solar Cells. J Polym Sci B Polym Phys 2017, 55 (7), 549–568. https://doi.org/10.1002/POLB.24301.

(72)   Roy, S. Applications of Polymers in Perovskite Solar Cells: A Review. Annals of Chemical Science Research 2020, 2 (2). https://doi.org/10.31031/ACSR.2020.02.000531.

(73)   Girish, K. H.; Vishnumurthy, K. A.; Roopa, T. S. Role of Conducting Polymers in Enhancing the Stability and Performance of Perovskite Solar Cells: A Brief Review. Materials Today Sustainability 2022, 17, 100090. https://doi.org/10.1016/J.MTSUST.2021.100090.

(74)   Wang, F.; Cao, Y.; Chen, C.; Chen, Q.; Wu, X.; Li, X.; Qin, T.; Huang, W. Materials toward the Upscaling of Perovskite Solar Cells: Progress, Challenges, and Strategies. Adv Funct Mater 2018, 28 (52), 1803753. https://doi.org/10.1002/ADFM.201803753.

160

(75)   Bakr, Z. H.; Wali, Q.; Fakharuddin, A.; Schmidt-Mende, L.; Brown, T. M.;
        Jose, R. Advances in Hole Transport Materials Engineering for Stable and
        Efficient Perovskite Solar Cells. Nano Energy 2017, 34, 271–305.
        https://doi.org/10.1016/J.NANOEN.2017.02.025.

(76)   Zhao, X.; Wang, M. Organic Hole-Transporting Materials for Efficient
        Perovskite Solar Cells. Mater Today Energy 2018, 7, 208–220.
        https://doi.org/10.1016/J.MTENER.2017.09.011.

(77)   Cai, B.; Xing, Y.; Yang, Z.; Zhang, W. H.; Qiu, J. High Performance Hybrid
        Solar Cells Sensitized by Organolead Halide Perovskites. Energy Environ Sci
        2013, 6 (5), 1480–1485. https://doi.org/10.1039/C3EE40343B.

(78)   Dubey, A.; Adhikari, N.; Venkatesan, S.; Gu, S.; Khatiwada, D.; Wang, Q.;
        Mohammad, L.; Kumar, M.; Qiao, Q. Solution Processed Pristine PDPP3T
        Polymer as Hole Transport Layer for Efficient Perovskite Solar Cells with
        Slower Degradation. Solar Energy Materials and Solar Cells 2016, 145, 193–
        199. https://doi.org/10.1016/J.SOLMAT.2015.10.008.

(79)   Liu, J.; Ge, Q.; Zhang, W.; Ma, J.; Ding, J.; Yu, G.; Hu, J. Highly π-Extended
        Copolymer as Additive-Free Hole-Transport Material for Perovskite Solar
        Cells. Nano Research 2018 11:1 2017, 11 (1), 185–194.
        https://doi.org/10.1007/S12274-017-1618-Z.

(80)   Maruo, H.; Sasaki, Y.; Harada, K.; Suwa, K.; Oyaizu, • Kenichi; Segawa, H.;
        Carter, • Kenneth; Nishide, H. Hole-Transporting Diketopyrrolopyrrole-
        Thiophene Polymers and Their Additive-Free Application for a Perovskite-
        Type Solar Cell with an Efficiency of 16.3%. Polym J 2019, 51, 91–96.
        https://doi.org/10.1038/s41428-018-0116-9.

(81)   Kulshreshtha, C.; Clement, A.; Pascher, T.; Sundström, V.; Matyba, P.
        Investigating Ultrafast Carrier Dynamics in Perovskite Solar Cells with an
        Extended π-Conjugated Polymeric Diketopyrrolopyrrole Layer for Hole

Transportation. RSC Adv 2020, 10 (11), 6618–6624. https://doi.org/10.1039/C9RA10009A.

(82) Zhao, H.; Yang, S.; Han, Y.; Yuan, S.; Jiang, H.; Duan, C.; Liu, Z.; Liu, S. A High Mobility Conjugated Polymer Enables Air and Thermally Stable CsPbI2Br Perovskite Solar Cells with an Efficiency Exceeding 15%. Adv Mater Technol 2019, 4 (9), 1900311. https://doi.org/10.1002/ADMT.201900311.

(83) Guo, X.; Zhang, B.; Lin, Z.; Su, J.; Yang, Z.; Zhang, C.; Chang, J.; Liu, S.; Hao, Y. Highly Efficient Perovskite Solar Cells Based on a Dopant-Free Conjugated DPP Polymer Hole Transport Layer: Influence of Solvent Vapor Annealing. Sustain Energy Fuels 2018, 2 (10), 2154–2159. https://doi.org/10.1039/C8SE00233A.

(84) Fan, W. J.; Li, W. S.; Zhang, Q.; Liu, W.; Ma, Y.; Wang, Z.; Zhu, M.; Wang, J.; Khalil, M.; Wang, H.; Gao, W. Improving the Fill Factor of Perovskite Solar Cells by Employing an Amine-Tethered Diketopyrrolopyrrole-Based Polymer as the Dopant-Free Hole Transport Layer. ACS Appl Energy Mater 2020, 3 (10), 9600–9609. https://doi.org/10.1021/ACSAEM.0C01085/SUPPL_FILE/AE0C01085_SI_001.PDF.

(85) Liu, W.; Ma, Y.; Wang, Z.; Mu, Z.; Gao, W.; Fan, W.; Li, W. S.; Zhang, Q. Improving the Hole Transport Performance of Perovskite Solar Cells through Adjusting the Mobility of the As-Synthesized Conjugated Polymer. J Mater Chem C Mater 2021, 9 (10), 3421–3428. https://doi.org/10.1039/D0TC05725H.

(86) Hou, Y.; Du, X.; Scheiner, S.; McMeekin, D. P.; Wang, Z.; Li, N.; Killian, M. S.; Chen, H.; Richter, M.; Levchuk, I.; Schrenker, N.; Spiecker, E.; Stubhan, T.; Luechinger, N. A.; Hirsch, A.; Schmuki, P.; Steinrück, H. P.; Fink, R. H.; Halik, M.; Snaith, H. J.; Brabec, C. J. A Generic Interface to

Reduce the Efficiency-Stability-Cost Gap of Perovskite Solar Cells. Science (1979) 2017, 358 (6367), 1192–1197. https://doi.org/10.1126/SCIENCE.AAO5561/SUPPL_FILE/AAO5561_HOU_SM.PDF.

(87)   Fu, Q.; Xu, Z.; Tang, X.; Liu, T.; Dong, X.; Zhang, X.; Zheng, N.; Xie, Z.; Liu, Y. Multifunctional Two-Dimensional Conjugated Materials for Dopant-Free Perovskite Solar Cells with Efficiency Exceeding 22%. 2023. https://doi.org/10.1021/acsenergylett.1c00385.

(88)   Fu, Q.; Liu, H.; Tang, X.; Wang, R.; Chen, M.; Liu, Y. Multifunctional Two-Dimensional Polymers for Perovskite Solar Cells with Efficiency Exceeding 24%. ACS Energy Lett 2022, 7 (3), 1128–1136. https://doi.org/10.1021/ACSENERGYLETT.1C02812/ASSET/IMAGES/LARGE/NZ1C02812_0005.JPEG.

(89)   Zade, S. S.; Zamoshchik, N.; Bendikov, M. Oligo- and Polyselenophenes: A Theoretical Study. Chemistry – A European Journal 2009, 15 (34), 8613–8624. https://doi.org/10.1002/CHEM.200900971.

(90)   Tsoi, W. C.; James, D. T.; Domingo, E. B.; Kim, J. S.; Al-Hashimi, M.; Murphy, C. E.; Stingelin, N.; Heeney, M.; Kim, J. S. Effects of a Heavy Atom on Molecular Order and Morphology in Conjugated Polymer:Fullerene Photovoltaic Blend Thin Films and Devices. ACS Nano 2012, 6 (11), 9646–9656. https://doi.org/10.1021/NN304024G/SUPPL_FILE/NN304024G_SI_001.PDF.

(91)   Marsh, A. v.; Heeney, M. Conjugated Polymers Based on Selenophene Building Blocks. Polymer Journal 2022 2022, 1–11. https://doi.org/10.1038/s41428-022-00731-y.

(92)   Takahashi, K.; Suzuki, Y. Perovskite Solar Cells with CuI Inorganic Hole Conductor. Jpn J Appl Phys 2017, 56 (8), 08MC04. https://doi.org/10.7567/JJAP.56.08MC04/XML.

(93)   Lu, C.; Zhang, W.; Jiang, Z.; Zhang, Y.; Ni, C. CuI/Spiro-OMeTAD Double-Layer Hole Transport Layer to Improve Photovoltaic Performance of Perovskite Solar Cells. Coatings 2021, Vol. 11, Page 978 2021, 11 (8), 978. https://doi.org/10.3390/COATINGS11080978.

(94)   Pang, S.; Chen, D. High-Quality Perovskite Film Preparations for Efficient Perovskite Solar Cells. Emerging Solar Energy Materials 2018. https://doi.org/10.5772/INTECHOPEN.75103.

(95)   Maruo, H.; Sasaki, Y.; Harada, K.; Suwa, K.; Oyaizu, K.; Segawa, H.; Carter, K.; Nishide, H. Hole-Transporting Diketopyrrolopyrrole-Thiophene Polymers and Their Additive-Free Application for a Perovskite-Type Solar Cell with an Efficiency of 16.3%. Polymer Journal 2018 51:1 2018, 51 (1), 91–96. https://doi.org/10.1038/s41428-018-0116-9.

(96)   Guo, X.; Zhang, B.; Lin, Z.; Su, J.; Yang, Z.; Zhang, C.; Chang, J.; Liu, S.; Hao, Y. Highly Efficient Perovskite Solar Cells Based on a Dopant-Free Conjugated DPP Polymer Hole Transport Layer: Influence of Solvent Vapor Annealing. Sustain Energy Fuels 2018, 2 (10), 2154–2159. https://doi.org/10.1039/C8SE00233A.

(97)   Zhang, H.; Liu, M.; Yang, W.; Judin, L.; Hukka, T. I.; Priimagi, A.; Deng, Z.; Vivo, P. Thionation Enhances the Performance of Polymeric Dopant-Free Hole-Transporting Materials for Perovskite Solar Cells. Adv Mater Interfaces 2019, 6 (18), 1901036. https://doi.org/10.1002/admi.201901036.

(98)   Yang, J.; Siempelkamp, B. D.; Liu, D.; Kelly, T. L. Investigation of CH3NH3PbI3degradation Rates and Mechanisms in Controlled Humidity Environments Using in Situ Techniques. ACS Nano 2015, 9 (2), 1955–1963.

https://doi.org/10.1021/NN506864K/SUPPL_FILE/NN506864K_SI_002.A VI.

(99) Kim, H. S.; Seo, J. Y.; Park, N. G. Impact of Selective Contacts on Long-Term Stability of CH3NH3PbI3 Perovskite Solar Cells. Journal of Physical Chemistry C 2016, 120 (49), 27840–27848. https://doi.org/10.1021/ACS.JPCC.6B09412/ASSET/IMAGES/LARGE/JP-2016-09412Q_0010.JPEG.

(100) Li, Z.; Xiao, C.; Yang, Y.; Harvey, S. P.; Kim, D. H.; Christians, J. A.; Yang, M.; Schulz, P.; Nanayakkara, S. U.; Jiang, C. S.; Luther, J. M.; Berry, J. J.; Beard, M. C.; Al-Jassim, M. M.; Zhu, K. Extrinsic Ion Migration in Perovskite Solar Cells. Energy Environ Sci 2017, 10 (5), 1234–1242. https://doi.org/10.1039/C7EE00358G.

(101) Sarvari, H.; Wang, X.; Wang, Y.; Zhang, P.; Li, S.; Singh, V. P.; Chen, Z. Photovoltaic Performance of Lead-Iodide Perovskite Solar Cells Fabricated under Ambient Air Conditions with HTM Solution Excluding LiTFSI. IEEE J Photovolt 2018, 8 (4), 1051–1057. https://doi.org/10.1109/JPHOTOV.2018.2838443.

(102) Zhang, Y.; Kirs, A.; Ambroz, F.; Lin, C.-T.; R Bati, A. S.; Parkin, I. P.; Shapter, J. G.; Batmunkh, M.; Macdonald, T. J.; Zhang, Y.; Kirs, A.; Ambroz, F.; Parkin, I. P.; Macdonald, T. J.; Lin, C.; R Bati, A. S.; Shapter, J. G.; Batmunkh, M. Ambient Fabrication of Organic–Inorganic Hybrid Perovskite Solar Cells. Small Methods 2021, 5 (1), 2000744. https://doi.org/10.1002/SMTD.202000744.

(103) Jena, A. K.; Ikegami, M.; Miyasaka, T. Severe Morphological Deformation of Spiro-OMeTAD in (CH3NH3)PbI3 Solar Cells at High Temperature. ACS Energy Lett 2017, 2 (8), 1760–1761. https://doi.org/10.1021/ACSENERGYLETT.7B00582/ASSET/IMAGES/LARGE/NZ-2017-00582Q_0002.JPEG.

(104) Jena, A. K.; Numata, Y.; Ikegami, M.; Miyasaka, T. Role of Spiro-OMeTAD in Performance Deterioration of Perovskite Solar Cells at High Temperature and Reuse of the Perovskite Films to Avoid Pb-Waste. J Mater Chem A Mater 2018, 6 (5), 2219–2230. https://doi.org/10.1039/C7TA07674F.

(105) Malinauskas, T.; Tomkute-Luksiene, D.; Sens, R.; Daskeviciene, M.; Send, R.; Wonneberger, H.; Jankauskas, V.; Bruder, I.; Getautis, V. Enhancing Thermal Stability and Lifetime of Solid-State Dye-Sensitized Solar Cells via Molecular Engineering of the Hole-Transporting Material Spiro-OMeTAD. ACS Appl Mater Interfaces 2015, 7 (21), 11107–11116. https://doi.org/10.1021/AM5090385/SUPPL_FILE/AM5090385_SI_001.PDF.

(106) Kasparavicius, E.; Magomedov, A.; Malinauskas, T.; Getautis, V. Long-Term Stability of the Oxidized Hole-Transporting Materials Used in Perovskite Solar Cells. Chemistry – A European Journal 2018, 24 (39), 9910–9918. https://doi.org/10.1002/CHEM.201801441.

(107) Zhao, X.; Kim, H. S.; Seo, J. Y.; Park, N. G. Effect of Selective Contacts on the Thermal Stability of Perovskite Solar Cells. ACS Appl Mater Interfaces 2017, 9 (8), 7148–7153. https://doi.org/10.1021/ACSAMI.6B15673/ASSET/IMAGES/LARGE/AM-2016-156737_0006.JPEG.

(108) Zhang, W.; Liu, P.; Sadollahkhani, A.; Li, Y.; Zhang, B.; Zhang, F.; Safdari, M.; Hao, Y.; Hua, Y.; Kloo, L. Investigation of Triphenylamine (TPA)-Based Metal Complexes and Their Application in Perovskite Solar Cells. ACS Omega 2017, 2 (12), 9231–9240. https://doi.org/10.1021/ACSOMEGA.7B01434/ASSET/IMAGES/LARGE/AO-2017-01434U_0004.JPEG.

(109) Li, M.; Wang, Z. K.; Yang, Y. G.; Hu, Y.; Feng, S. L.; Wang, J. M.; Gao, X. Y.; Liao, L. S. Copper Salts Doped Spiro-OMeTAD for High-Performance

Perovskite Solar Cells. Adv Energy Mater 2016, 6 (21), 1601156. https://doi.org/10.1002/AENM.201601156.

(110) Chen, C.; Zhang, W.; Cong, J.; Cheng, M.; Zhang, B.; Chen, H.; Liu, P.; Li, R.; Safdari, M.; Kloo, L.; Sun, L. Cu(II) Complexes as p-Type Dopants in Efficient Perovskite Solar Cells. ACS Energy Lett 2017, 2 (2), 497–503. https://doi.org/10.1021/ACSENERGYLETT.6B00691/ASSET/IMAGES/LARGE/NZ-2016-006914_0008.JPEG.

(111) Wang, Q.; Dong, Q.; Li, T.; Gruverman, A.; Huang, J.; Wang, Q.; Dong, Q.; Huang, J.; Li, T.; Gruverman, A. Thin Insulating Tunneling Contacts for Efficient and Water-Resistant Perovskite Solar Cells. Advanced Materials 2016, 28 (31), 6734–6739. https://doi.org/10.1002/ADMA.201600969.

(112) Zheng, X.; Chen, B.; Dai, J.; Fang, Y.; Bai, Y.; Lin, Y.; Wei, H.; Zeng, X. C.; Huang, J. Defect Passivation in Hybrid Perovskite Solar Cells Using Quaternary Ammonium Halide Anions and Cations. Nature Energy 2017 2:7 2017, 2 (7), 1–9. https://doi.org/10.1038/nenergy.2017.102.

(113) Buin, A.; Pietsch, P.; Xu, J.; Voznyy, O.; Ip, A. H.; Comin, R.; Sargent, E. H. Materials Processing Routes to Trap-Free Halide Perovskites. Nano Lett 2014, 14 (11), 6281–6286. https://doi.org/10.1021/NL502612M/SUPPL_FILE/NL502612M_SI_001.PDF.

(114) Manser, J. S.; Saidaminov, M. I.; Christians, J. A.; Bakr, O. M.; Kamat, P. v. Making and Breaking of Lead Halide Perovskites. Acc Chem Res 2016, 49 (2), 330–338. https://doi.org/10.1021/ACS.ACCOUNTS.5B00455/ASSET/IMAGES/LARGE/AR-2015-004557_0007.JPEG.

(115) Wetzelaer, G.-J. A. H.; Scheepers, M.; Sempere, A. M.; Momblona, C.; Ávila, J.; Bolink, H. J.; Wetzelaer, G.-J. A. H.; Scheepers, M.; Sempere, A. M.; Momblona, C.; Ávila, J.; Bolink, H. J. Trap-Assisted Non-Radiative

Recombination in Organic–Inorganic Perovskite Solar Cells. Advanced Materials 2015, 27 (11), 1837–1841. https://doi.org/10.1002/ADMA.201405372.

(116) Yoo, H. S.; Park, N. G. Post-Treatment of Perovskite Film with Phenylalkylammonium Iodide for Hysteresis-Less Perovskite Solar Cells. Solar Energy Materials and Solar Cells 2018, 179, 57–65. https://doi.org/10.1016/J.SOLMAT.2018.02.015.

(117) Li, Y.; Wu, H.; Qi, W.; Zhou, X.; Li, J.; Cheng, J.; Zhao, Y.; Li, Y.; Zhang, X. Passivation of Defects in Perovskite Solar Cell: From a Chemistry Point of View. Nano Energy 2020, 77, 105237. https://doi.org/10.1016/J.NANOEN.2020.105237.

(118) K H, G. Advances in Surface Passivation of Perovskites Using Organic Halide Salts for Efficient and Stable Solar Cells. Surfaces and Interfaces 2021, 26, 101420. https://doi.org/10.1016/J.SURFIN.2021.101420.

(119) Jiang, Q.; Zhao, Y.; Zhang, X.; Yang, X.; Chen, Y.; Chu, Z.; Ye, Q.; Li, X.; Yin, Z.; You, J. Surface Passivation of Perovskite Film for Efficient Solar Cells. Nature Photonics 2019 13:7 2019, 13 (7), 460–466. https://doi.org/10.1038/s41566-019-0398-2.

(120) K H, G. Advances in Surface Passivation of Perovskites Using Organic Halide Salts for Efficient and Stable Solar Cells. Surfaces and Interfaces 2021, 26, 101420. https://doi.org/10.1016/J.SURFIN.2021.101420.

(121) Zhuang, J.; Mao, P.; Luan, Y.; Yi, X.; Tu, Z.; Zhang, Y.; Yi, Y.; Wei, Y.; Chen, N.; Lin, T.; Wang, F.; Li, C.; Wang, J. Interfacial Passivation for Perovskite Solar Cells: The Effects of the Functional Group in Phenethylammonium Iodide. ACS Energy Lett 2019, 4 (12), 2913–2921. https://doi.org/10.1021/ACSENERGYLETT.9B02375/ASSET/IMAGES/LARGE/NZ9B02375_0005.JPEG.

(122) Yang, S.; Dai, J.; Yu, Z.; Shao, Y.; Zhou, Y.; Xiao, X.; Zeng, X. C.; Huang, J. Tailoring Passivation Molecular Structures for Extremely Small Open-Circuit Voltage Loss in Perovskite Solar Cells. J Am Chem Soc 2019, 141 (14), 5781–5787. https://doi.org/10.1021/JACS.8B13091/ASSET/IMAGES/LARGE/JA-2018-13091V_0005.JPEG.

CURRICULUM VITAE

Surname, Name: Bağ Çelik, Esra

EDUCATION

Degree	Institution	Year of Graduation
MS	METU Chemistry	2014
BS	METU Chemistry	2010
High School	Mehmet Emin Resulzade High School, Ankara	2005

EXPERIENCE

Kordsa	Project Leader	2022-continue
Cankaya University	Lecturer	2012-2020

PUBLICATIONS

Gunes, U., Bag Celik, E., Akgul, C. C., Koc, M., Ameri, M., Uzuner, B. E., ... & Gunbas, G. (2021). A Thienothiophene-Based Cation Treatment Allows Semitransparent Perovskite Solar Cells with Improved Efficiency and Stability. Advanced Functional Materials, 31, 2103130.

Bag, E., Begik, O., Yusan, P., Erel-Goktepe, I. (2015). Hydrogen-Bonded Multilayers with Controllable pH-Induced Disintegration Kinetics for Controlled Release Applications from Surfaces, Journal of Macromolecular Science, Part A, 52:4, 286.

FOREIGN LANGUAGES

English (Advanced), French (Beginner)

INTERESTS

Painting, Camping&Hiking, Puzzles, Musicals, Yoga, Pilates, Amateur Photography